

# Proposal for the NuPRISM Experiment in the J-PARC Neutrino Beamline

S. Bhadra,<sup>28</sup> A. Blondel,<sup>4</sup> S. Bordoni,<sup>7</sup> A. Bravar,<sup>4</sup> C. Bronner,<sup>10</sup> R.G. Calland,<sup>10</sup> J. Caravaca Rodríguez,<sup>7</sup> M. Dziewiecki,<sup>27</sup> M. Ericson,<sup>12,3</sup> T. Feusels,<sup>1</sup> G.A. Fiorentini Aguirre,<sup>28</sup> M. Friend,<sup>6,\*</sup> L. Haegel,<sup>4</sup> M. Hartz,<sup>10,26</sup> R. Henderson,<sup>26</sup> T. Ishida,<sup>6,\*</sup> M. Ishitsuka,<sup>23</sup> C.K. Jung,<sup>14,†</sup> A.C. Kaboth,<sup>8</sup> H. Kakuno,<sup>24</sup> H. Kamano,<sup>16</sup> A. Konaka,<sup>26</sup> Y. Kudenko,<sup>9,‡</sup> R. Kurjata,<sup>27</sup> M. Kuze,<sup>23</sup> T. Lindner,<sup>26</sup> K. Mahn,<sup>13</sup> J.F. Martin,<sup>25</sup> M. Martini,<sup>5</sup> J. Marzec,<sup>27</sup> K.S. McFarland,<sup>18</sup> S. Nakayama,<sup>21,†</sup> T. Nakaya,<sup>11,10</sup> S. Nakamura,<sup>15</sup> Y. Nishimura,<sup>22</sup> A. Rychter,<sup>27</sup> F. Sánchez,<sup>7</sup> T. Sato,<sup>15</sup> M. Scott,<sup>26</sup> T. Sekiguchi,<sup>6,\*</sup> T. Shima,<sup>16</sup> M. Shiozawa,<sup>21,10</sup> T. Sumiyoshi,<sup>24</sup> R. Tacik,<sup>17,26</sup> H.K. Tanaka,<sup>21,†</sup> H.A. Tanaka,<sup>1,§</sup> S. Tobayama,<sup>1</sup> M. Vagins,<sup>10,2</sup> C. Vilela,<sup>14</sup> J. Vo,<sup>7</sup> D. Wark,<sup>19,8</sup> M.O. Wascko,<sup>8</sup> M.J. Wilking,<sup>14</sup> S. Yen,<sup>26</sup> M. Yokoyama,<sup>20,†</sup> and M. Ziembicki<sup>27</sup>

(The NuPRISM Collaboration)

<sup>1</sup> University of British Columbia, Department of Physics and Astronomy, Vancouver, British Columbia, Canada

<sup>2</sup> University of California, Irvine, Department of Physics and Astronomy, Irvine, California, U.S.A.

<sup>3</sup> Physics Department, Theory Unit, CERN, Geneva, Switzerland

<sup>4</sup> University of Geneva, Section de Physique, DPNC, Geneva, Switzerland

<sup>5</sup> Department of Physics and Astronomy, Ghent University, Gent, Belgium

<sup>6</sup> High Energy Accelerator Research Organization (KEK), Tsukuba, Ibaraki, Japan

<sup>7</sup> Institut de Física d'Altes Energies (IFAE), Bellaterra (Barcelona), Spain

<sup>8</sup> Imperial College London, Department of Physics, London, United Kingdom

<sup>9</sup> Institute for Nuclear Research of the Russian Academy of Sciences, Moscow, Russia

<sup>10</sup> Kavli Institute for the Physics and Mathematics of the Universe (WPI),

Todai Institutes for Advanced Study, University of Tokyo, Kashiwa, Chiba, Japan

<sup>11</sup> Kyoto University, Department of Physics, Kyoto, Japan

<sup>12</sup> Université de Lyon, Université Claude Bernard Lyon 1, IPN Lyon (IN2P3), Villeurbanne, France

<sup>13</sup> Michigan State University, Department of Physics and Astronomy, East Lansing, Michigan, U.S.A.

<sup>14</sup> State University of New York at Stony Brook, Department of Physics and Astronomy, Stony Brook, New York, U.S.A.

<sup>15</sup> Osaka University, Department of Physics, Osaka, Toyonaka, Japan

<sup>16</sup> Osaka University, Research Center for Nuclear Physics(RCNP), Ibaraki, Osaka, Japan

<sup>17</sup> University of Regina, Department of Physics, Regina, Saskatchewan, Canada

<sup>18</sup> University of Rochester, Department of Physics and Astronomy, Rochester, New York, U.S.A.

<sup>19</sup> STFC, Rutherford Appleton Laboratory, Harwell Oxford, and Daresbury Laboratory, Warrington, United Kingdom

<sup>20</sup> University of Tokyo, Department of Physics, Tokyo, Japan

<sup>21</sup> University of Tokyo, Institute for Cosmic Ray Research, Kamioka Observatory, Kamioka, Japan

<sup>22</sup> University of Tokyo, Institute for Cosmic Ray Research, Research Center for Cosmic Neutrinos, Kashiwa, Japan

<sup>23</sup> Tokyo Institute of Technology, Department of Physics, Tokyo, Japan

<sup>24</sup> Tokyo Metropolitan University, Department of Physics, Tokyo, Japan

<sup>25</sup> University of Toronto, Department of Physics, Toronto, Ontario, Canada

<sup>26</sup> TRIUMF, Vancouver, British Columbia, Canada

<sup>27</sup> Warsaw University of Technology, Institute of Radioelectronics, Warsaw, Poland

<sup>28</sup> York University, Department of Physics and Astronomy, Toronto, Ontario, Canada

(Dated: June 16, 2015)

As long-baseline neutrino experiments enter the precision era, the difficulties associated with understanding neutrino interaction cross sections on atomic nuclei are expected to limit experimental sensitivities to neutrino oscillation parameters. In particular, the ability to relate experimental observables to the incident neutrino energy in all previous experiments has relied solely on theoretical models of neutrino-nucleus interactions, which currently suffer from very large theoretical uncertainties.

By observing charged current  $\nu_\mu$  interactions over a continuous range of off-axis angles from  $1^\circ$  to  $4^\circ$ , the NuPRISM water Cherenkov detector can provide a direct measurement of the far detector lepton kinematics for any given set of oscillation parameters, which largely removes neutrino interaction modeling uncertainties from T2K oscillation measurements. This naturally provides a direct constraint on the relationship between lepton kinematics and neutrino energy. In addition, NuPRISM is a sensitive probe of sterile neutrino oscillations with multiple energy spectra, which provides unique constraints on possible background-related explanations of the MiniBooNE anomaly. Finally, high-precision measurements of neutrino cross sections on water are possible, including electron neutrino measurements and the first ever measurements of neutral current interactions

\* also at J-PARC, Tokai, Japan

† affiliated member at Kavli IPMU (WPI), the University of Tokyo, Japan

‡ also at Moscow Institute of Physics and Technology and National Research Nuclear University "MEPhI", Moscow, Russia

§ also at Institute of Particle Physics, Canada

as a function of neutrino energy. Using these precise measurements of neutrino cross sections, it may be possible to measure CP violation in sub-GeV atmospheric neutrinos at the *3sigma* level.

The NuPRISM detector also provides significant benefits to the proposed Hyper-Kamiokande project. A demonstration that neutrino interaction uncertainties can be controlled will be important to understanding the physics reach of Hyper-K. In addition, NuPRISM will provide an easily accessible prototype detector for many of the new hardware components currently under consideration for Hyper-K. The following document presents the configuration, physics impact, and preliminary cost estimates for a NuPRISM detector in the J-PARC neutrino beamline.

CONTENTS			
I. Introduction	4		
A. Uncertainties in Neutrino Energy Determination	5	B. Civil Construction	37
B. ND280 Capabilities and Limitations	6	C. Liner and Tank	37
C. Detector Overview	7	D. Detector Frame and Lifting Mechanism	38
II. Physics Capabilities	7	1. Detector Shape, Support and Positioning	38
A. Off-Axis Fluxes	8	2. Water Flow and Optical Isolations	38
B. Monochromatic Beams	9	3. Walls of Inner Detector (ID)	39
C. Simulation Inputs	10	4. Detector in the shaft	39
D. Event Pileup	11	5. Detector Surveying	41
1. Visible particle rates and pile-up	12	E. Scintillator panels	41
2. Entering neutron background	14	1. Scintillator counters with WLS/avalanche photodiode readout	42
3. Cross-check with INGRID	14	2. Veto counters for NuPRISM	42
E. Event Selection for Sensitivity Studies	15	3. Integrated Design	42
F. T2K $\nu_\mu$ Disappearance Sensitivities	15	F. Photomultiplier Tubes	43
G. NuPRISM 1-Ring e-like Ring Measurements	23	G. Electronics	43
1. Beam $\nu_e$ and $\bar{\nu}_e$ cross section measurement	23	1. FADC Digitization	43
2. Predicting oscillated $\nu_e$ for the appearance measurement	24	2. Signal Conditioning And PMT HV Supply	44
3. Backgrounds from $\nu_\mu$ 's	25	3. Study of a Digital Constant Fraction Algorithm	44
H. Sterile Neutrino Sensitivity	25	4. Tests Using an Arbitrary Waveform Generator	46
1. Background	27	5. Noise Study and Optimum Filtering	48
2. Systematics	28	H. Water System	50
3. Sensitivities	28	1. Gd option	51
I. Atmospheric neutrino CP violation	28	IV. Detector Calibration	52
J. $\bar{\nu}_\mu$ Measurements	32	A. Overview of Super-K Calibration Systems	52
K. Cross Section Measurements	33	1. Detector hardware calibrations	52
1. CC Inclusive	34	2. Calibrations for physics analyses	53
2. CC $0\pi$	34	V. Conclusion	54
3. CC $1\pi^+$ and CC $1\pi^0$	35		
4. NC $1\pi^+$ and NC $1\pi^0$	35	References	54
III. Detector Design and Hardware	36		
A. Site Selection	36		

A. Detector Costs	56
1. Civil Construction	56
2. Photomultiplier Tubes	56
3. PMT Electronics	56
4. OD Scintillator Panels	57
5. Water System	57

## I. INTRODUCTION

With the publications of the first ever observation of  $\nu_e$  appearance, and the world's most precise measurement of  $\theta_{23}$ , T2K has achieved its initial experimental goals with only 8.5% of the approved protons on target (POT). The next phase of the experiment will make even more precise measurements of  $\nu_e$  appearance and  $\nu_\mu$  disappearance using both neutrinos and anti-neutrinos in order to probe the value of  $\delta_{CP}$ , the  $\theta_{23}$  octant, and  $|\Delta m_{32}^2|$ . In conjunction with measurements from NO $\nu$ A, these measurements may also provide a constraint on the neutrino mass hierarchy.

In order to achieve these goals, a more precise understanding of neutrino interaction cross sections is required. Currently, T2K is forced to rely on neutrino interaction generators to translate experimental observables into constraints on the neutrino energy spectrum, which depends on the value of the oscillation parameters. Measurements of very forward-going muons on the carbon target employed by the existing near detector, ND280, are translated into constraints on the  $4\pi$  muon angular distribution on a water target seen at the far detector. The interactions of final-state hadrons both within the nucleus and within each detector medium can have a significantly different impacts on the near and far detector analyses. Some of the backgrounds at far detector, Super-Kamiokande (Super-K), are poorly constrained at ND280. This is particularly true of NC $\pi^+$  events, which are problematic both because the cross section is not well measured, and because  $\pi^+$  reconstruction at Super-K is not well understood. This results in a contamination of both the  $\nu_\mu$  and  $\nu_e$  samples that produces large systematic uncertainties.

It is also necessary to measure events with single, electron-like rings in order to constrain any differences in the  $\nu_e$  and  $\nu_\mu$  cross sections. These events can be caused by a variety of sources, such as beam  $\nu_e$ , single  $\gamma$  production,  $\pi^0$  production, external  $\gamma$  background, sterile neutrino oscillations and radiative muon production. An excess of such events has been observed by MiniBooNE. It is important to confirm whether a similar excess exists on a water target, ideally with a water Cherenkov detector, and if found, the cause must be understood in order to perform precision  $\nu_e$  appearance measurements.

The least constrained component of these neutrino interaction models, however, is the relationship between the experimentally observable lepton kinematics and the energy of the incident neutrino. At present, there is an experimentally-unconstrained and potentially large bias in the ability to translate lepton kinematics to neutrino energy. Current estimates, based solely on new, recently developed models, suggest that this bias may be one of T2K's largest systematic uncertainties, and no existing dataset can provide a constraint on this uncertainty in a manner that does not rely on neutrino interaction models. Had neutrino interaction models been trusted to provide this relationship just 5 years ago, current mod-

els suggest that 20 to 30% of events where only the final state lepton was observed would have been reconstructed with an incorrect neutrino energy in a way that would not have been constrained or even detectable. Even a high-performance near detector, capable of precisely measuring all charged particles in the final state, would be forced to rely on models that relate lepton kinematics to hadronic final states, and no modern theoretical models offer a prediction for such a relationship within a nuclear environment.

A precise understanding of these interactions also provides an opportunity to search for CP violation in atmospheric neutrinos with energies below 1 GeV. This energy region has significant sensitivity to the effects of CP violation, but in order to extract this information, the  $\nu_e/\nu_\mu$  cross section ratio must be known to high precision, as well as the relationship between the lepton angle and the neutrino angle, which becomes large at low energies. NuPRISM can significantly enhance our understanding of both of these currently large systematic uncertainties.

The NuPRISM water-Cherenkov detector takes advantage of the energy dependence of the neutrino flux with off-axis angle by spanning a continuous range of 1 to 4 degrees in off-axis angle. This technique has the potential to significantly reduce uncertainties from neutrino interaction modeling in T2K oscillation analyses, as is demonstrated for the muon neutrino disappearance measurement described in Section II. In particular, these measurements will provide the first direct experimental constraint on the relationship between lepton kinematics and neutrino energy using measurements of final state muons at many different off-axis angles. In order to construct a more cost-effective detector that can reasonably be built on a timescale that is applicable to T2K, this document proposes to instrument a subset of the full water volume on a frame that moves vertically within the water tank, which sequentially samples the full off-axis range of the shaft in 5-6 separate running periods.

A large water-Cherenkov 1 km from a 600 MeV neutrino source is also an ideal experiment to search for sterile neutrino oscillations at  $\Delta m^2$  of 1 eV<sup>2</sup>. NuPRISM can provide additional constraints on explanations for the MiniBooNE low-energy excess, since the oscillation signature and the backgrounds vary differently as a function of off-axis angle. NuPRISM can provide a complementary measurement of comparable sensitivity to the Fermilab short-baseline LAr program.

The construction of a NuPRISM detector in the next 3-5 years can also provide significant benefits to Hyper-Kamiokande (Hyper-K). The problems with understanding neutrino interactions can have a larger impact on Hyper-K, since Hyper-K will have much smaller statistical errors, and a demonstration that these uncertainties can be managed with a NuPRISM near detector will significantly enhance the physics case for Hyper-K. In addition, NuPRISM is an easily accessible water Cherenkov detector that provides an ideal environment to test Hyper-K technology. Hyper-K proposes to use

new, in-water electronics, new solid state hybrid-PMTs (HPDs), and a new tank and liner construction to prevent leaks, all of which require extensive testing in a prototype detector. Finally, NuPRISM will provide an intermediate physics program that bridges the gap from T2K phase I to Hyper-K, which can provide continuity within the Japanese physics community while Hyper-K is being designed and constructed.

The remainder of this document provides an overview of the detector components and physics potential of NuPRISM. The results for a full T2K  $\nu_\mu$  disappearance analysis are provided, and a variety of additional NuPRISM neutrino energy spectrum fits are presented to demonstrate how the NuPRISM technique can constrain  $\nu_e$  cross sections, which will be important for measurements of  $\nu_e$  appearance and  $\delta_{CP}$ , as well as several different oscillation backgrounds. Cost estimates have been obtained for the items that are expected to dominate the cost of the project, in particular photomultiplier tubes (PMTs) and civil construction. For the additional less expensive items, cost estimates from a very similar project proposed in 2005, the T2K 2 km water Cherenkov detector, are used to guide expectations for the full NuPRISM project cost.

### A. Uncertainties in Neutrino Energy Determination

Prior to 2009, neutrino interaction models assumed that neutrinos, when encountering a nuclear target, interact a single nucleon. The initial state of the nucleon was characterized by a binding energy and Fermi momentum, which were drawn from either a Fermi gas [2, 3] or a more specialized spectral function treatment [4]. In this paradigm, all the remaining dynamics of charge-current quasi-elastic (CCQE) interactions, in which the target neutron is converted into an outgoing proton, are encapsulated in a set of three vector and three axial-vector form factors. Most of these form factors are tightly constrained from external electron and pion scattering experiments (for a detailed discussion, see Ref. [10]). The largest remaining uncertainty is on the axial vector form factor, which is assumed to take a dipole form,

$$F_A(Q^2) = \frac{F_A(0)}{(1 + \frac{Q^2}{M_A^2})^2}. \quad (1)$$

The parameter  $F_A(0)$  is precisely known from nuclear beta decay, which leaves  $M_A$  as the remaining uncertain parameter. Modifying  $M_A$  simultaneously alters both the overall CCQE cross section and the shape of the  $Q^2$  distribution.

In 2009, the first comparison of MiniBooNE CCQE-like data at neutrino energies around 1 GeV and NOMAD data at higher energies was released. A reproduction of that comparison is shown in Figure I A. The MiniBooNE data are consistent with an  $M_A$  value of 1.35 GeV

(an additional empirical parameter,  $\kappa$  is consistent with no modification at 1  $\sigma$ ), while the NOMAD data prefer an  $M_A$  of 1.03 GeV. This discrepancy is currently unexplained by neutrino-nucleus interaction models and is an outstanding experimental question that can be addressed by NuPRISM (see Section II K 2).

Later in 2009, the Marteau [5] formalism for the treatment of neutrino scattering on nucleon pairs in nuclei was resurrected by Martini *et al.* [6–8] to explain the higher event rate and muon kinematic distributions observed by MiniBooNE. If this explanation of the MiniBooNE event excess were correct, it would imply that neutrino energy reconstruction for all previous neutrino experiments on nuclei at the GeV scale could have significant biases for 20–30% of CCQE-like events. In the past few years, the models of Martini *et al.* and Nieves *et al.* [9] have begun to incorporate these effects, but such calculations are very difficult and the predictions of just these two models produce significantly different results when applied to T2K oscillation analyses [1].

There exists circumstantial experimental evidence for multinucleon interaction mechanisms in both neutrino and electron scattering, but nothing that allows us to conclusively solve the problem or even to down-select among the various calculations. In electron scattering, the reaction mechanism is different due to the absence of an axial-vector current component. In neutrino scattering experiments with broadband beams, the evidence is only circumstantial, since we must rely on the predictions of the models themselves to extract the neutrino energy for any given event. Other approaches, such as making precise measurements of the hadronic final state, are limited by a lack of theoretical understanding of the expected hadron kinematics for multinucleon events. Even the final state hadron spectra for CCQE events are modified by nuclear effects which are also not well understood.

Figure 2 illustrates the challenge associated with using near detector data to constrain the interaction model that predicts far detector event rates. The detectors measure the convolution of the neutrino spectrum with the interaction model. Since the near and far detector spectra are different due to neutrino oscillations, the measurement of this convolution in the near detector does not directly constrain the event rate in the far detector, and neutrino energies that represent a small fraction of the event rate in the near detector can be a significantly impact the measurement of oscillation parameters in the far detector.

In addition to multinucleon effects, other effects such as long range correlations and final state interactions within the target nucleus can also produce distortions to the neutrino energy spectrum that can be difficult to model. Figure 3 shows the ratio of the neutrino to anti-neutrino cross section for  $\nu_\mu$  according to several theoretical models. The MiniBooNE measurement is also shown. In order to perform precision oscillation measurements with uncertainties at the level of the few percent statistical errors expected for  $7.8 \times 10^{21}$  POT, it will be

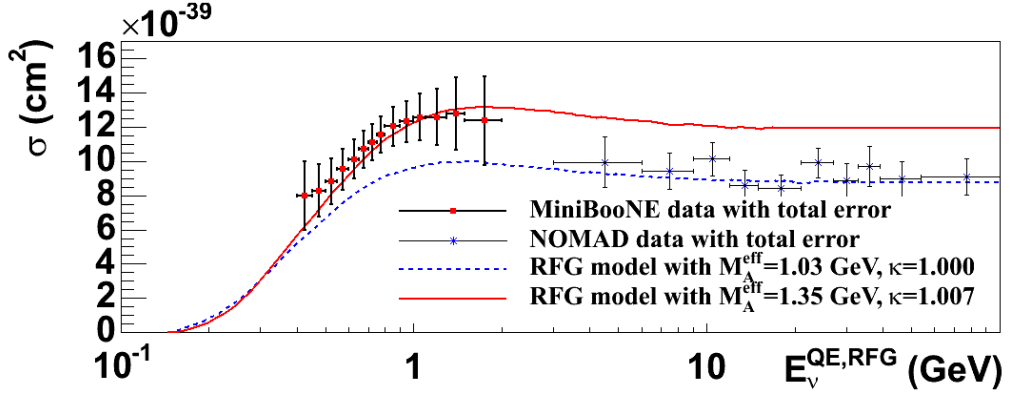


FIG. 1. The CCQE cross section measurements are shown for MiniBooNE and NOMAD. The data show significant differences between measurements made at low and high energies.

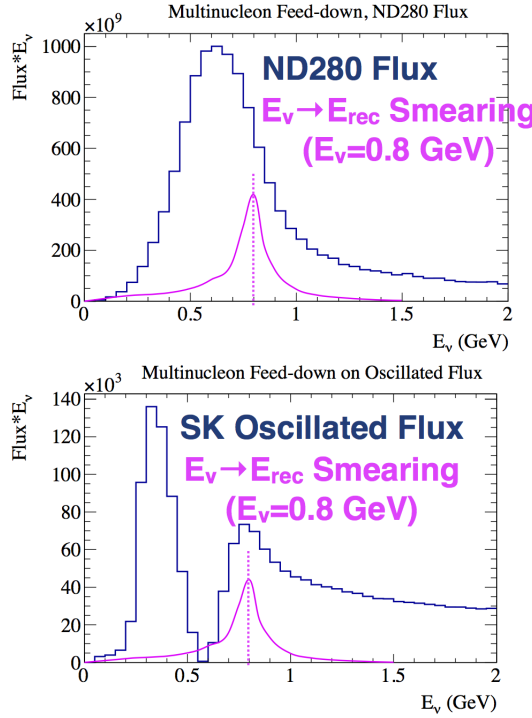


FIG. 2. A cartoon of the effect of energy reconstruction biases is shown for both the T2K near detector (top) and the far detector (bottom). At the far detector, these biases directly impact the measurement of the oscillation dip, but the biases are largely unconstrained at the near detector due to the large unoscillated sample of unbiased CCQE events.

necessary to provide a data-driven constraint on these neutrino interaction model uncertainties.

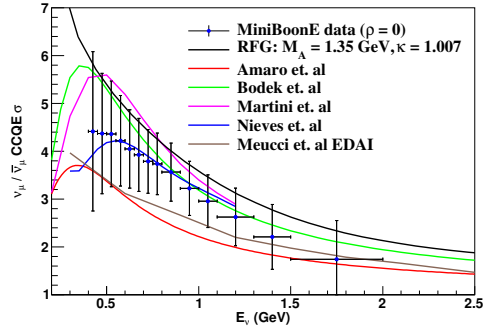


FIG. 3. The ratio of the CCQE cross section ratio for muon neutrinos and anti-muon neutrinos is shown for various theoretical models and the MiniBooNE measurement. More precision is required for precision CP violation measurements. (plot courtesy of J. Grange, private communication)

## B. ND280 Capabilities and Limitations

T2K oscillation analyses rely on precise constraints of flux and cross section model parameters from ND280. While a 3.2% uncertainty on the predicted number of electron neutrinos at the far detector has been achieved for the combination of flux and cross section parameters that are currently constrained by the near detector, there remains a 4.7% uncertainty on the far detector event sample due to additional cross section parameters that remain unconstrained. This unconstrained uncertainty is dominated by uncertainties in the modeling of the target oxygen nucleus, and largely depends on the theoretical model used to extrapolate measurements on carbon to oxygen.

The full capabilities of the T2K near detector have not yet been exploited. For example, the near detector analyses have thus far used interactions in the most-upstream Fine-Grained Detector (FGD1), which is composed en-

tirely of alternating layers of horizontally- and vertically-oriented scintillator bars. Since the FGD scintillator layers are predominantly composed of carbon and hydrogen, FGD1 measurements cannot directly probe interactions on oxygen. An additional FGD (FGD2) contains layers of water interspersed within its scintillator layers. A simultaneous fit of the interactions in both FGDs can provide a constraint on nuclear uncertainties in oxygen, and may potentially reduce the corresponding nuclear model uncertainties.

Another expected improvement to ND280 is the extension of the measured phase space of the outgoing lepton kinematics from a charged-current neutrino interaction. In the currently available analyses, muons are required to be produced in an FGD and traverse a minimum distance through the downstream TPC in order to make a measurement of both muon momentum and particle identification. This limits the muon acceptance to forward angles. Improvements to detector timing calibration and to track matching to the Electromagnetic Calorimeters (ECALs) and Side Muon Range Detectors (SMRDs) surrounding the FGDs and TPCs will allow for the reconstruction of charged-current events with backward-going and sideways-going muons. These additional samples will add less than 20% to the total even sample with a degraded energy resolution relative to events that enter a TPC, however they may be able to improve constraints on the cross section modeling in previously inaccessible and potentially important new regions of phase space.

An additional sample of events that has not yet been incorporated into the oscillation analysis are charged-current interactions in the pi-zero detector (P0D). The P0D is capable of operating with and without water targets dispersed throughout its active volume, and by measuring the event rates separately in these two configurations, it is possible to extract constraints on interactions in water. The requirement to match a track in the TPC limits the angular acceptance for muons produced in the P0D, however the larger fiducial volume of the P0D produces a higher event sample.

In order for any of these new samples to reduce systematic uncertainties, it is necessary to choose a neutrino interaction model that can characterize all possible variations of the neutrino cross sections as a function of both neutrino energy and the final state particle kinematics. In other words, model dependent choices will have to be made that will directly impact the strength of the constraint that can be extracted. Given the difficulties in understanding neutrino-nucleus interactions, it may not be possible to justify reductions in cross section systematic uncertainties beyond their current level without a direct experimental constraint. In addition, the aforementioned uncertainties due to multinucleon effects have not yet been incorporated into T2K oscillation analyses. Preliminary studies within T2K indicate that these effects would be difficult to constrain using only lepton kinematics from ND280 at the level required for the full-statistics T2K sensitivity, and may be as large

as the current dominant systematic uncertainties. The use of additional hadronic information is being explored, but any such constraint would be subject to even further model dependence.

### C. Detector Overview

The NuPRISM detector uses the same water Cherenkov detection technology as Super-K with a cylindrical water volume that is taller than Super-K (50-100 m vs 41 m) but with a much smaller diameter (10-12 m vs 39 m). The key requirements are that the detector span the necessary off-axis range ( $1^\circ$ - $4^\circ$ ) and that the diameter is large enough to contain the maximum required muon momentum. The baseline design considers a detector location that is 1 km downstream of the neutrino interaction target with a maximum contained muon momentum of 1 GeV/c. This corresponds to a 50 m tall tank with a 6 m diameter inner detector (ID) and a 10 m diameter outer detector (OD). A larger, 8 m ID is also being considered at the expense of some OD volume at the downstream end of the tank. As the NuPRISM analysis studies mature, the exact detector dimensions will be refined to ensure sufficient muon momentum,  $\nu_e$  statistics and purity, etc.

The instrumented portion of the tank is a subset of the full height of the water volume, currently assumed to be 10 m for the ID and 14 m for the OD. The novel feature of this detector is the ability to raise and lower the instrumented section of the tank in order to span the full off-axis range in 6 steps. The inner detector will be instrumented with either 5-inch or 8-inch PMTs to ensure sufficient measurement granularity for the shorter light propagation distances relative to Super-K. Also under consideration is to replace the OD reflectors with large scintillator panels, such as those used in the T2K Side Muon Range Detector (SMRD), although this has not yet been integrated into the overall detector design. More details regarding the detector hardware can be found in Section III

## II. PHYSICS CAPABILITIES

The physics goals of NuPRISM can be summarized in 4 main categories:

1. By recreating T2K oscillated neutrino energy spectra at the NuPRISM near detector, the outgoing lepton kinematics for any set of oscillation parameters can be measured at NuPRISM and directly compared to the observed lepton kinematics at the far detector. This results in the cancellation of systematic uncertainties related to neutrino interaction modeling to first order.
2. The distance between the neutrino production target and NuPRISM is ideal for searching for ster-

ile neutrino oscillations with mass splittings near  $1 \text{ eV}^2$ . Since the relative populations of the signal and background events vary differently as the off-axis angle changes, NuPRISM can provide unique constraints on many of the background-related hypotheses for the MiniBooNE low energy excess.

3. NuPRISM can directly measure the neutrino interaction final state from a range of mono-energetic beams. This allows for unique cross section measurements, such as the first ever energy-dependent neutral current (NC) and charged current (CC) cross section measurements that do not rely on neutrino generators to provide the incident neutrino energy. Measurements from mono-energetic beams, such as the energy transferred to the hadronic system, are also of great interest to the nuclear physics community. Another limiting set of systematic uncertainties for current and future neutrino oscillation experiments are the interaction cross sections for electron neutrinos, and NuPRISM will provide the world's most stringent constraints on electron neutrino interactions in water.
4. Atmospheric neutrinos measured at Super-Kamiokande with energies below 1 GeV have significant sensitivity to CP violation. However, extracting this information is currently limited by both the  $\nu_e/\nu_\mu$  cross section ratio and differential cross sections in lepton kinematics, both of which can be further constrained by NuPRISM, which may allow for up to a  $3\sigma$  measurement of CP violation, depending on the true value of  $\delta_{CP}$ .

The following sections will describe the NuPRISM detector concept and the impact it can have on a variety of physics analyses at T2K and Super-Kamiokande. A detailed description of the simulation and analysis inputs used to calculate sensitivities, which are largely derived from standard T2K tools, is also provided.

### A. Off-Axis Fluxes

The NuPRISM detector concept exploits the fact that as a neutrino detector is moved to larger off-axis angles relative to the beam direction, the peak energy of the neutrino energy spectrum is lowered and the size of the high-energy tail is reduced. This effect can be seen in Figure 4, which shows the neutrino energy spectra at several different off-axis angles in the T2K beam line. Since the off-axis angle for a single neutrino interaction can be determined from the reconstructed vertex position, this extra dimension of incident neutrino energy dependence can be used to constrain the interaction rates and final state particles in a largely model independent way.

A typical NuPRISM detector for the T2K beam line would span a continuous range of off-axis angles from  $1^\circ$

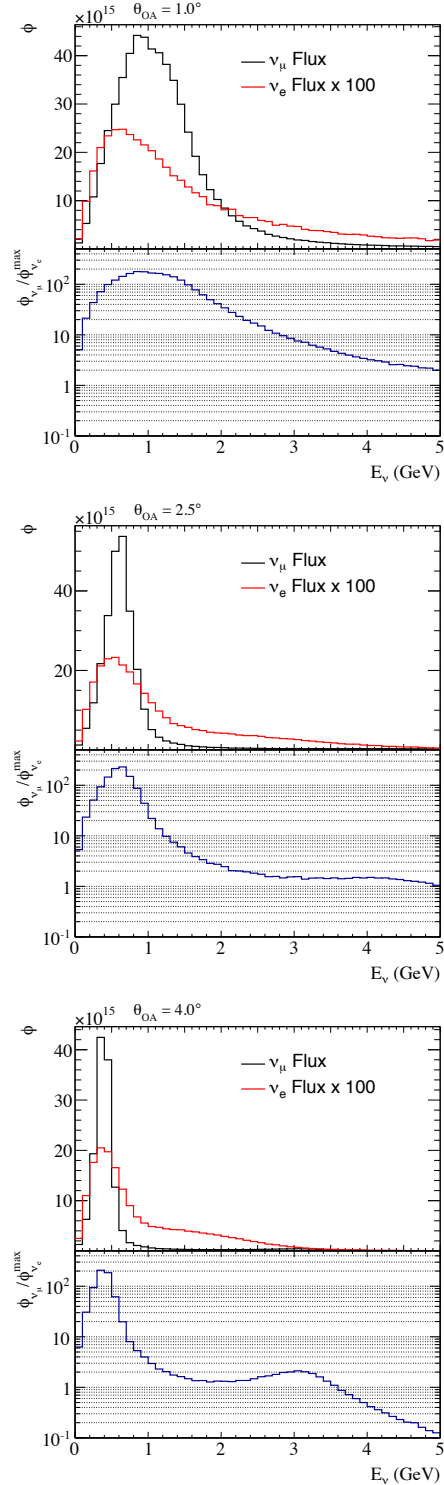


FIG. 4. The neutrino energy spectra for  $\nu_\mu$  and  $\nu_e$  fluxes in the T2K beam operating in neutrino mode are shown for off-axis angles of  $1^\circ$ ,  $2.5^\circ$ , and  $4^\circ$ . The  $\nu_\mu$  flux normalized by the maximum  $\nu_e$  flux is shown at the bottom of each plot, demonstrating that feed-down from high energy NC backgrounds to  $\nu_e$  candidates can be reduced by going further off-axis.

to  $4^\circ$ . For T2K, the best choice of technology is a water Cherenkov detector in order to use the same nuclear target as Super-K, and to best reproduce the Super-K detector efficiencies.

### B. Monochromatic Beams

The detector can be logically divided into slices of off-axis angle based on the reconstructed vertex of each event. In each slice, the muon momentum and angle relative to the mean neutrino direction can be measured. By taking linear combinations of the measurements in each slice, it is possible to produce an effective muon momentum and angle distribution for a Gaussian-like beam at energies between 0.4 and 1.2 GeV. Qualitatively, any desired peak energy can be chosen by selecting the appropriate off-axis angle, as shown in Figure 5, and then the further on-axis measurements are used to subtract the high energy tail, while the further off-axis measurements are used to subtract the low energy tail. Figure 5 shows three such “pseudo-monochromatic” neutrino energy spectra constructed in this manner. These spectra are for selected 1-ring muon candidates and systematic errors from the flux model are applied using the T2K flux systematic error model. The statistical errors for an exposure of  $4.5 \times 10^{20}$  protons on target are also shown. In all cases the high energy and low energy tails are mostly canceled over the full energy range and the monochromatic nature of the spectrum is stable under the flux systematic and statistical variations.

Figure 6 shows the reconstructed energy distributions for 1-ring muon candidates observed with the pseudo-monochromatic beams shown in Figure 5. The candidate events are divided into quasi-elastic scatters and non-quasi-elastic scatters, which include contributions from processes related to nuclear effects such as multinucleon interactions or pion absorption in final state interactions. With these pseudo-monochromatic beams, one sees a strong separation between the quasi-elastic scatters and the non-quasi-elastic scatters with significant energy reconstruction bias, especially in the 0.8 to 1.2 GeV neutrino energy range. These measurements can be used to directly predict the effect of non-quasi-elastic scatters in oscillation measurements and can also provide a unique constraint on nuclear models of these processes.

Since the pseudo-monochromatic beams have a well defined energy with a  $1\sigma$  width typically less than 0.15 GeV and a well defined direction, it is possible to use the known neutrino energy and direction to construct observables that are typically used in electron scattering experiments where the beam’s four momentum is known. These include the energy transfer to the target,  $\omega$ , the square of the three momentum transfer to the target,  $q^2$ , the square of the four momentum transfer,  $Q^2 = q^2 - \omega^2$ , and the Bjorken  $x$ ,  $x_B = Q^2/(2m\omega)$ . Unlike the typical treatment in neutrino scattering data, where the energy and momentum transfer are calculated assuming

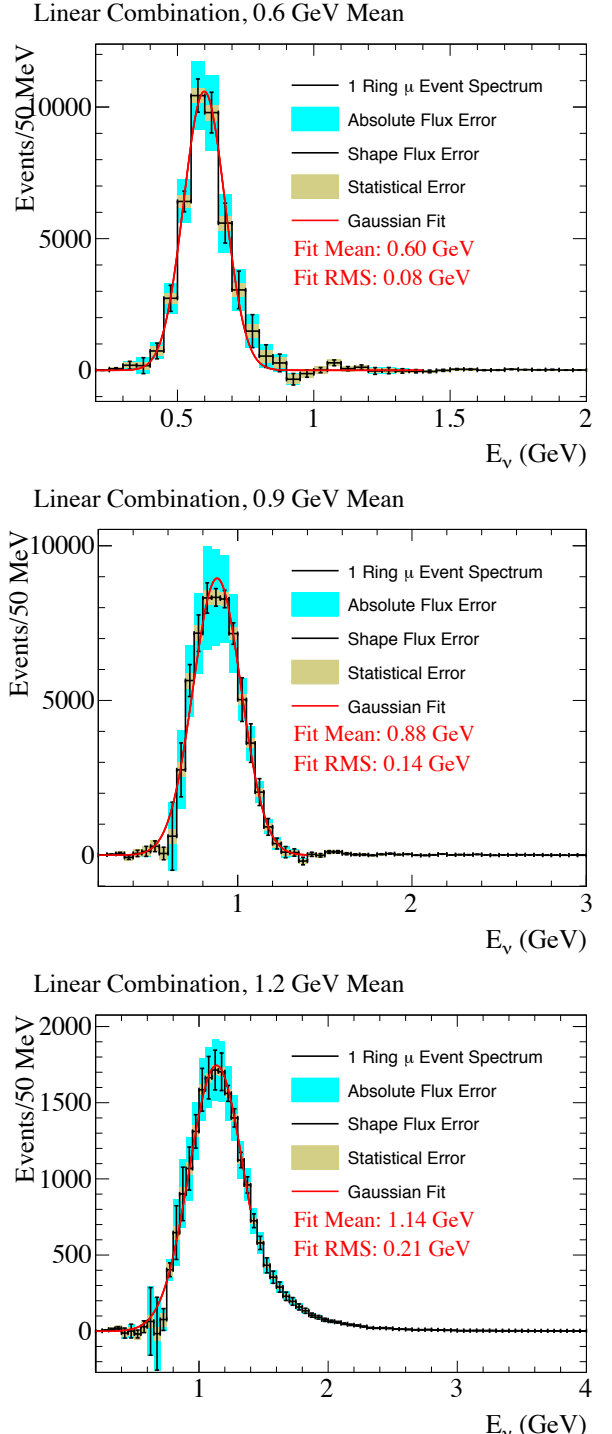


FIG. 5. Three “pseudo-monochromatic” spectra centered at 0.6 (top), 0.9 (middle) and 1.2 (bottom) GeV. The aqua error bars show the  $1\sigma$  uncertainty for flux systematic variations, while the black error bars show the flux systematic variation after the overall normalization uncertainty is removed. The tan error bars show the statistical uncertainty for samples corresponding to  $4.5 \times 10^{20}$  protons on target.

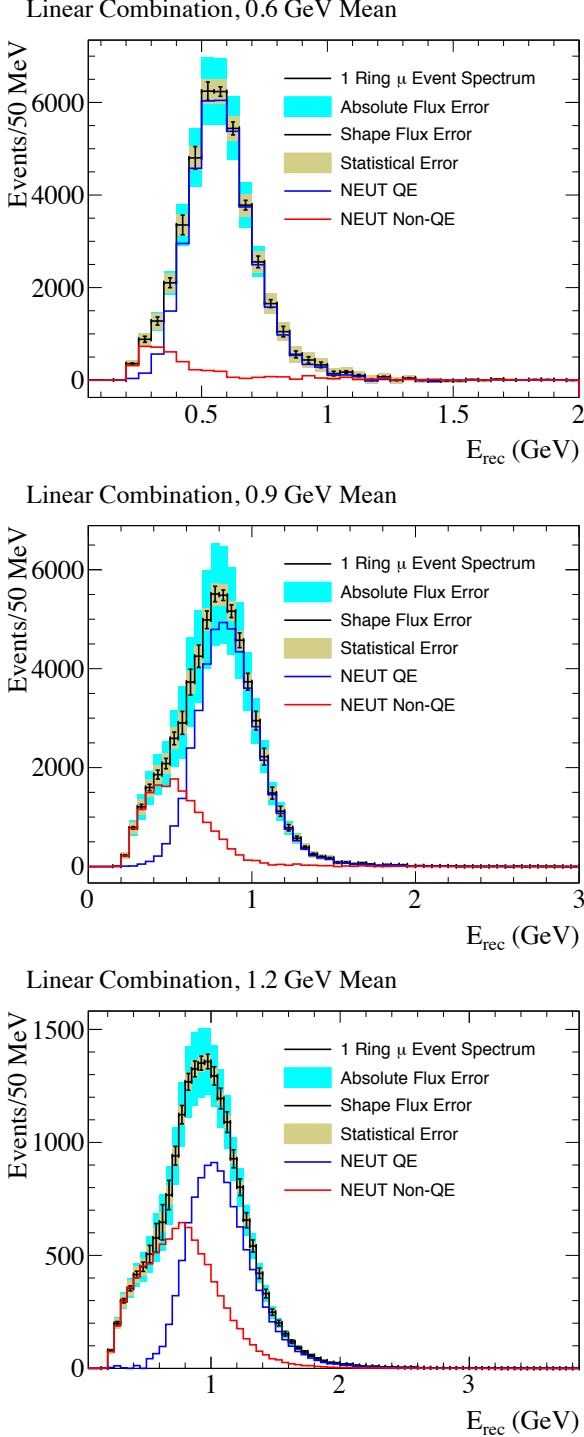


FIG. 6. The reconstructed energy distributions for 1-ring muon candidate events produced using “pseudo-monochromatic” spectra centered at 0.6 (top), 0.9 (middle) and 1.2 (bottom) GeV. The aqua error bars show the  $1\sigma$  uncertainty for flux systematic variations, while the black error bars show the flux systematic variation after the overall normalization uncertainty is removed. The tan error bars show the statistical uncertainty for samples corresponding to  $4.5 \times 10^{20}$  protons on target. The red and blue histograms show the contributions from non-quasi-elastic and quasi-elastic scatters respectively.

quasielastic kinematics with a single bound nucleon target, the energy and momentum transfer can be calculated from the pseudo-monochromatic beam constraint and the observed final state muon kinematics. Hence the cross section as a function of these observables can be measured for non-quasielastic as well as quasielastic interactions. Figure 7 shows the distribution of reconstructed single  $\mu$  ring events with an  $E_\nu = 1$  GeV pseudo-monochromatic beam in the energy and momentum transfer variables, broken down by true quasielastic and non-quasielastic events. Figure 8 shows the energy transfer for a single slice of  $q^2 = 0.7 - 0.9$   $\text{GeV}/c^2$  with flux and statistical error bars included. By making measurements in these variables, NuPRISM measures neutrino-nucleus cross sections as a function of the kinematics of probe of the nucleus, independent of the interaction type. This is a unique capability among neutrino scattering experiments.

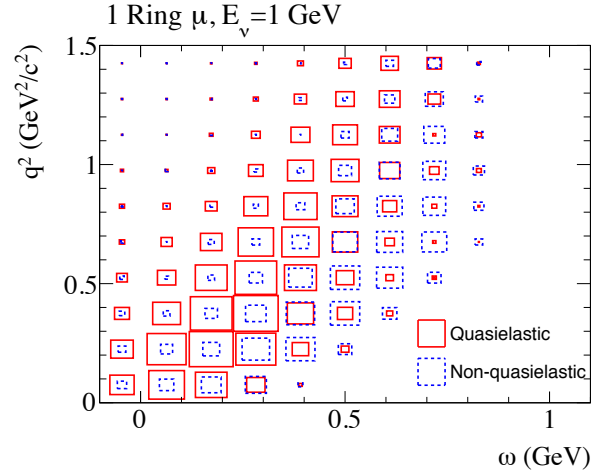


FIG. 7. For an  $E_\nu = 1$  GeV pseudo-monochromatic beam, the distribution of observed single muon ring events in reconstructed energy transfer and reconstructed square of the three momentum transfer. The true quasielastic events are shown in red and the true non-quasielastic events are shown in blue.

The NuPRISM technique can be expanded beyond these pseudo-monochromatic beams. This linear combination method can be used to reproduce a wide variety of flux shapes between 0.4 and 1.0 GeV. In particular, as described later in this section, it is possible to reproduce all possible oscillated Super-K spectra with a linear combination of NuPRISM measurements, which significantly reduces many of the uncertainties associated with neutrino/nucleus interaction modeling.

### C. Simulation Inputs

To perform NuPRISM sensitivity analyses, the official T2K flux production and associated flux uncertainties have been extended to cover a continuous range of off-axis angles, and the standard T2K package used to gen-

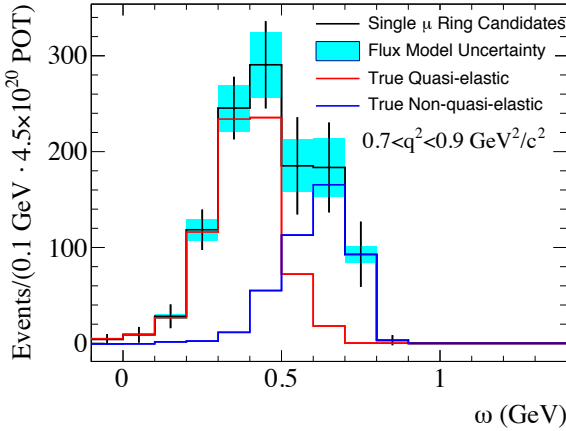


FIG. 8. For an  $E_\nu = 1$  GeV pseudo-monochromatic beam, the distribution of observed single muon ring events in reconstructed energy transfer when the reconstructed  $q^2$  is between 0.7 and  $0.9\text{ GeV}^2/\text{c}^2$ . The true quasielastic events are shown in red and the true non-quasielastic events are shown in blue. The flux and statistical uncertainties (for a  $4.5 \times 10^{20}$  proton on target exposure) are shown.

erate vertices in ND280 has also been modified to handle flux vectors with varying energy spectra across the detector. However, for the analysis presented in this note, full detector simulation and reconstruction of events were not available. Instead, selection efficiencies and reconstruction resolutions for vertex, direction, and visible energy were tabulated using the results of fTQu run on Super-K events. The efficiency for electrons (muons) was defined as events passing the following cuts: OD veto, 1-ring, e-like ( $\mu$ -like), 0 (1) decay electrons, and the T2K fTQu  $\pi^0$  rejection (no  $\pi^0$  cut). The efficiency tabulation was performed in bins of the true neutrino energy, the visible energy and distance along the track direction to the wall of the most energetic ring, and separate tables were produced for charged current events with various pion final states (CC0 $\pi$ , CC1 $\pi^\pm 0\pi^0$ , CC0 $\pi^\pm 1\pi^0$ , CCN $\pi^\pm 0\pi^0$ , and CCother) for both  $\nu_e$  and  $\nu_\mu$  events, as well as a set of neutral current final states, also characterized by pion content (NC0 $\pi$ , NC1 $\pi^\pm 0\pi^0$ , NC0 $\pi^\pm 1\pi^0$ , NCN $\pi^\pm 0\pi^0$ , and NCother). To determine the smearing of true quantities due to event reconstruction, vertex, direction, and visible energy resolution functions were also produced for the 1-ring e-like and  $\mu$ -like samples in bins of visible energy and distance along the track direction to the wall of the most energetic ring.

The neutrinos in NuPRISM are simulated with the T2K flux simulation tool called JNUBEAM. The version of JNUBEAM used is consistent with what is currently used by T2K and it includes the modeling of hadronic interactions based on data from the NA61/SHINE experiment. We define the off-axis angle for a particular neutrino as the angle between the beam axis and the vector from the average neutrino production point along

the beam axis to the point at which the neutrino crosses the flux plane, as illustrated in Fig. 9. The off-axis angle is defined in terms of the average neutrino production point so that an off-axis angle observable can be constructed based on the location of the interaction vertex in NuPRISM. The off-axis angle and energy dependence for each neutrino flavor is shown in Fig. 10. The neutrino flux files are produced for both neutrino mode (focussing positively charged hadrons) and antineutrino mode (focussing negatively charged hadrons), although only the neutrino mode flux is used for the analysis presented in this note.

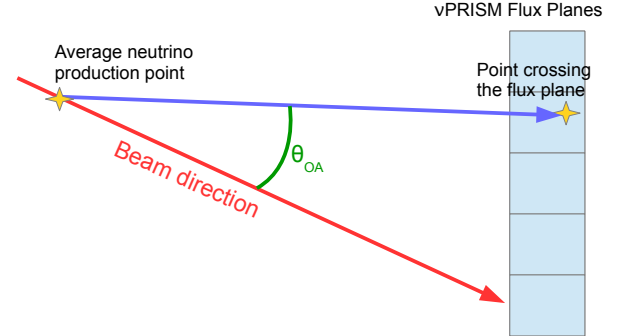


FIG. 9. The definition of the off-axis angle for individual neutrinos.

The positions of the neutrino interaction vertices in the NuPRISM water volume are shown in Fig. 11. The rate of simulated interactions has been cross checked against the observed INGRID rates and found to be consistent.

#### D. Event Pileup

The baseline design of NuPRISM is an outer detector (OD) volume with radius of 5 m and height of 14 m, and an inner detector (ID) volume with a radius of 3 m and height of 10 m, located 1 km from the T2K target. We also consider a design where the ID volume has a radius of 4 m and height of 12 m, leaving 1 m of OD surrounding the ID.

We have carried out a simulation of events in the NuPRISM ID and OD volumes, as well as the surrounding earth and water column to study the event pile-up in NuPRISM. Interactions and particle propagation in the earth+NuPRISM geometry shown in Fig. 12 are simulated. The flux at the upstream end of the volume is simulated using the JNUBEAM package with horn currents set to 320 kA (neutrino beam) or -320 kA (antineutrino beam). Interactions in the earth and detector volumes are generated using the same tools NEUT neutrino interaction generator. The earth volume is filled with  $\text{SiO}_2$  with a density of  $2.15\text{ g/cm}^3$ . The water volume has three detector sub-volumes: the ID detector, the OD

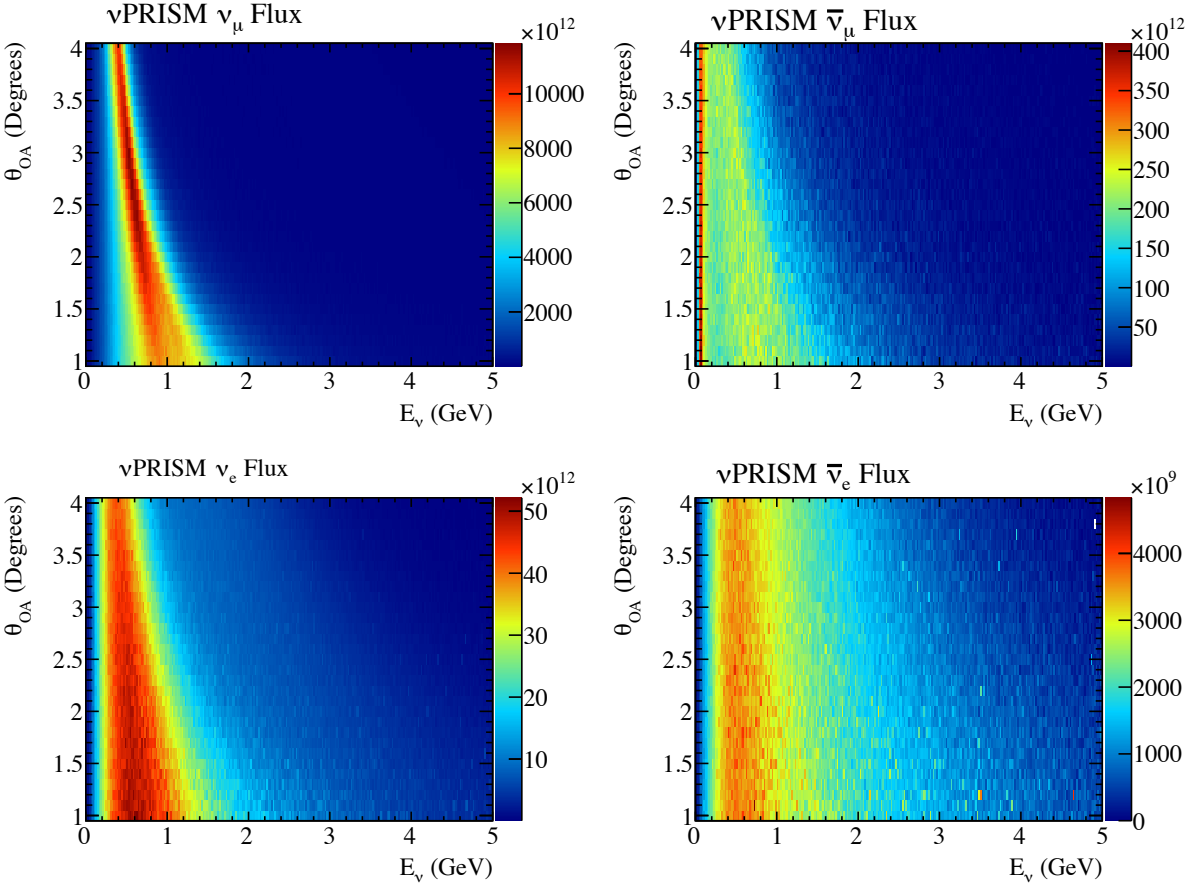


FIG. 10. The neutrino flux (arbitrary normalization) as a function of off-axis angle and energy for each neutrino flavor with the horn in neutrino-mode operation.

detector and an intermediate volume corresponding the the 4 m radius ID. The vertical position of the detector volumes in the water column can be adjusted to study the event pile-up at different off-axis angles. A GEANT4 simulation of the particles from the neutrino vectors is carried out and all particles with visible energy greater than 10 MeV are recorded if they originate in any of the detector volumes or cross any of the detector volume boundaries. Entering neutrons are considered separately from charged particles and photons.

Events can be categorized in two ways: by where the original interaction takes place and by the detector volumes in which particles produce Cherenkov radiation. In the first case, events are categorized as originating in the ID, OD or the earth and water surrounding the OD. In the second case, events are categorized as producing light exclusively in the OD, exclusively in the ID, or in both the ID and OD. Events that originate in the ID and are contained in the ID are the signal events.

The J-PARC beam consists of 8 microbunches per spill. The microbunches are  $\sim$ 15 ns long and separated by  $\sim$ 600 ns. For 750 kW beam operation with a 1 Hz spill frequency, there are  $2 \times 10^{13}$  protons in each mi-

crobatch. For the pile-up studies presented here, we consider  $2 \times 10^{13}$  protons per bunch and  $1.6 \times 10^{14}$  protons per spill. Event rates are considered with the NuPRISM detector placed at off-axis positions of 1.0-1.6°, 2.0-2.6° and 3.0-3.6°. Event rates are also produced at 0.0-0.6° off-axis so that comparisons can be made to the observed event rates in the T2K on-axis INGRID detectors.

### 1. Visible particle rates and pile-up

Tables I and II show the simulated event rates with visible particles for the 3 m and 4 m radius IDs respectively. For the 1.0 – 1.6° off-axis angle position, the total rate of ID+OD visible events in a spill (8 bunches) is 8.10. If a bunch contains an event, the probability that the next bunch contains at least one visible event is 63.7%. This suggests that NuPRISM should employ deadtimeless electronics that can record events in neighboring bunches and that the after-pulsing of PMTs should be carefully considered.

For the 3 m ID case in the 1.0 – 1.6° position, there are 0.917 events with OD light per bunch. If a simple veto on

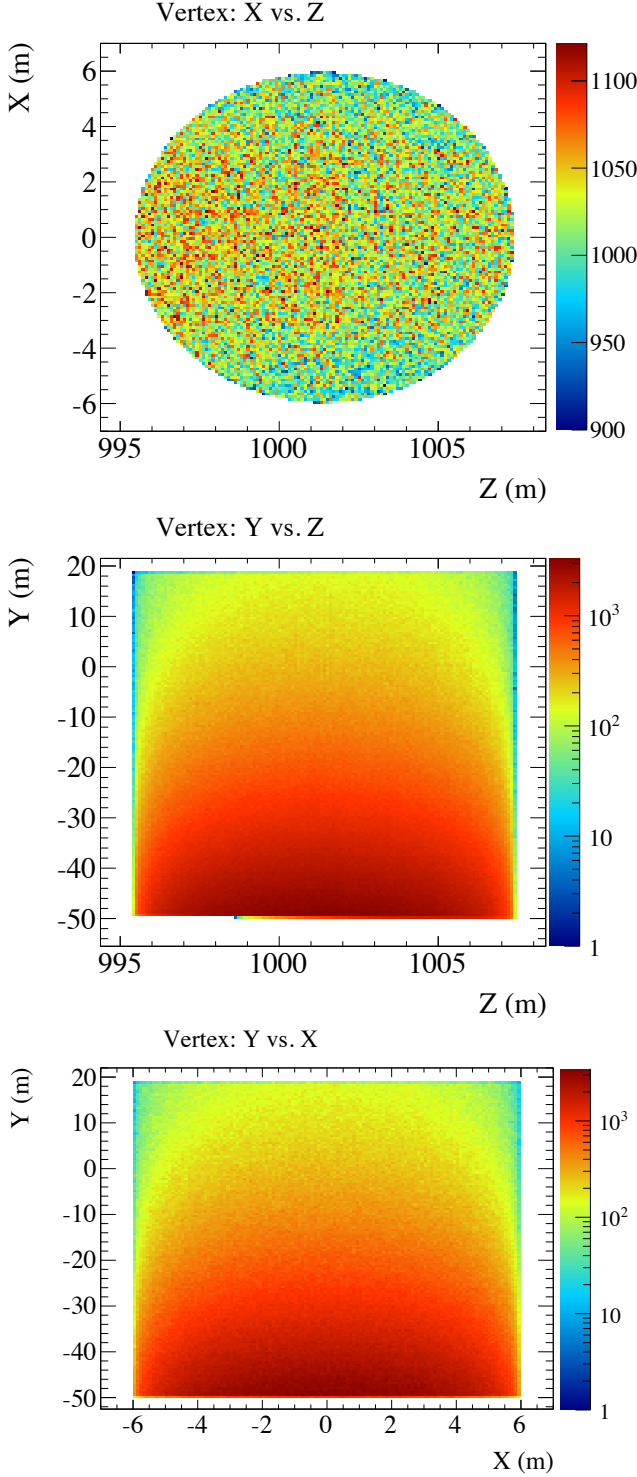


FIG. 11. The distribution of simulated vertices shown in projections to the x-z (top), y-z (middle) and x-y (bottom) planes. Here x is defined as the horizontal axis perpendicular to the beam, z is the horizontal axis in the beam direction and y is the vertical axis.

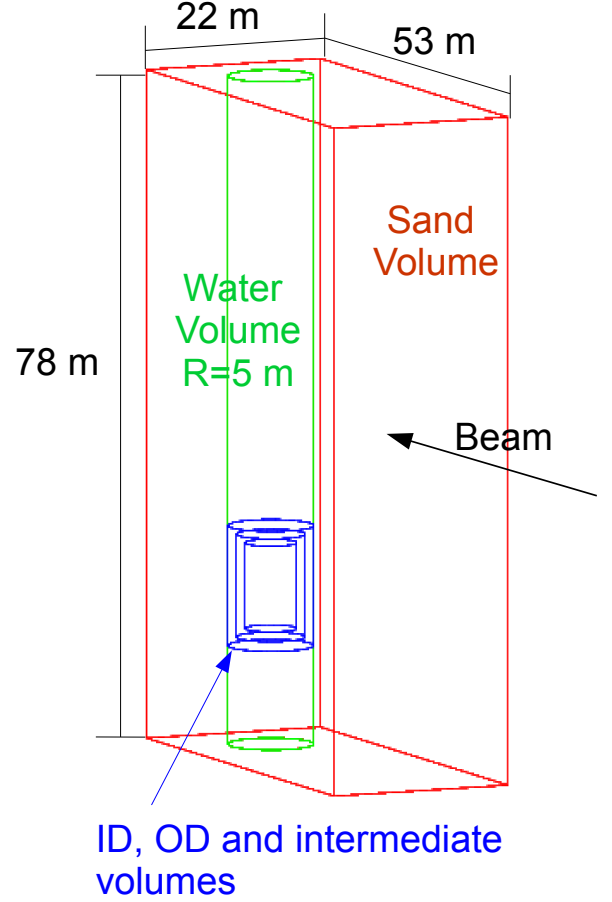


FIG. 12. The GEANT4 geometry used in the pile-up simulation.

any OD light in the same bunch is applied, 60.0% of fully contained ID events are vetoed due to the accidental coincidence rate in the OD. This simple OD veto rate drops to 25.8% and 10.7% for the  $2.0 - 2.6^\circ$  and  $3.0 - 3.6^\circ$  positions respectively. For the 4 m ID case, the simple OD veto rates are 54.2%, 22.2% and 9.5% for the  $1.0 - 1.6^\circ$ ,  $2.0 - 2.6^\circ$  and  $3.0 - 3.6^\circ$  positions respectively. A more intelligent OD veto may be applied if entering charged particles are tracked by scintillator panels at the OD and ID detector boundaries. These events may be kept in the analysis and the reconstruction can be seeded with the entering particle position and trajectory as measured by the scintillator panels. In that case, the OD veto rates can be as low as 30.7% and 28.6% for the  $1.0 - 1.6^\circ$  position with the 3 m and 4 m radius IDs respectively.

The importance of the OD veto depends on the type of reconstructed candidate event. For reconstructed muon candidates, it is expected that entering backgrounds can be controlled by fiducialization, and a tight OD veto may not be required. For reconstructed electron candidates,

entering backgrounds may need to be controlled with and OD veto. However, the most pure electron candidate samples will be collected in the most off-axis positions, where the OD pile-up is the smallest. Hence it is expected that pile-up in the OD will not drastically reduce the efficiency to select the event samples of most interest.

When the OD veto is applied, there may also be pile-up of fully contained ID events. There are on average 0.095, 0.035 and 0.016 fully contained ID events per bunch in the 3 m radius ID for the  $1.0 - 1.6^\circ$ ,  $2.0 - 2.6^\circ$  and  $3.0 - 3.6^\circ$  off-axis positions respectively. The percentage of fully contained ID events with 2 or more interactions is 4.6%, 1.7% and 0.8% for the 3 off-axis positions. For the 4 m radius ID, these percentages increase to 10.9%, 4.1% and 1.8%. It is expected that this level of pile-up can be handled by the reconstruction, either by vetoing on the presence of multiple vertices, or by reconstructing multiple vertices.

The probability for a selected FC ID event to be the only ID event in a spill is 22.4%. Since the muon decay time ( $2.2 \mu\text{s}$ ) is comparable to the bunch spacing (600 ns), electrons from muon decays cannot be matched to their primary interaction using only the decay electron production time. For interactions inside the ID, a spatial likelihood matching the decay electron to the primary vertex may be constructed based on the reconstructed decay electron vertex position and the reconstructed primary vertex or reconstructed stopping point of the candidate muons or charged pions in the event. For decay electrons originating from muons produced outside of the ID, a similar spatial likelihood may be constructed using OD light, ID light, and hits from scintillator panels (if they are installed between the OD and ID) from the entering particle. Since the muon mean lifetime is shorter than the spill length ( $5 \mu\text{s}$ ), there will also be statistical power to match decay electrons to their primary vertex based on the time separation of the decay electron vertex and primary vertex. On the other hand, the muon lifetime may provide a cross-check for the spatial matching of primary and decay electron vertices since significant mismatching would tend to smear the time separation distribution beyond the muon lifetime.

The event rates for an antineutrino beam are simulated by changing the horns' operating currents to -320 kA. Due to the smaller antineutrino cross section, the pile-up rates for antineutrinos are smaller than the comparable neutrino rates for every detector configuration.

## 2. Entering neutron background

Neutrons entering NuPRISM may interact to produce visible particles. Visible particles from neutron interactions have been included in the rates calculated in the previous section. If NuPRISM is doped with Gd to detect neutrons produced in neutrino interactions in the ID, entering beam induced neutrons will be a source of background. The number of neutrons entering the OD,

4 m radius ID and 3 m radius ID have been simulated.

Since the neutron capture time on Gd is  $\sim 30 \mu\text{s}$  and the spill length is  $\sim 5 \mu\text{s}$ , the entering neutron rates for a full spill ( $1.6 \times 10^{14}$  protons on target) are shown in Table III. In the  $1.0 - 1.6^\circ$  position, 9.120 neutrons enter the OD, but only 1.844 enter the 4 m radius ID. This reduction is greater than what is expected based on the relative surface areas of the OD and ID, and is due to the fact that there are no free protons in the  $\text{SiO}_2$  earth simulation to moderate low energy neutrons. However, the inclusion of 0.5% by mass of H in the earth does not significantly change the rate of neutrons entering the ID. Since the rate of neutrons entering the ID for the most on-axis position is  $\sim 1\text{-}2$  neutrons per spill, the reconstruction of neutron capture vertices with sufficient spatial resolution to separate signal neutrons from entering background neutrons is an important design consideration if NuPRISM will include Gd doping.

## 3. Cross-check with INGRID

We can cross-check the estimated NuPRISM event rates by extrapolating from the event rates observed by INGRID. We assume that the rate of interactions inside the detector will scale with the detector mass, and the rate of entering events from the earth will scale with the cross-sectional area of the detector. The rates should also scale with  $1/d^2$ , were  $d$  is the distance from the average neutrino production point to the detector, about 240 m for INGRID and 960 m for NuPRISM.

INGRID observes  $1.74 \text{ events per } 1 \times 10^{14} \text{ protons on target}$  in 14 INGRID modules with a total mass of  $5.7 \times 10^4 \text{ kg}$ . For an OD+ID mass of  $1.1 \times 10^6 \text{ kg}$ , we extrapolate the INGRID rate, assuming 60% detection efficiency in INGRID, to obtain 0.69 interactions in the OD+ID for  $2.0 \times 10^{13}$  protons on target. The simulated rates of visible OD+ID interactions in NuPRISM are 2.33 and 0.67 for the  $0.0 - 0.6^\circ$  and  $1.0 - 1.6^\circ$  positions respectively. Since INGRID covers an angular range of about  $\pm 1$  degree, it is reasonable that the extrapolated value from INGRID falls between the simulated NuPRISM values at these two positions.

INGRID also observes a event rate from earth interactions of  $4.53 \text{ events per } 1 \times 10^{14} \text{ POT}$  in 14 modules with a cross-sectional area of  $21.5 \text{ m}^2$ . These earth interaction candidates are INGRID events failing the upstream veto and fiducial volume cuts. The selection of entering earth-interaction events is  $> 99\%$  efficient and 85.6% pure. Scaling to the OD cross-sectional area and distance while correcting for the efficiency and purity gives a rate of 0.32 events entering the OD per bunch. The rates from the NuPRISM simulation are 1.10 and 0.34 for the  $0.0 - 0.6^\circ$  and  $1.0 - 1.6^\circ$  degree positions respectively. Once again, the extrapolated INGRID rate is close to the range observed in the NuPRISM simulation.

In summary, the event pile-up rates for NuPRISM appear manageable. Even for the most on-axis position

TABLE I. The event rates per  $2 \times 10^{13}$  protons on target for NuPRISM with horn currents at 320 kA and ID radius of 3 m.

	Interaction Outside OD			Interaction Inside OD			Interaction Inside ID		
	Producing light in:								
Off-axis Angle ( $^{\circ}$ )	OD only	ID only	ID & OD	OD only	ID only	ID & OD	OD only	ID only	ID & OD
0.0-0.6	0.877	0.001	0.226	1.464	0.005	0.241	0.007	0.341	0.271
1.0-1.6	0.273	0.000	0.068	0.428	0.001	0.071	0.002	0.094	0.075
2.0-2.6	0.084	0.000	0.021	0.149	0.000	0.021	0.000	0.035	0.024
3.0-3.6	0.034	0.000	0.007	0.062	0.000	0.001	0.000	0.016	0.009

TABLE II. The event rates per  $2 \times 10^{13}$  protons on target for NuPRISM with horn currents at 320 kA and ID radius of 4 m.

	Interaction Outside OD			Interaction Inside OD			Interaction Inside ID		
	Producing light in:								
Off-axis Angle ( $^{\circ}$ )	OD only	ID only	ID & OD	OD only	ID only	ID & OD	OD only	ID only	ID & OD
0.0-0.6	0.612	0.004	0.488	0.763	0.007	0.265	0.008	0.807	0.479
1.0-1.6	0.193	0.001	0.147	0.227	0.002	0.079	0.002	0.227	0.134
2.0-2.6	0.061	0.000	0.044	0.077	0.001	0.026	0.001	0.084	0.042
3.0-3.6	0.025	0.000	0.016	0.033	0.000	0.011	0.000	0.036	0.015

and high power beam, most bunches with interactions will only have a single interaction with visible light in the ID. The OD veto rate from pile-up can be as large as 60%, hence detailed studies of the OD design and performance will be carried out. The OD veto rate may be reduced and better understood with the inclusion of scintillator panels at the outer edge of the OD or at the OD/ID boundary. The electronics for NuPRISM should be deadtime-less to handle multiple events per spill. The rate of entering neutrons per spill is  $\sim 1\text{-}2$  for the most on-axis position, so the reconstruction of neutron capture on Gd vertices will be considered in the optimization of the ID photo-detector configuration.

### E. Event Selection for Sensitivity Studies

We select samples of single ring muon and electron candidates for the long and short baseline sensitivity studies described in the following sections. As described in Section II C, the efficiencies for single ring electron or muon selections are applied using tables calculated from the SK MC. The efficiency tables are calculated with the following requirements for muon and electron candidates:

- Muon candidate requirements: fully contained, a single muon-like ring, 1 or fewer decay electrons
- Electron candidate requirements: fully contained, a single electron-like ring, no decay electrons, passes the fitQun  $\pi^0$  cut

Additional cuts are applied on the smeared  $\nu$ PRISM MC. For the muon candidates the cuts are similar to the SK selection for the T2K disappearance analysis:

- Muon candidate cuts:  $dWall > 100$  cm,  $toWall > 200$  cm,  $E_{vis} > 30$  MeV,  $p_{\mu} > 200$  MeV/c

where  $dWall$  is the distance from the event vertex to the nearest wall, and  $toWall$  is the distance from the vertex to the wall along the direction of the particle.

For the single ring electron candidates, the cuts on  $toWall$  and  $E_{vis}$  were reoptimized since the separation between electrons and muons or electrons and  $\pi^0$ 's degrades closer to the wall. The cut on  $dWall$  is set to 200 cm to avoid entering backgrounds. The cuts are:

- Electron candidate cuts:  $dWall > 200$  cm,  $toWall > 320$  cm,  $E_{vis} > 200$  MeV

The tight fiducial cuts for the electrons candidates are needed to produce a relatively pure sample, but there is a significant impact to the electron candidate statistics. A simulation with finer PMT granularity may allow for the  $toWall$  cut to be relaxed, increasing the statistics without degrading the purity.

### F. T2K $\nu_{\mu}$ Disappearance Sensitivities

The most straightforward application of the NuPRISM concept to T2K is in the  $\nu_{\mu}$  disappearance measurement. The main goal of this  $\nu_{\mu}$  disappearance analysis is to demonstrate that NuPRISM measurements will remove most of the neutrino cross section systematic uncertainties from measurements of the oscillation parameters. This is achieved by directly measuring the muon momentum vs angle distribution that will be seen at Super-K for any choice of  $\theta_{23}$  and  $\Delta m_{32}^2$ .

To clearly compare the NuPRISM  $\nu_{\mu}$  analysis with the standard T2K approach, the full T2K analysis is reproduced using NuPRISM in place of ND280. This is done by generating fake data samples produced from throws of the flux and cross section systematic parameters and fitting these samples using the standard oscillation analysis framework. In each flux, cross section and

TABLE III. The entering neutron rates per  $1.6 \times 10^{14}$  protons on target for NuPRISM with horn currents at 320 kA.

Off-axis Angle ( $^{\circ}$ )	Entering OD	Entering ID ( $r=4$ m)	Entering ID ( $r=3$ m)
1.0-1.6	9.120	1.844	1.073
2.0-2.6	2.954	0.598	0.354
3.0-3.6	1.189	0.232	0.132

statistical throw, three fake data samples using different cross section models were produced at both ND280 and Super-K: default NEUT with pionless delta decay, NEUT with the Nieves multinucleon model replacing pionless delta decays, and NEUT with an ad-hoc multinucleon model that uses the final state kinematics of the Nieves model and the cross section from Martini *et al.* For each throw, all three fake data samples were fit to derive estimates of the oscillation parameters. The differences between the fitted values of  $\sin^2 \theta_{23}$  for the NEUT nominal and NEUT+Nieves or NEUT+Martini fake data fits are shown in Figure 13. The systematic uncertainty associated with assuming the default NEUT model rather than the model of Martini or Nieves is given by the quadrature sum of the RMS and mean (i.e. bias) of these distributions. For the ND280 analysis, there is a 3.6% uncertainty when comparing with the Nieves model, and a 4.3% uncertainty in the measured value of  $\sin^2 \theta_{23}$  when comparing with the Martini model. These uncertainties would be among the largest for the current T2K  $\nu_\mu$  disappearance analysis, and yet they are based solely on model comparisons with no data-driven constraint.

As was discussed in Section IA the limitation of using ND280 data to predict observed particle distributions at Super-K is that the neutrino flux at these two detectors is different due to oscillations. Therefore, any extrapolation has significant and difficult to characterize cross section model dependent uncertainties. In the NuPRISM based analysis, this limitation is resolved by deriving linear combinations of the fluxes at different off-axis angles to produce a flux that closely matches the predicted oscillated flux at Super-K. The observed particle distributions measured by NuPRISM are then combined with the same linear weights to predict the particle distribution at Super-K. In this way, the analysis relies on the flux model to determine the weights that reproduce the oscillated flux while minimizing cross section model dependence in the extrapolation.

The first stage of the NuPRISM  $\nu_\mu$  analysis is to separate the 1-4 degree off-axis range of the detector into 30 0.1 degree or 60 0.05 degree bins in off-axis angle. The neutrino energy spectrum in each off-axis bin is predicted by the T2K neutrino flux simulation. For each hypothesis of oscillation parameter values that will be tested in the final oscillation fit, the oscillated Super-K energy spectrum is also predicted by the T2K neutrino flux simulation. A linear combination of the 30 (60) off-axis fluxes is then taken to reproduce each of the Super-K oscillated

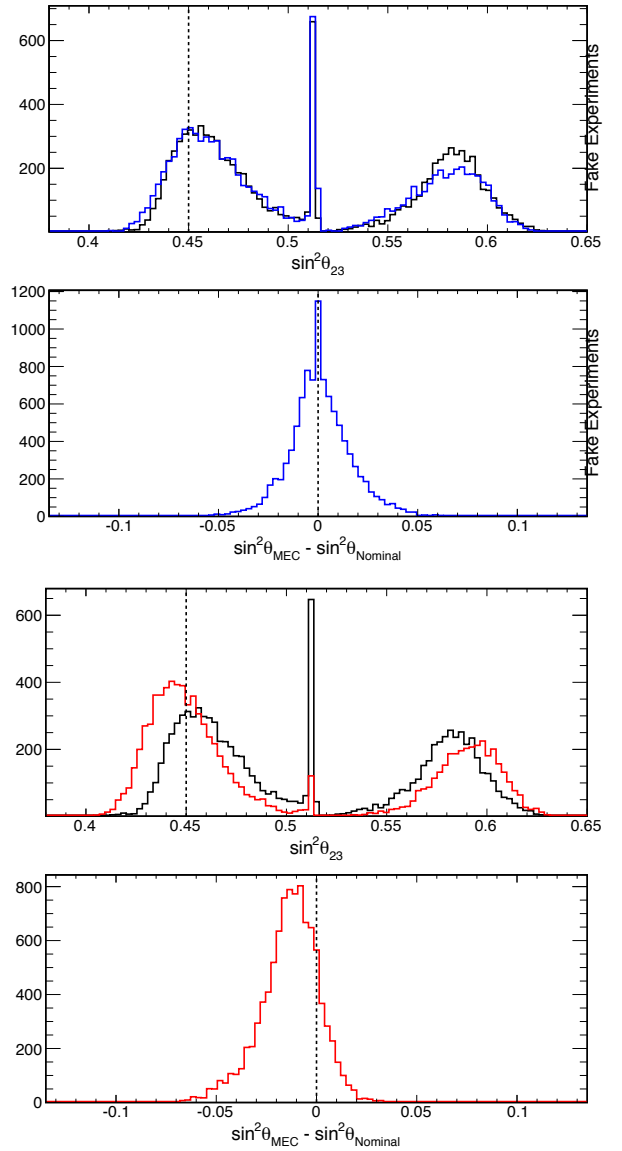


FIG. 13. The results of fitting fake data with and without multinucleon effects are shown. The measured differences in  $\sin^2 \theta_{23}$  when comparing the Nieves model to default neut (blue) and the Martini model to default neut (red) give RMS values of 3.6% and 3.2%, respectively, and biases of 0.3% and -2.9%, respectively.

spectra,

$$\Phi^{SK}(E_\nu; \theta_{23}, \Delta m_{32}^2) E_\nu = \sum_{i=1}^{30} c_i(\theta_{23}, \Delta m_{32}^2) E_\nu \Phi_i^{\nu P}(E_\nu), \quad (2)$$

where  $c_i(\theta_{23}, \Delta m_{32}^2)$  is the weight of each off-axis bin,  $i$ . The extra factors of  $E_\nu$  are inserted to approximate the effect of cross section weighting. The  $c_i(\theta_{23}, \Delta m_{32}^2)$  are determined by a fitting routine that seeks agreement between the Super-K flux and the linear combination over a specified range of energy. An example linear combination of nuPRISM off-axis fluxes that reproduces the SK flux is shown in Figure 14. These fits can successfully reproduce Super-K oscillated spectra, except at neutrino energies below  $\sim 400$  MeV. The maximum off-axis angle is  $4^\circ$ , which peaks at 380 MeV, so at lower energies it is difficult to reproduce an arbitrary flux shape. This could be improved by extending the detector further off-axis.

The determination of the  $c_i(\theta_{23}, \Delta m_{32}^2)$  weights to reproduce the oscillated flux is subject to some optimization. Figure 15 shows two sets of weights for a particular oscillation hypothesis. In the first case a smoothness constrain was applied to the weights so that they vary smoothly between neighboring off-axis angle bins. In the second case the weights are allowed to vary more freely relative to their neighbors. Figure 16 shows the comparisons of the NuPRISM flux linear combinations with the Super-K oscillated flux for a few oscillation hypotheses in the smoothed and free weight scenarios. The oscillated flux in the maximum oscillation region is nearly perfectly reproduced when the weights are allowed to vary more freely. When they are constrained to vary smoothly, the agreement is less perfect, although still significantly better than the agreement between ND280 and Super-K fluxes. An analysis using the free weights is less dependent on the cross section model assumptions in the extrapolation to Super-K since the Super-K flux is more closely matched. On the other hand, the analysis with the smoothed weights is less sensitive to uncertainties on the flux model and NuPRISM detector model that have an off-axis angle dependence since neighboring bins have similar weight values. The statistical errors are also smaller for the smoothed weight case since the sum in quadrature of the weights in a given neutrino energy bin is smaller when there are less fluctuations in weight values. In the analysis presented here, the smoothed weights are used, although the optimization of the level of smoothness is an area where the analysis will be improved in the future.

The NuPRISM candidate events are events with a single observed muon ring and no other observed particles, matching the selection applied at Super-K. After the  $c_i(\theta_{23}, \Delta m_{32}^2)$  coefficients are derived, they are used to make linear combination of observed candidate event distributions from each NuPRISM off-axis bin. In this case the observables are the momentum and polar angle of the scattered muon candidate, and hence the expected Super-K distribution of these observables is predicted by

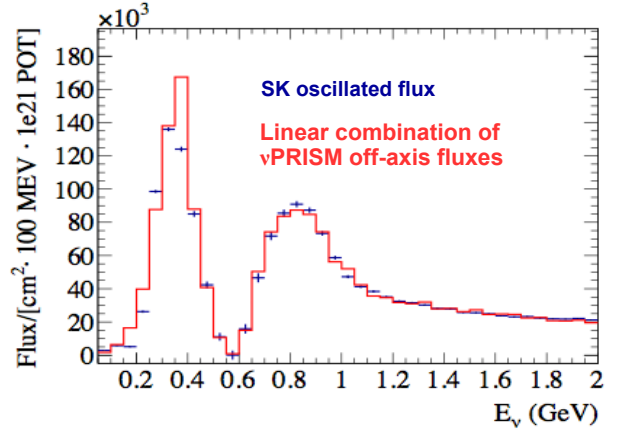


FIG. 14. A sample fit of the flux in 30 NuPRISM fluxes to an oscillated Super-K flux is shown. Good agreement can be achieved, except at low energies due to the  $4^\circ$  maximum off-axis angle seen by NuPRISM.

the linear combination of observed NuPRISM events.

In order to use these NuPRISM measurements to make an accurate prediction of Super-K muon kinematics, a series of corrections are required. First, non-signal events from either neutral current events or charged current events with another final state particle above Cherenkov threshold, must be subtracted from each near detector slice. This is particularly important for neutral current events, which depend on the total flux rather than the oscillated flux at Super-K, but depend on the oscillated flux in the NuPRISM linear combination. This background subtraction is model dependent, and is a source of systematic uncertainty, although neutral current interactions can be well constrained by in situ measurements at NuPRISM. The differences in detector efficiency and resolution must also be corrected. The efficiency differences are due to differences in detector geometry and are largely independent of cross section modeling. Detector resolutions must be well determined from calibration data, but this effect is somewhat mitigated due to the fact that the near and far detector share the same detector technology. Finally, for the present analysis, the two dimensional muon momentum vs angle distribution is collapsed into a one dimensional  $E_{rec}$  distribution using a transfer matrix,  $M_{i,p,\theta}(E_{rec})$ . This is an arbitrary choice that does not introduce model dependence into the final result, and has only been used for consistency with existing T2K  $\nu_\mu$  disappearance results. Future analyses can be conducted entirely in muon momentum and angle variables.

The final expression for the NuPRISM prediction for

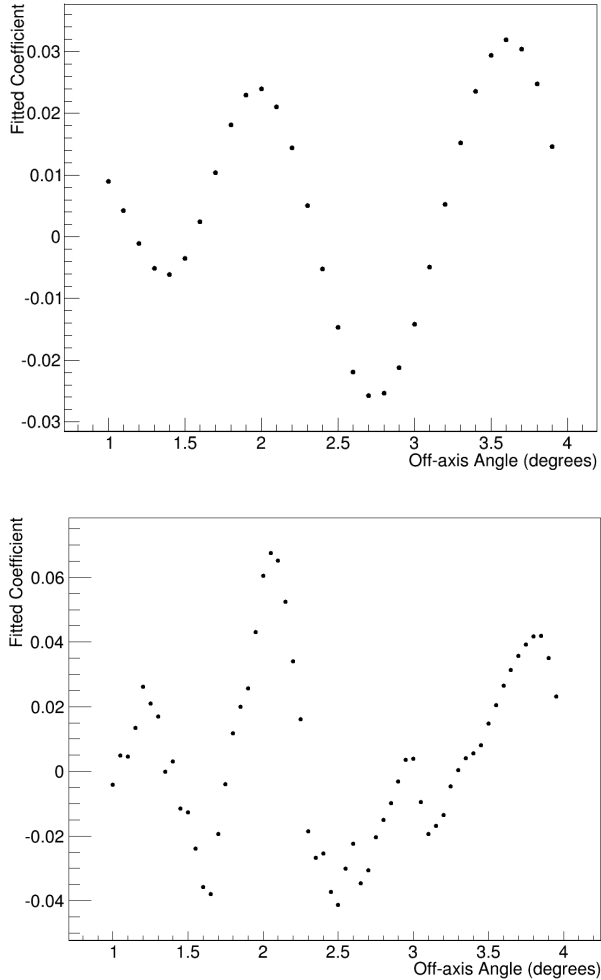


FIG. 15. The weights for each off-axis bin produced in the NuPRISM flux fits are shown after requiring that neighboring bins have similar values (top; as in Figure 16 left column) and with neighboring bins allowed to vary more freely relative to each other (bottom; as in Figure 16 right column).

the Super-K event rate is then

$$\begin{aligned}
 N^{SK}(E_{rec}; \theta_{23}, \Delta m_{32}^2) &= \delta(E_{rec}) + B^{SK}(E_{rec}; \theta_{23}, \Delta m_{32}^2) \\
 &+ \sum_{i=1}^{30} \sum_{p,\theta} c_i(\theta_{23}, \Delta m_{32}^2) (N_{i,p,\theta}^{\nu P} - B_{i,p,\theta}^{\nu P}) \\
 &\times \frac{\epsilon_{p,\theta}^{SK}}{\epsilon_{i,p,\theta}^{\nu P}} M_{i,p,\theta}(E_{rec}),
 \end{aligned} \tag{3}$$

where  $N^{SK}(E_{rec})$  and  $N_{i,p,\theta}^{\nu P}$  are the number of expected events in Super-K  $E_{rec}$  bins and NuPRISM off-axis angle, muon momentum, and muon angle bins, respectively,  $B^{SK}(E_{rec})$  and  $B_{i,p,\theta}^{\nu P}$  are the corresponding number of background events in these samples, and  $\epsilon_{p,\theta}^{SK}$  and  $\epsilon_{i,p,\theta}^{\nu P}$  are the efficiencies in each detector. The final correction factor,  $\delta(E_{rec})$ , accounts for any residual differences be-

tween the NuPRISM prediction and the Super-K event rate predicted by the Monte Carlo simulation. These are mostly due to the previously described imperfect flux fitting, and the fact that NuPRISM is not sensitive to neutrino energies above  $\sim 1.5$  GeV since most muons at that energy are not contained within the inner detector. Comparisons of the Super-K event rate and the NuPRISM prediction for Super-K prior to applying the  $\delta(E_{rec})$  correction factor are given in Figure 17.

The NuPRISM technique effectively shifts uncertainties in neutrino cross section modeling into flux prediction systematic uncertainties. This is quite helpful in oscillation experiments since many flux systematic uncertainties cancel, and the important physical processes in the flux prediction, the hadronic scattering, can be directly measured by dedicated experiments using well characterized proton and pion beams. Figure 18 shows the effect of a few selected flux uncertainties on the Super-K energy spectrum and the NuPRISM linear combination. The largest flux uncertainty is due to pion production in proton-carbon interactions, but this uncertainty mostly cancels when applied at both the near and far detector. The more problematic uncertainties are those that affect the off-axis angle, such as horn current and proton beam positioning, since these effects will impact Super-K and the NuPRISM linear combinations differently. Figure 19 shows four examples of how the Super-K  $E_{rec}$  distribution and the corresponding NuPRISM predicted distribution vary for different throws of all the flux and cross section systematic uncertainties. The predicted spectra from the nuPRISM linear combination closely tracks the true spectrum at SK, indicating a correlated effect from most systematic parameters on the nuPRISM linear combination and SK event rates.

The final covariance matrices are shown in Figure 20. The largest errors are at high energies where no NuPRISM events are present due to the smaller diameter of the detector relative to Super-K. In this region, the Super-K prediction is subject to the full flux and cross section uncertainties with no cancellation at the near detector. Similarly, at energies below 400 MeV the errors get larger since the current  $4^\circ$  upper bound in off-axis angle prohibits the NuPRISM flux fit from matching the Super-K spectrum at low energies.

Using the NuPRISM covariance matrices shown in Figure 20 in place of those produced by ND280, the standard T2K  $\nu_\mu$  disappearance oscillation analysis is repeated. The results are shown in Figure 21. As expected, the NuPRISM analysis is largely insensitive to cross section modeling. Replacing the default new model with the Nieves multinucleon model now produces a 1.0% uncertainty in  $\sin^2 \theta_{23}$ , and the corresponding Martini uncertainty is 1.2%. More importantly, this uncertainty is now constrained by data rather than a pure model comparison. These uncertainties are expected to be further reduced as the flux fits are improved, and NuPRISM constraints on NC backgrounds and information from ND280

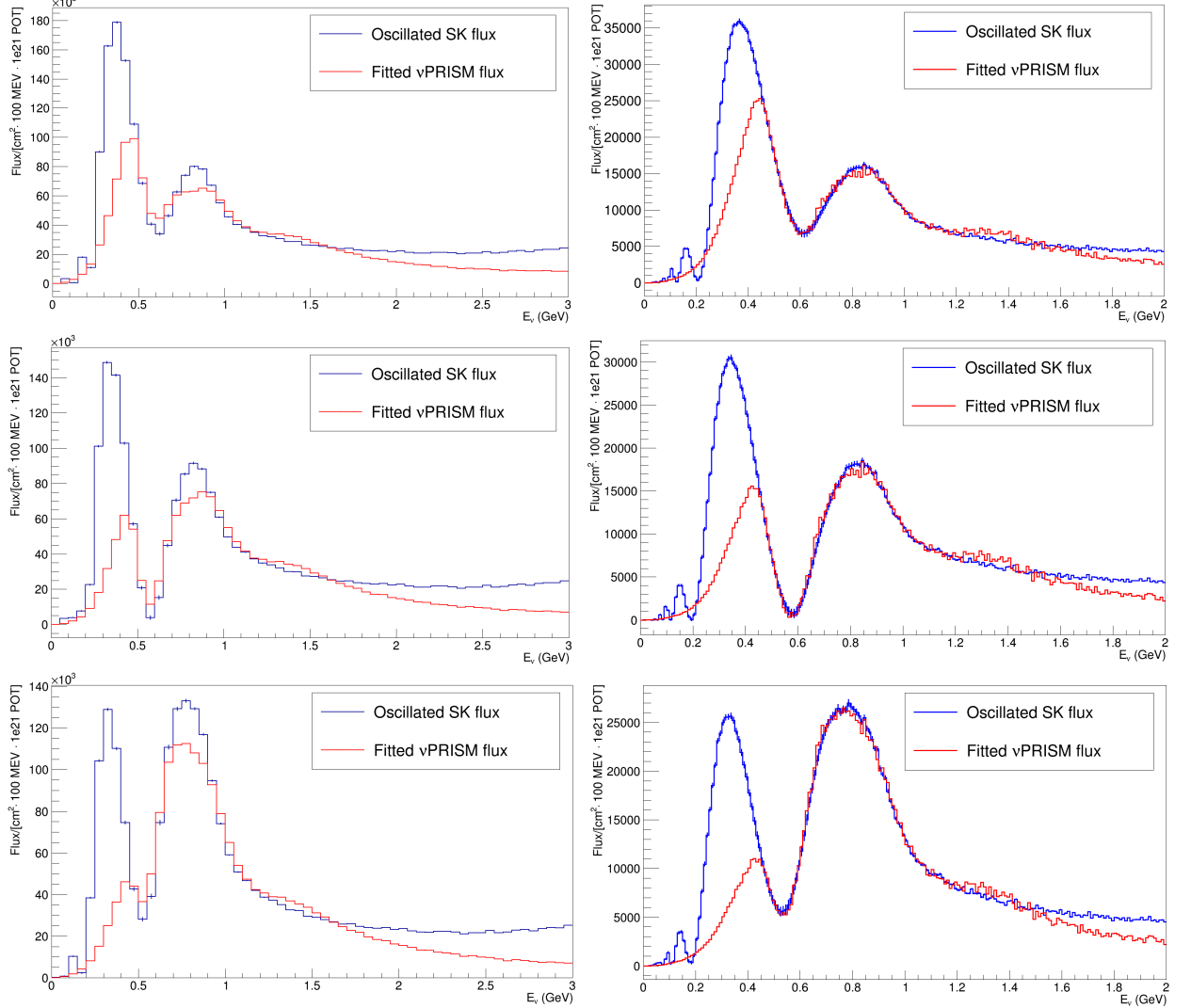


FIG. 16. Fits of the NuPRISM flux bins to oscillated Super-K fluxes are shown for three different sets of  $(\theta_{23}, \Delta m_{32}^2)$ : top -  $(0.61, 2.56 \times 10^{-3})$ , middle -  $(0.48, 2.41 \times 10^{-3})$ , and bottom -  $(0.41, 2.26 \times 10^{-3})$ . In the left column, the weights for the off-axis bins are forced to vary smoothly with off-axis angle, while in the right column they are allowed to vary more freely.

are incorporated into the analysis.

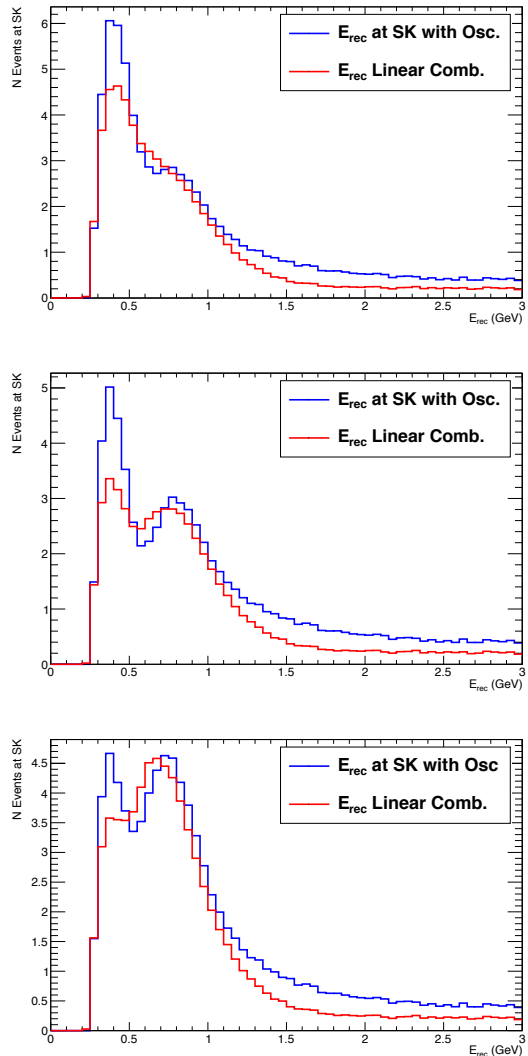


FIG. 17. The Super-K  $E_{rec}$  distributions and NuPRISM  $E_{rec}$  predictions corresponding to the flux fits in Figure 16 (left column) are shown prior to applying the  $\delta(E_{rec})$  correction factor.

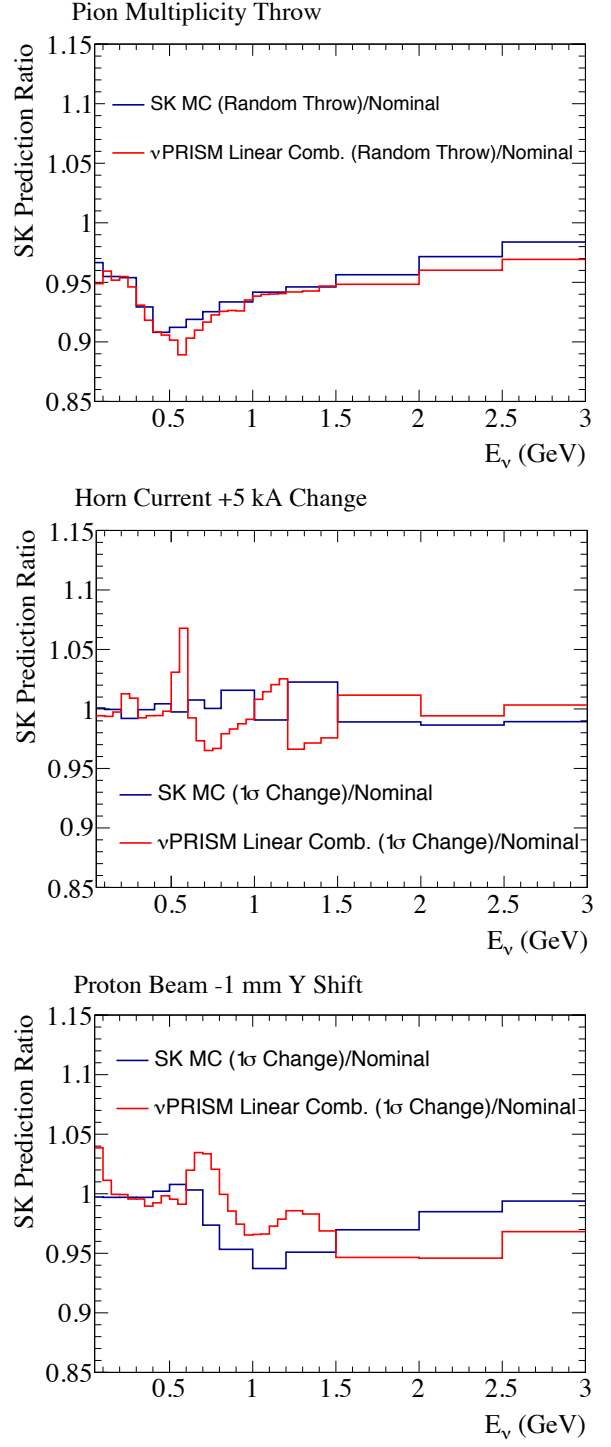


FIG. 18. Systematic uncertainties on the neutrino flux prediction due to pion production (top), horn current (middle), and proton beam y-position (bottom) are shown.

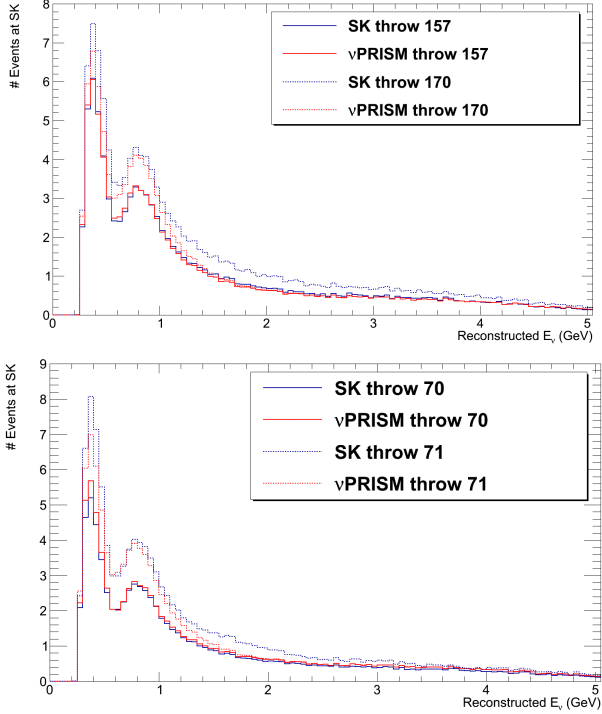


FIG. 19. Variations in the Super-K  $E_{rec}$  spectrum and the corresponding NuPRISM prediction are shown for 4 throws of all the flux and cross section parameters. Significant correlations exist between the near and far detector, which help to reduce the systematic uncertainty.

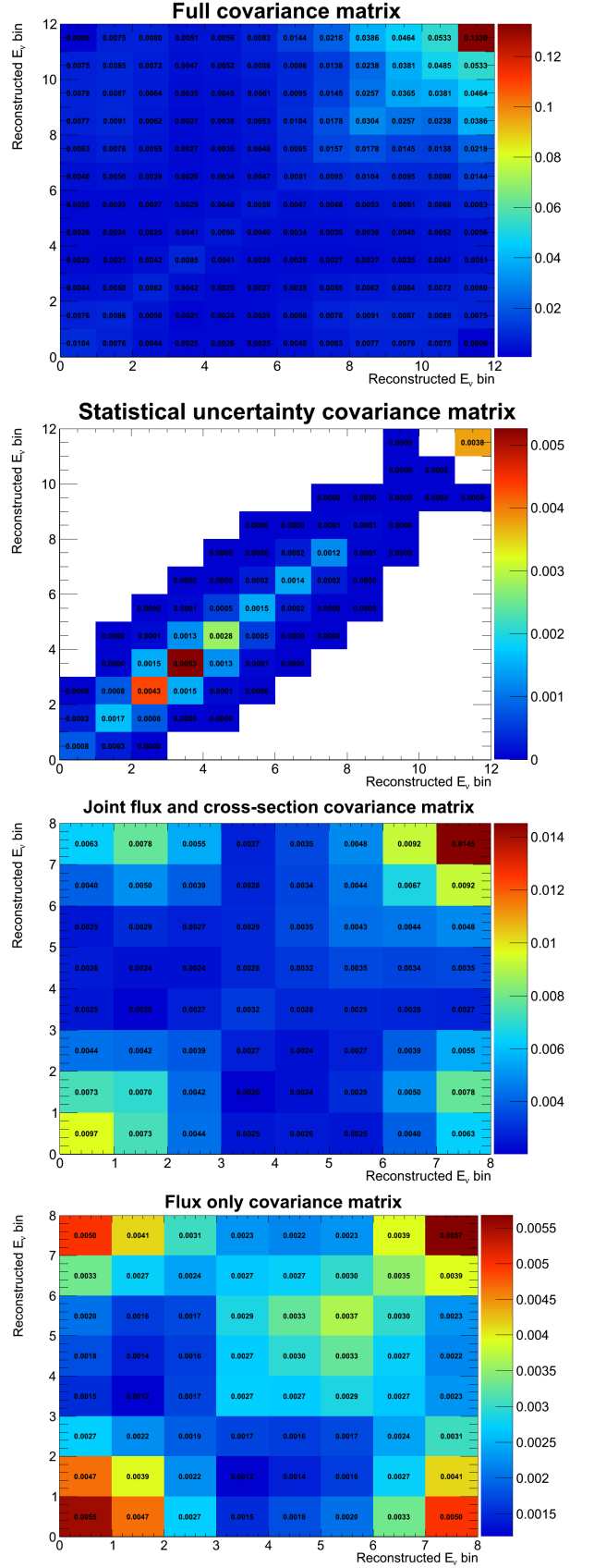


FIG. 20. Covariance matrices are shown (from top to bottom) for the total, statistical, systematic, and flux only uncertainties. The bin definitions (in GeV) are 0: (0.0,0.4), 1: (0.4,0.5), 2: (0.5,0.6), 3: (0.6,0.7), 4: (0.7,0.8), 5: (0.8,1.0), 6: (1.0,1.25), 7: (1.25,1.5), 8: (1.5,3.5), 9: (3.5,6.0), 10: (6.0,10.0), 11: (10.0,30.0)

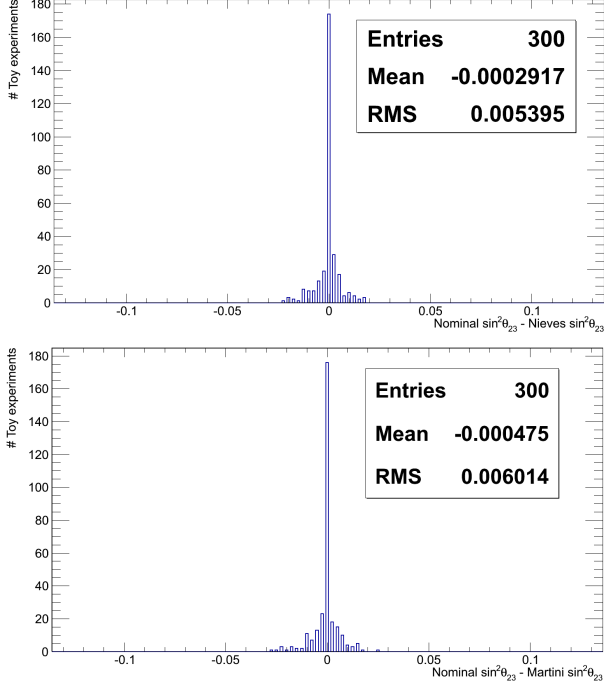


FIG. 21. The variation in the measured  $\sin^2 \theta_{23}$  due to mult-inucleon effects in the NuPRISM  $\nu_\mu$  analysis are shown. For the Nieves and Martini fake datasets, the RMS produces 1.0% and 1.2% uncertainties, respectively, with no measurable bias. This is a large improvement over the standard T2K results shown in Figure 13

## G. NuPRISM 1-Ring e-like Ring Measurements

Single ring e-like events in NuPRISM at an off-axis angle of  $2.5^\circ$  in principle provide a reliable estimate of the  $\nu_e$  appearance background at SK, since the near-to-far extrapolation correction is small. This includes beam  $\nu_e$ , NC $\pi^0$ , and NC single  $\gamma$  (NC $\gamma$ ) backgrounds with production cross section and detection efficiency in water folded in. For a  $\nu_e$  background study with better than  $\sim 10\%$  precision, more careful studies are required: for example, the  $\gamma$  background from outside the detector scales differently between the near and far detectors due to the differences in surface to volume ratio. Contributions from CC backgrounds, e.g. CC $\pi^0$  events created outside the detector, would also be different between near and far detector due to oscillation. Careful identification of each type of single ring e-like event is required. As described below, the NuPRISM capability of covering wide off-axis ranges makes such a study possible. It also enables relative cross section measurements between  $\nu_e$  and  $\nu_\mu$ , which are likely to be limiting systematic uncertainties for measuring CP violation.

### 1. Beam $\nu_e$ and $\nu_e$ cross section measurement

The beam  $\nu_e$  represents only 1% of the total neutrino flux and about 0.5% at the off-axis peak energy at  $E_\nu=600\text{MeV}$ . Thanks to the excellent  $\mu/e$  particle identification and  $\pi^0$  suppression in water Cherenkov detectors when using fiTQun, the  $\nu_\mu$  background is expected to be suppressed, similar to the suppression seen at Super-K. Since the beam  $\nu_e$ 's originate from three body decays of muons and kaons, their off-axis dependence is more mild than the dependence seen in the  $\nu_\mu$  flux. By taking advantage of the steep off-axis angle dependence of the  $\nu_\mu$  flux, it is possible to study background contamination in detail. For example, the  $\nu_\mu$  backgrounds are largely suppressed compared to beam  $\nu_e$  at an off-axis angle larger than 2.5 degrees. The beam  $\nu_e$  events at NuPRISM provide an opportunity to precisely study  $\nu_e$  cross sections, for which there is currently very little data available. The cross section difference between  $\nu_e$  and  $\nu_\mu$ , which does not cancel in the near to far detector extrapolation in  $\nu_\mu \rightarrow \nu_e$  appearance, is considered to be an eventual limitation of the CP violation sensitivity [22]. The differences in the  $\nu_e$  and  $\nu_\mu$  cross sections arise from kinematical phase space differences due to the difference in mass between electron and muons, radiative corrections, possible second class currents, which also depend on lepton mass, and nuclear effects [10].

NuPRISM provides a unique method for canceling the flux differences between  $\nu_e$  and  $\nu_\mu$ . Using a technique similar to that used in the NuPRISM  $\nu_\mu$  disappearance analysis, it is possible to use linear combinations of  $\nu_\mu$  measurements at different off-axis angles to reproduce the shape of the intrinsic  $\nu_e$  flux in the large off-axis

angle section of NuPRISM:

$$\Phi_{\nu_e}(E_\nu) = \sum c_i \Phi_{\nu_\mu}^i(E_\nu), \quad (4)$$

where  $\Phi_{\nu_e}(E_\nu)$  is the NuPRISM  $\nu_e$  flux of interest,  $\Phi_{\nu_\mu}^i(E_\nu)$  is the  $\nu_\mu$  flux at the  $i^{th}$  off-axis position and  $c_i$  is the weight factor for the  $i^{th}$  off-axis position. Using this combination, the ratio of the  $\nu_e$  and  $\nu_\mu$  double differential cross sections in momentum and angle can be directly measured, averaged over the  $\nu_e$  flux spectrum.

Figure 22 shows that the NuPRISM  $2.5^\circ - 4.0^\circ$  off-axis  $\nu_e$  flux can be reproduced by the linear combination of  $\nu_\mu$  fluxes for the  $0.3-1.5\text{ GeV}$  energy range. Above  $1.5\text{ GeV}$  the  $\nu_e$  flux cannot be produced since the fall-off of the  $\nu_\mu$  fluxes is steeper. However, this region will have little impact for the ratio measurement since the analysis will be applied in the limited lepton kinematic range where the NuPRISM muon acceptance is non-zero, cutting out forward produced high momentum leptons.

The Hyper-K experiment requires a 2-3% uncertainty on the  $\sigma_{\nu_e}/\sigma_{\nu_\mu}$  and  $\sigma_{\bar{\nu}_e}/\sigma_{\bar{\nu}_\mu}$  cross section ratios [15]. We have studied the potential precision of a  $\sigma_{\nu_e}/\sigma_{\nu_\mu}$  measurement in NuPRISM using the expected number of charged current  $\nu_e$  interactions with no final state pions in the  $2.5-4.0^\circ$  off-axis range of NuPRISM and a 2 m radius fiducial volume. The numbers are for an exposure of  $1.45 \times 10^{21}$  protons on target, a conservative estimate of the exposure in this off-axis angle range through the lifetimes of T2K and Hyper-K. Figure 23 shows the ratio of the electron neutrino over muon neutrino cross section for the neutrino energy range of  $0.3-1.5\text{ GeV}$  in NEUT 5.1.4.2. The difference is larger at lower energy where the impact of the lepton mass is larger. It is also the case that the CP violation effect increases with  $1/E_\nu$ , therefore measuring the cross section ratio in the  $0.3-0.6\text{ GeV}$  energy range is important. Figure 23 also shows the statistical and flux systematic uncertainties on the ratio of the electron neutrino and muon neutrino event rates in NuPRISM, where the muon neutrino events are combined using the linear combination described in Figure 22. Below  $0.6\text{ GeV}$ , the total statistical and flux uncertainties are 3.0% and 3.2% respectively. It may be possible to reduce the flux uncertainty with better hadron production measurements used for the flux modeling. If the hadron production uncertainty is reduced by a factor of two, the flux uncertainty below  $0.6\text{ GeV}$  is reduced to 1.7%.

Additional uncertainties on the  $\sigma_{\nu_e}/\sigma_{\nu_\mu}$  measurement are from the background subtraction and reconstruction. The  $\nu_e$  purity is expected to be 75% or greater and the experience of T2K and SK suggests that the neutral current backgrounds can be estimated with 10% precision. This corresponds to a 2.5% or better precision on the background subtraction. The rate of neutral current interactions themselves can be constrained by the selection of neutral current enhanced samples in NuPRISM. T2K has achieved 2.6% and 2.2% reconstruction uncertainties on the charged current  $\nu_e$  and  $\nu_\mu$  candidate samples in SK. We expect that NuPRISM can achieve a similar level

of systematic uncertainty with potential improvements from new calibration methods.

T2K will search for CP violation with samples of  $\nu_e$  and  $\bar{\nu}_e$  candidates in the SK detector that have  $\sim 10\%$  statistical precision. With a NuPRISM exposure of  $4.5 \times 10^{20}$  protons on target at each off-axis angle and horn polarity, the potential exposure during the nominal T2K period,  $\sigma_{\nu_e}/\sigma_{\nu_\mu}$  for neutrino energies of 0.3-0.6 MeV can be measured with a statistical precision as low as 5.4%. Over the range of 0.3-0.9 GeV, the statistical precision of the  $\sigma_{\nu_e}/\sigma_{\nu_\mu}$  measurement can reach 3.6%. Systematic uncertainties on the flux model, background subtraction and reconstruction can also be controlled at the level of 3% or better. Hence NuPRISM can measure the  $\sigma_{\nu_e}/\sigma_{\nu_\mu}$  cross section ratio to the level of precision required by T2K. This represents a significant improvement compared to the current treatment of the  $\sigma_{\nu_e}/\sigma_{\nu_\mu}$  cross section ratio where the ratio is derived from the model with no measurement to confirm the correct treatment in the model.

To fully take advantage of the Hyper-K accelerator neutrinos and sub-GeV atmospheric neutrinos to measure CP violation, the uncertainty on the  $\sigma_{\nu_e}/\sigma_{\nu_\mu}$  cross section ratio should be reduced to the 2-3% level. This means reducing each of the uncertainties from statistics, the flux model, the background and the reconstruction to the 1.0-1.5% level. If the 2.5-4.0° off-axis range receives an exposure of  $5.55 \times 10^{21}$  protons on target, the statistical uncertainty in the 0.3-0.6 GeV range can be reduced to 1.5%. This level of exposure can be achieved by additional data taking beyond the currently planned T2K and Hyper-K exposures, or by fully instrumenting the 2.5-4.0° off-axis angle region during the Hyper-K exposure. A reduction of hadron production uncertainties to 6% reduces the flux systematic uncertainty on the ratio to 1.7%. This uncertainty or better may be achieved with measurements of hadron production on a replica target and dedicated measurements on aluminum and iron targets to control the uncertainties from hadronic interactions outside of the target. Replica target data for T2K already exists and T2K is in the process of implementing the data in the T2K flux prediction. Preliminary studies suggest that hadron production uncertainties on the 90% of the flux from hadrons produced inside the target can be reduced to  $\sim 4\%$  with the replica target data. The background subtraction uncertainty may be reduced by the selection of even more pure  $\nu_e$  candidate samples. Studies of the relationship between the size and spacing of photo-detectors and the electron selection purity are now be carried out. Reduced reconstruction uncertainties may be achieved by the application of new calibration methods.

The measurement of the  $\sigma_{\bar{\nu}_e}/\sigma_{\bar{\nu}_\mu}$  ratio does present additional challenges beyond the  $\sigma_{\nu_e}/\sigma_{\nu_\mu}$  measurement. The lower antineutrino interaction cross section implies a smaller statistical sample, however Hyper-K will use a longer exposure with the antineutrino beam so as to balance the total event rates for neutrinos and antineutrinos. Hence, we expect a similar statistical precision

can be achieved for the  $\sigma_{\bar{\nu}_e}/\sigma_{\bar{\nu}_\mu}$  ratio. The  $\bar{\nu}_e$  candidate sample will include a larger neutral current background, so the purity of the electron reconstruction is most important for the antineutrino measurement. The antineutrino candidates also have a significant wrong-sign (neutrino) background. The wrong-sign background can be constrained by the measurement made in the neutrino beam.

This section shows that NuPRISM has the potential to make measurements of the  $\sigma_{\nu_e}/\sigma_{\nu_\mu}$  cross section ratio with precision better than 5% and with a plausible path to 2-3% precision. The precision measurement will require an efficient and pure selection of electron neutrino candidates. The experience of T2K suggests that pure samples of electron neutrinos can be selected using a water-Cherenkov detector. Currently, NuPRISM is the only proposed detector that can approach the level of precision for the  $\sigma_{\nu_e}/\sigma_{\nu_\mu}$  measurement on water required for Hyper-K.

## 2. Predicting oscillated $\nu_e$ for the appearance measurement

As discussed in the previous section, the cross section ratio of  $\sigma_{\nu_e}/\sigma_{\nu_\mu}$  can be measured using beam  $\nu_e$  and  $\nu_\mu$  interaction candidates in NuPRISM. The measured cross section ratio can be used to apply the NuPRISM extrapolation method to predict the  $\nu_e$  candidates at SK for the appearance measurement. Following the procedure used for the disappearance analysis, the oscillated+intrinsic beam  $\nu_e$  flux is described by a linear combination of the NuPRISM off-axis  $\nu_\mu$  fluxes:

$$\begin{aligned} & \Phi_{\nu_\mu}^{SK}(E_\nu) P_{\nu_\mu \rightarrow \nu_e}(E_\nu | \theta_{13}, \delta_{cp}, \dots) + \Phi_{\nu_e}^{SK}(E_\nu) \\ &= \sum c_i(\theta_{13}, \delta_{cp}, \dots) \Phi_{\nu_\mu}^i(E_\nu). \end{aligned} \quad (5)$$

$\Phi_{\nu_\mu}^{SK}(E_\nu)$  and  $\Phi_{\nu_e}^{SK}(E_\nu)$  are the predicted  $\nu_\mu$  and  $\nu_e$  fluxes at SK in the absence of oscillations.  $P_{\nu_\mu \rightarrow \nu_e}$  is the  $\nu_\mu$  to  $\nu_e$  oscillation probability.  $\Phi_{\nu_\mu}^i(E_\nu)$  is the  $i^{th}$  off-axis  $\nu_\mu$  flux in NuPRISM and the  $c_i$  are the derived coefficients that depend on the oscillation hypothesis being tested. Figure 22 shows the level of agreement that can be achieved between the linear combination of NuPRISM fluxes and the predicted SK  $\nu_e$  flux for a particular oscillation hypothesis. The agreement is excellent between 0.4 and 2.0 GeV. Below 0.4 GeV, the second oscillation maximum is not reproduced, but the rate from this part of the flux is small.

Using the derived  $c_i$  coefficients, the measured muon  $p, \theta$  distributions from NuPRISM are used to predict the SK  $p, \theta$  distribution for the  $\nu_e$  flux. An additional correction must be applied to correct from the predicted muon distribution for  $\nu_\mu$  interactions to the predicted electron distribution for  $\nu_e$  interactions. This correction is derived from the cross section models which are constrained by the ratio measurement described in the previous section.

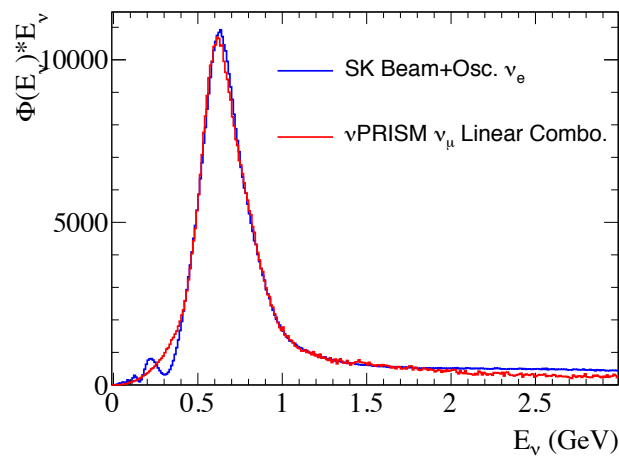
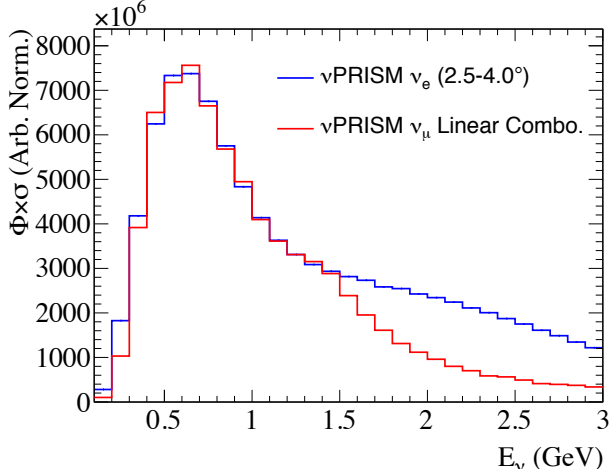


FIG. 22. Fits of the off-axis NuPRISM  $\nu_\mu$  fluxes to the NuPRISM  $2.5^\circ - 4.0^\circ$  off-axis  $\nu_e$  flux (top) and the oscillated+intrinsic beam  $\nu_e$  at SK (bottom) assuming  $\sin^2 2\theta_{13} = 0.094$ ,  $\delta_{cp} = 0$ ,  $\Delta m_{32}^2 = 2.4 \times 10^{-3} \text{ eV}^2$  and  $\sin^2 \theta_{23} = 0.5$ .

### 3. Backgrounds from $\nu_\mu$ 's

The backgrounds from  $\nu_\mu$  comes from  $\text{NC}\pi^0$  events with one  $\gamma$  missed,  $\text{NC}\gamma$  events ( $\Delta \rightarrow N\gamma$ ), CC events with  $e/\mu$  mis-ID,  $\gamma$ 's coming from  $\nu$  (mainly  $\nu_\mu$ ) interaction outside the detector (dirt or sand events). Because the  $\nu_\mu$  energy spectrum changes dramatically as a function of vertex positions (= off-axis angles) in nuPRISM, these background processes can be studied and verified by comparing their vertex distributions.

The  $\text{NC}\pi^0$  rate can be measured by detecting two  $\gamma$ 's in nuPRISM. By using the hybrid  $\pi^0$  technique used in T2K-SK analysis, the  $\pi^0$  backgrounds with a missing  $\gamma$  can be estimated using the beam  $\nu_e$  and Michel electrons as electron samples combined with a Monte Carlo  $\gamma$  event. The  $\text{NC}\pi^0$  rate can also be used to estimate the

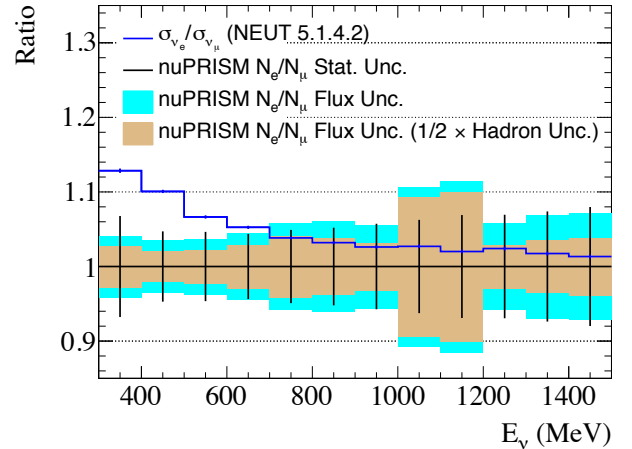


FIG. 23. The ratio of the electron neutrino CC0 $\pi$  cross section over the muon neutrino CC0 $\pi$  cross section in NEUT 5.1.4.2 (blue). The statistical uncertainty (for  $1.45 \times 10^{21}$  protons on target) on the ratio of NuPRISM electron neutrino to muon neutrino events is shown in black. The blue band shows the neutrino flux systematic uncertainty on the NuPRISM electron neutrino to muon neutrino event ratio. The tan band shows the flux systematic uncertainty if hadron production modeling uncertainties are reduced by a factor of 2 through new measurements.

$\text{NC}\gamma$  rate. As mentioned above, dirt/sand background is suppressed by having fully active outer veto detector and the fiducial volume cut. The vertex distribution of the  $\nu_e$  events as a function of the distance from the (upstream) wall provides an excellent confirmation of the suppression of the background, as is done in the T2K-SK analysis.

### H. Sterile Neutrino Sensitivity

The NuPRISM detector will provide a unique and sensitive search for sterile neutrinos in the  $\nu_\mu \rightarrow \nu_e$  channel, and eventually the  $\nu_\mu \rightarrow \nu_\mu$  channel, particularly when ND280 is incorporated into the analysis. The 1km location of NuPRISM for the off-axis peak energies of 0.5–1.0 GeV matches the oscillation maximum for the sterile neutrinos hinted by LSND and MiniBooNE. The presence or absence of an excess of  $\nu_e$  events as a function of off-axis angle will provide a unique constraint to rule out many currently proposed explanations of the MiniBooNE excess, such as feed-down in neutrino energy due to nuclear effects. The off-axis information also allows for a detailed understanding of the backgrounds, since they have a different dependence on off-axis angle than the oscillated signal events.

Figure 24 shows the single ring e-like events observed by MiniBooNE. There are several sources of events:

- Beam  $\nu_e$  from muons and kaons

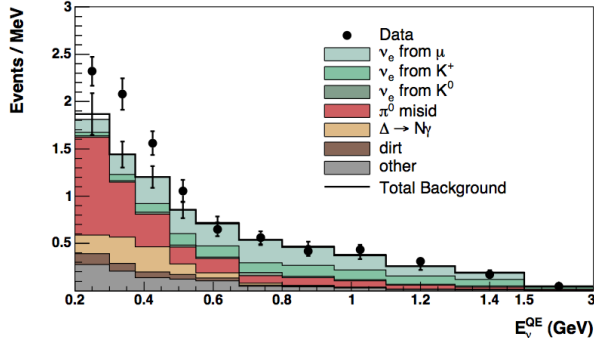


FIG. 24. Reconstructed neutrino energy distribution for the  $\nu_e$  appearance analysis of MiniBooNE [21].

- NC $\pi^0$  with one of the photons missed
- NC $\gamma$  ( $\Delta \rightarrow N\gamma$ )
- "Dirt" events: background  $\gamma$  coming from outside
- Others, such as CC events with  $\mu$  misidentified as electron
- Possible sterile neutrino contribution causing  $\nu_\mu \rightarrow \nu_e$  oscillation

There is a significant discrepancy between data and the Monte Carlo prediction. For precision  $\nu_e$  appearance studies, such as CP violation, it is essential to understand the origin of this discrepancy.

This section presents an initial, conservative sensitivity of NuPRISM to sterile neutrino oscillations. The present sensitivities are based on reconstruction efficiencies taken from Super-K, which performs much worse near the wall than NuPRISM due to the much coarser granularity provided by 20-inch PMTs relative to 8-inch PMTs. In addition, we do not yet incorporate any constraints on the backgrounds from in situ measurements in NuPRISM, and thus the full T2K neutrino cross section uncertainty is assumed for each background process. This is a particularly conservative assumption for NC $\pi^0$  events, since this process will be measured to high precision with NuPRISM. Finally, the T2K near detector, ND280, provides a secondary measurement at a much shorter baseline, and on a water target, which can further constrain flux and cross section uncertainties, however no information from ND280 has been incorporated into the measurement at this stage.

The LSND and MiniBooNE experiments detect an undetermined excess in their  $\nu_e$  and  $\bar{\nu}_e$  channels, which may be explained by sterile neutrino mixing with a  $\sin^2(2\theta_{\mu e}) \sim 10^{-3}$  and  $\Delta m_{41}^2 \sim 2\text{eV}^2$  in the 3+1 model [21].

The sensitivity studies in this section assume a 4 m inner detector and an exposure of  $4.5 \times 10^{20}$  p.o.t with a horn configuration enhancing neutrinos and defocusing antineutrinos. The possible  $\nu_e$  disappearance due to

TABLE IV. number of events for  $\nu_\mu$  selection and expected number of signal events for  $\nu_e$  selection (for each oscillation hypothesis)

$\nu_\mu$ Selection	
	Events
$\nu_\mu$	
	$1.689 \times 10^6$
$\nu_e$ Selection	
$(\sin^2(2\theta_{\mu e}), \Delta m_{41}^2)$	Events
$\nu_\mu \rightarrow \nu_e$	
(0.013, 0.43)	4158.1
(0.001, 1)	456.6
(0.005, 1)	2283.2
(0.01, 10)	3657.4
(0.001, 10)	365.7

sterile mixing is neglected as in the case of the LSND analysis. This is justified by the fact that  $\nu_e$  composes only 1% of the beam and the  $\nu_\mu \rightarrow \nu_e$  channel will be dominant. For simplicity, the effect of  $\nu_\mu$  disappearance was also neglected, although this is done in order to establish a first comparison to the LSND results. In the case where both  $\nu_e$  appearance and  $\nu_\mu$  disappearance signals are considered, the sensitivity to the mixing angle is expected to improve, and the results shown here can be considered a conservative estimate.

We test the simplest sterile neutrino model by adding to the standard three-neutrino parametrization one additional mass state, mainly sterile, with a squared mass difference to the other states  $\Delta m_{41}^2$ . Since the mixing with the sterile neutrino is dominant at short baselines, such as the nuPRISM baseline, the new mass state is expected to be of the order of  $1\text{eV}^2$ . Such heavy mass state, much larger than the two standard neutrino mass splittings, makes the two-neutrino approximation to be valid. The  $\nu_e$  appearance probability can be then written as:

$$P_{\nu_\mu \rightarrow \nu_e} = \sin^2(2\theta_{\mu e}) \sin^2 \left( 1.27 \Delta m_{41}^2 [\text{eV}^2] \frac{L[\text{km}]}{E[\text{GeV}]} \right) \quad (6)$$

where  $L$  is the neutrino flight path fixed at 1 km, and  $E$  is the energy of the neutrinos. The effective mixing angle could be rewritten in terms of the extended PMNS matrix,  $U$ , in the way  $\sin^2(2\theta_{\mu e}) = 4|U_{\mu 4}|^2|U_{e 4}|^2$ . We consider an analysis on both the reconstructed energy ( $E_{\text{Rec}}$ ) and the off-axis angle (OAA) shape information, so both rate and shape are taken into account by building bidimensional binned templates. Although we are neglecting any possible effect coming from a short baseline muon neutrino disappearance, we use muon neutrino candidate events to constrain flux and cross section uncertainties affecting the estimation of the nue signal events.

Both  $\nu_\mu$  selection events and  $\nu_\mu \rightarrow \nu_e$  appearance signal events for different oscillation hypothesis are presented in Table IV.

The systematic errors due to the flux and cross-section

uncertainties are included through a covariance matrix calculated using toy Monte Carlo throws. We performed a  $\chi^2$  test for a binned template of 10  $E_{Rec}$  bins and 10 OAA bins between 0.2 GeV and 4 GeV for both  $\nu_e$  and  $\nu_\mu$  selections, in order to obtain the expected sensitivity in the bidimensional oscillation parameter space ( $\sin^2(2\theta_{\mu e})$ ,  $\Delta m_{41}^2$ ). For each oscillation hypothesis, the  $\chi^2$  value is given by:

$$\chi^2 = \vec{n}_s(\sin^2(2\theta_{\mu e}), \Delta m_{41}^2)^T \times V^{-1} \times \vec{n}_s(\sin^2(2\theta_{\mu e}), \Delta m_{41}^2) \quad (7)$$

where  $\vec{n}_s$  is a vector of 200 elements (in  $E_{Rec}$  and OAA bins) containing the number of expected  $\nu_e$  appearance signal events in the first 100 entries, followed by the expected number of events due to the muon neutrino disappearance. These last entries are all set to 0 since we assumed no  $\nu_\mu$  disappearance.  $V$  is thus a  $200 \times 200$  covariance matrix including the statistical and systematic errors for both  $\nu_e$  and  $\nu_\mu$  selections. This  $V$  matrix is constructed in the following way:

$$V = \begin{pmatrix} W_{ee} & W_{e\mu} \\ W_{\mu e} & W_{\mu\mu} \end{pmatrix} \quad (8)$$

where  $W_{ee}$  and  $W_{\mu\mu}$  only involve statistical and systematic errors coming only from  $\nu_e$  and  $\nu_\mu$  selections, respectively; while  $W_{e\mu}$  and  $W_{\mu e}$  take into account the correlations between both selections. In Figure 25, we can see that the correlations between  $\nu_e$  and  $\nu_\mu$  ( $W_{e\mu}$  and  $W_{\mu e}$ ) are large enough as the ones from only  $\nu_e$  ( $W_{ee}$ ).

### 1. Background

The background after the final event selection is composed of electron-like reconstructed events coming from two different sources: a) the intrinsic  $\nu_e$  contamination of the incident  $\nu_\mu$  neutrino flux; and b) events coming from  $\nu_\mu$  neutrinos which are reconstructed as electron-like events. The two background components have been investigated respectively in terms of their origin (parent particle) or their interaction mode. The  $\nu_e$  intrinsic background mainly come from  $\mu^+$  decay and, at higher energy, from  $K^+$  decay. Background events coming from  $\nu_\mu$  have been instead classified into 5 categories based on the neutrino interaction mode. We distinguish between events having a  $\pi^0$  in the final state ( $CC\nu_\mu\pi^0$  and  $NC\nu_\mu\pi^0$ ),  $CCQE\nu_\mu$  (misreconstructed as electron-like) and other events coming from both NC and CC but with no  $\pi^0$  in the final state. Figure 26 show the Monte Carlo energy spectrum for background events broken down into its different contributions. A  $\nu_e$  appearance signal simulated for oscillation hypothesis  $\Delta m_{41}^2 = 0.43 \text{ eV}^2$  and  $\sin^2(2\theta_{\mu e}) = 0.013$  is also shown. The dominant component comes from  $NC\nu_\mu\pi^0$  events, where a photon coming from the  $\pi^0$  decay has been identified as an electron.

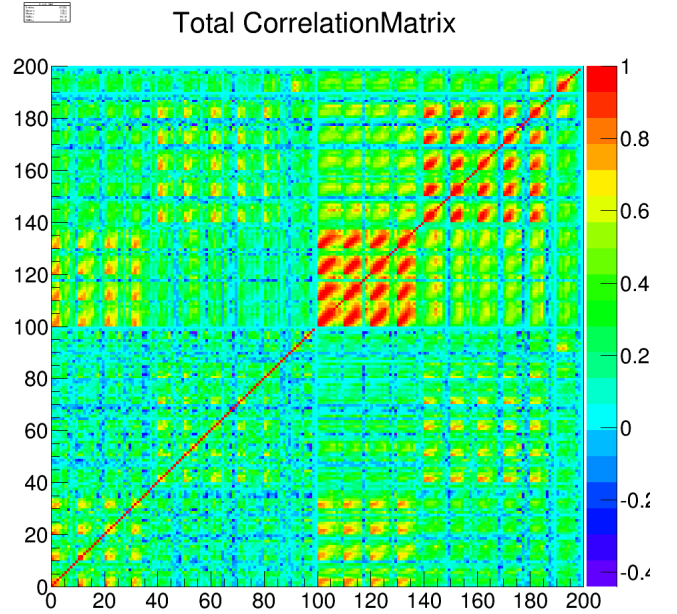


FIG. 25. Correlation matrix corresponding to  $V$  covariance matrix, including both flux and cross-section systematic uncertainties

The  $\nu_\mu$  background, dominant in the low energy region, quickly decrease and its contribution become almost negligible for  $E_{rec} \sim 1 \text{ GeV}$ . On the contrary, the  $\nu_e$  intrinsic background presents a longer tail, characteristic of the 3-body decay kinematics from which they are generated.

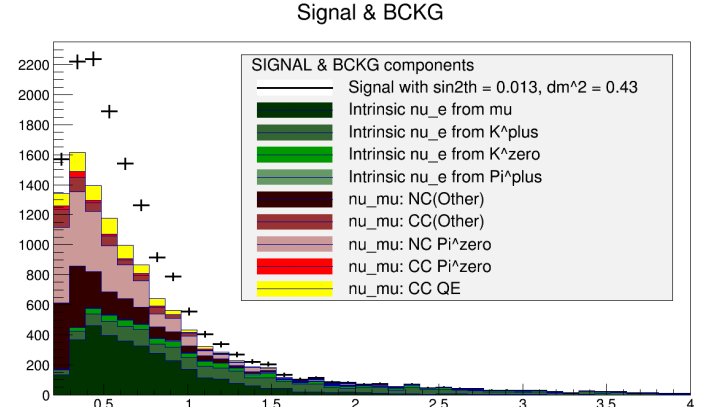


FIG. 26. Background broken-down by component and signal for sterile mixing parameters  $\sin^2(2\theta_{\mu e}) = 0.013$  and  $\Delta m_{41}^2 = 0.43 \text{ eV}^2$

A unique feature of measuring sterile neutrinos in NuPRISM is the variation in background composition as a function of the off-axis angle. This can be seen by dividing the off-axis range of 1.1 to 3.9 degrees into 4 bins, as shown in Figure 27. The signal and background shapes show significantly different responses to changes

TABLE V. Expected number of events for every component of the background as a function the OAA.

OAA( $^{\circ}$ )	1.1-1.8	1.8-2.5	2.5-3.2	3.2-3.9
<b>BCKG: <math>\nu_e</math> Component</b>				
$K^+$	443	440	391	347
$\mu^+$	1168	949	669	423
$K^0$	184	141	155	125
$\pi^+$	17	25	22	9
<b>BCKG: <math>\nu_{\mu}</math> Component</b>				
$CCQE\nu_{\mu}$	332	196	98	44
$CC\nu_{\mu}\pi^0$	78	31	15	8
$NC\nu_{\mu}\pi^0$	1454	558	231	131
$CC\nu_{\mu}Other$	328	129	32	24
$NC\nu_{\mu}Other$	1029	368	198	119

in the off-axis angle.

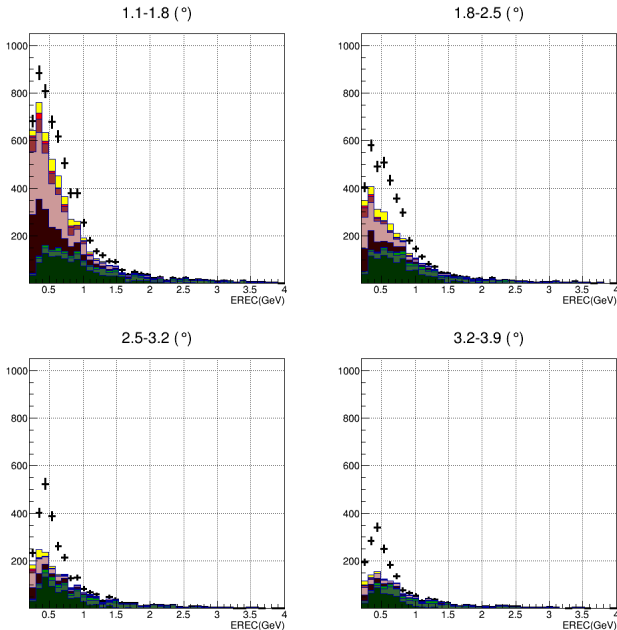


FIG. 27. Background broken-down by component and for 4 slices in OAA range, and signal for sterile mixing parameters  $\sin^2(2\theta_{\mu}e) = 0.013$  and  $\Delta m_{41}^2 = 0.43 \text{ eV}^2$

Table V summarizes the signal and background event rates as a function of off-axis angle. Both the NC and CC components are reduced by an order of magnitude when moving to the highest off-axis angles. On the contrary, the intrinsic background components (especially coming from  $K^+$  and  $K^0$ ) almost remain constant. This characteristic behavior of the intrinsic background can also be used to isolate a pure sample of  $\nu_e$  events to perform cross-section measurements.

## 2. Systematics

To estimate of the size of the flux and cross section uncertainties, we consider the diagonal terms of the covariance matrix built separately for each source of background: for the intrinsic component ( $K^+$ ,  $K^0$ ,  $\mu^+$  and  $\pi^+$ ), and also for the NC ( $NC\nu_{\mu}\pi^0$  and  $NC\nu_{\mu}Other$ ) and CC ( $CC\nu_{\mu}\pi^0$  and  $CC\nu_{\mu}Other$ ) components.

From this study, we observe that the NC component is the largest source of systematic errors only in the low OAA and reconstructed energy region. Furthermore, we noticed that the CC component error sizes are quite smaller than the NC. In the high OAA and reconstructed energy region, the dominant source of systematics is instead related to the intrinsic  $\nu_e$  component.

Since this intrinsic component is an irreducible background, we conclude that the main efforts should go in the direction of reducing the rest of the components of the background (specially the NC).

## 3. Sensitivities

The  $\chi^2$  is computed for each point of a bidimensional grid and the constant  $\Delta\chi^2$  method is applied to determine the contours for the regions excluded at the 90%,  $3\sigma$  and  $5\sigma$  C.L. The resulting nuPRISM sensitivity is presented in Figure 28 (top) and compared to the LSND allowed region.

Since the current NuPRISM event selections are based on the 20-inch PMTs of Super-Kamiokande, we expect a significant improvement in the identification of  $\pi^0$  background events when using a full simulation including 8-inch PMTs. In addition, The  $\pi^0$  production rate will be precisely measured in NuPRISM using the 2-ring e-like selected sample, which will significantly reduce the currently assumed systematic error assigned to the  $\pi^0$  background events. Both of these improvements can be studied by reducing the size of the  $\pi^0$  background. Figure 28 (bottom) shows the effect on the sensitivity of a 30% reduction in the  $\pi^0$  background.

Despite the current conservative assumptions on the size of the NC background and its uncertainty, NuPRISM can provide a precise check of the LSND/MiniBooNE oscillation signal, comparable to the sensitivity of the upcoming Fermilab short-baseline program, by covering the LSND 90% allowed range at  $3\sigma$  for all values of  $\Delta m^2$  outside of  $2 \text{ eV}^2$ . As the analysis matures, and information from ND280 is incorporated, additional improvements in the sensitivities are expected.

## I. Atmospheric neutrino CP violation

Atmospheric neutrinos provide baseline lengths of up to 13,000 km which can be tagged by the zenith angle of the charged lepton produced in the charged current interactions of the neutrinos. The availability of neutrinos and

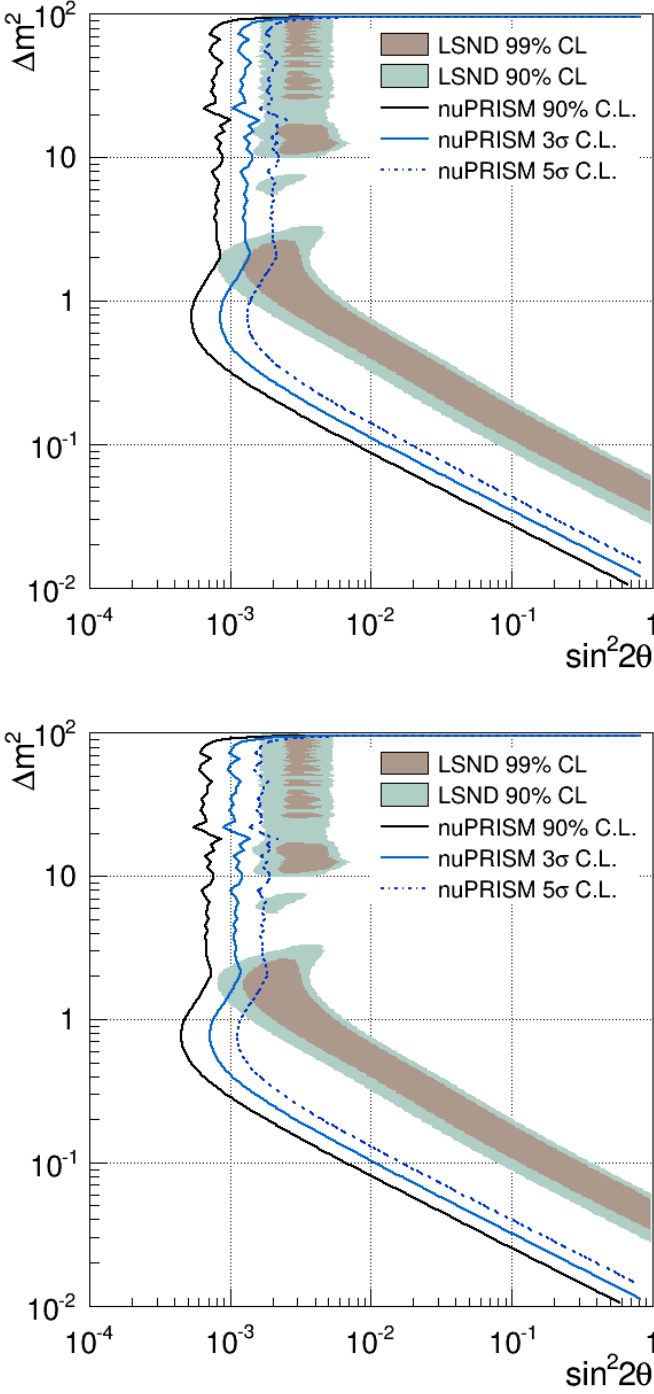


FIG. 28. 90%, 3 $\sigma$  and 5 $\sigma$  C.L. expected sensitivities for an exposure of  $4.6 \times 10^{20}$  p.o.t. for statistical uncertainties with flux and cross-section systematic uncertainties. The sensitivity curves are shown taking into account the whole background (top) and a 30% reduction of the  $NC\nu_\mu$  background (bottom). For comparison, the LSND allowed region at 90% and 99% C.L. is also showed.

antineutrinos of both electron and muon flavors over this wide range of baseline lengths and energies provides rich information about the neutrino oscillations. The matter effect gives additional information such as determination of the mass hierarchy.

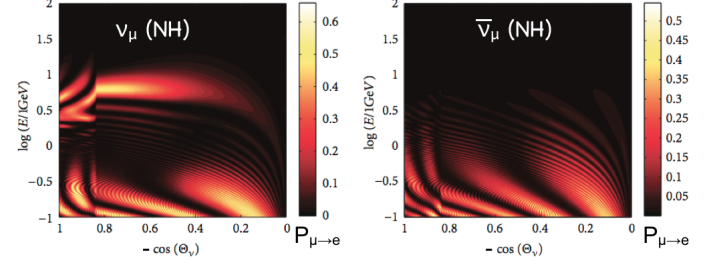


FIG. 29.  $\nu_\mu \rightarrow \nu_e$  oscillation probability in neutrino energy,  $\log_{10}(E_\nu)$ , versus zenith angle,  $\cos \theta_Z$ , space (oscillogram). Left plot is for neutrinos with the normal hierarchy and the right plot is for antineutrinos with the normal hierarchy.

Figure 29 shows the  $\nu_\mu \rightarrow \nu_e$  oscillation probability assuming the normal hierarchy for neutrinos (left) and antineutrinos (right). The vertical axis is the neutrino energy,  $\log_{10} E_\nu$ , and the horizontal axis is the zenith angle,  $\cos \theta_Z$ . There is a large enhancement for upward going ( $\cos \theta_Z \sim -1$ ) neutrinos at several GeV but not for antineutrinos. In the case of inverted hierarchy, the resonance appears for antineutrinos instead of neutrinos, allowing the study of the neutrino mass hierarchy. There is also a strong interference patterns in the sub-GeV region, which comes from the  $\theta_{12}$  oscillation. The atmospheric neutrino flux is the largest in this sub-GeV region, and SuperK has already accumulated more than 10,000 sub-GeV  $\nu_e$  events over 5000 days of running.

The subGeV oscillation pattern comes from the  $\nu_\mu \rightarrow \nu_e$  and  $\bar{\nu}_\mu \rightarrow \bar{\nu}_e$  appearance oscillations as well as the original cosmic  $\nu_e$ 's and  $\bar{\nu}_e$ 's oscillating away (disappearance). Since the anti-neutrino cross section is a factor of 4 smaller than neutrino cross section in the sub-GeV energy range, mainly neutrinos are detected. Because  $\nu_e$ 's can disappear into  $\nu_\mu$  and  $\nu_\tau$ , the probability of  $\nu_e$  disappearance,  $P_{e\mu} + P_{e\tau} \sim 2P_{e\mu}$ , assuming maximal  $\theta_{23}$  mixing  $\sin 2\theta_{23}=1$ , which leads to  $P_{e\mu} \sim P_{e\tau}$ . Since the  $\nu_\mu$  to  $\nu_e$  flux ratio,  $r = \Phi_{\nu_\mu}/\Phi_{\nu_e} \sim 2$ , the number of  $\nu_e$ 's that are added from  $\nu_\mu \rightarrow \nu_e$  appearance is  $rP_{\mu e} \sim 2P_{\mu e}$ . If the T (CP) is conserved,  $P_{e\mu} = P_{\mu e}$ , the oscillation effect in observed atmospheric  $\nu_e$  is cancelled and we would not be able to observe the oscillation as shown in Figure 30. This natural cancellation provides an opportunity for a sensitive tests for CP violation as well as maximal  $\theta_{23}$  mixing.

The above simplified discussion ignores the matter effect, which enhances the oscillation effects, as described in Reference [23]:

$$P_{e\mu} = c_{23}^2 |A_{e2}|^2 + s_{23}^2 |A_{e3}|^2 + 2s_{23}c_{23} \operatorname{Re}(e^{i\delta} A_{e2}^* A_{e3})$$

$$P_{e\tau} = s_{23}^2 |A_{e2}|^2 + c_{23}^2 |A_{e3}|^2 - 2s_{23}c_{23} \operatorname{Re}(e^{i\delta} A_{e2}^* A_{e3}),$$

where  $A_{e2}$  and  $A_{e3}$  are the transition amplitudes to the mass eigenstates in the earth matter. For the maximal  $\theta_{23}$  mixing or  $s_{23}^2 = c_{23}^2 = 0.5$  and  $r=2$ , the oscillation effect for  $\nu_e$  flux  $\Phi_e$  compared to without oscillation  $\Phi_e^0$  becomes:

$$\begin{aligned}\Phi_e/\Phi_e^0 &= r \times P_{\mu e} - P_{e\mu} - P_{e\tau} = 2P_{e\mu}(-\delta) - P_{e\mu} - P_{e\tau} \\ &= Re(e^{i\delta} A_{e2}^* A_{e3}) = |A_{e2} A_{e3}| \cos(\delta + \phi),\end{aligned}$$

where we used the relation  $P_{\mu e}(\delta) = P_{e\mu}(-\delta)$  and  $\phi = \arg(A_{e2}^* A_{e3})$ . The oscillation effect is enhanced by the matter effect and is proportional to  $\cos(\delta + \phi)$ .

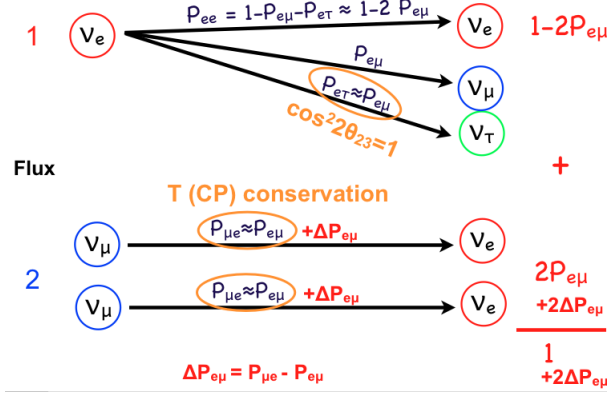


FIG. 30. Assuming that the atmospheric  $\nu_\mu$  and  $\nu_e$  ratio is two, the maximum  $\theta_{23}$  mixing ( $\theta_{23} = 45^\circ$ ), and T(CP) conservation, the oscillation effect in  $\nu_e$  observed spectrum is totally cancelled. If there is T(CP) violation ( $\Delta CP$ ), the observed  $\nu_e$  spectrum would show the oscillation effect.

Since the high energy muons above several GeV have more chance to reach the ground before decaying, the ratio  $r$  becomes significantly larger than 2 and the cancellation does not work anymore. This allows the study of the  $\nu_\mu \rightarrow \nu_e$  matter oscillation resonance at several GeV to study the mass hierarchy.

Figure 31 shows the  $\nu_\mu \rightarrow \nu_e$  appearance probability as a function of the neutrino energy for three typical zenith angles,  $\cos Z = -1.0, -0.8, -0.4$ , where sub-GeV resonance effect is enhanced [24]. The sub-GeV and multi-GeV resonances come from the  $\theta_{12}$  and  $\theta_{23}$  matter effects, respectively. The colour of the curves corresponds to different CP phases. The blue curve, which is the smallest, represents  $\delta_{CP}=0$  case, and the other colour lines represent for different  $\delta_{CP}$  values. The CP violation effect is as large as 20% in the sub-GeV neutrino energy range.

The zenith angle resolution, which is the correlation between the initial neutrino direction and the out-going lepton direction, starts to become measureable for the neutrino energies above  $E_\nu = 400-500$  MeV.

Figure 32 shows the expected zenith angle distributions for the standard SK Monte Carlo for sub-GeV electron-like events with 0 and 1 decay electrons and  $\mu$ -like events with 1 and 2 decay electrons. The colour of the lines are

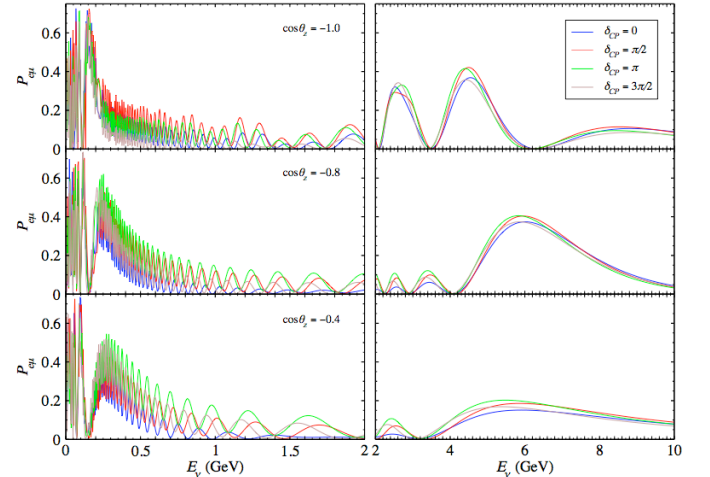


FIG. 31.  $\nu_\mu \rightarrow \nu_e$  oscillation probability  $P_{\mu e}$  as a function of neutrino energy  $E_\nu$  for the zenith angle of  $\cos_{\text{zenith}} = -1.0, -0.8, -0.4$  for the CP phase  $\delta_{CP} = 0$ (blue),  $\pi/2$ (red),  $\pi$ (green),  $3\pi/2$ (orange) [24]

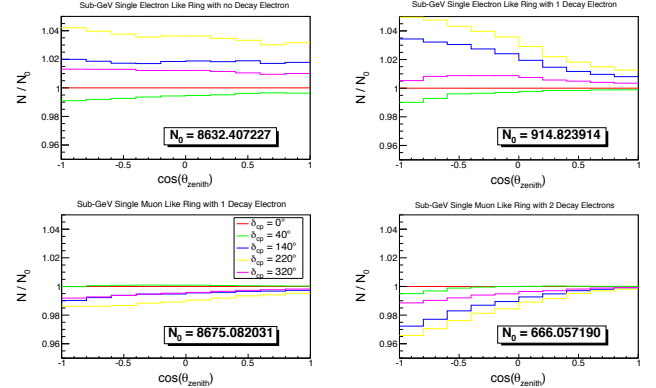


FIG. 32. Expected zenith angle distributions for sub-GeV electron-like with 0 and 1 decay electrons (top left and right) and  $\mu$ -like events with 1 and 2 decay electrons (bottom left and right). The colour of the lines are for different CP violation phases.

for different CP violation phases. As much as a several % CP violation effect is expected.

Figure 33 shows the current preliminary CP sensitivity of SK data along with T2K sensitivity presented at the Neutrino2014 conference. The  $\delta_{CP} = 0$  is disfavoured at  $\Delta_x^2$  of 3.5 or at 90%CL, which is better than T2K. On the other hand, the sensitivity is worse than T2K in rejecting  $\delta_{CP} = \pi$ . The  $\delta_{CP} = \pi$  region can be explored by using antineutrinos which can be tagged by detecting neutrons with existing  $np \rightarrow d\gamma$  trigger (Eff.=20%) or the planned Gd upgrade (GAZOOKS!). The antineutrino events provide better zenith angle measurements due to their strong forward scattering and thus enhance the signal sensitivity, although the statistical power is lower due to the smaller antineutrino interaction cross section.

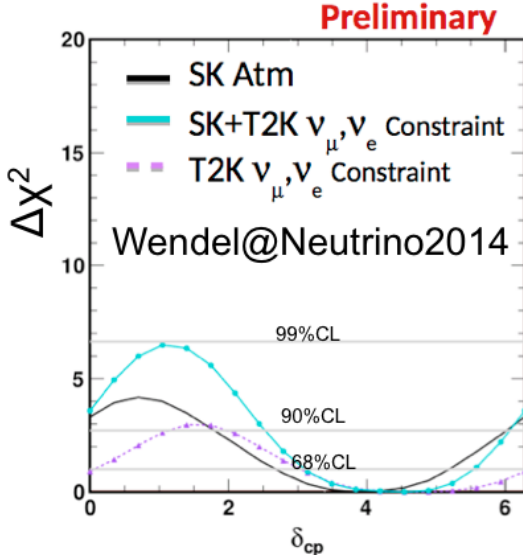


FIG. 33. Preliminary CP sensitivity of SK data along with T2K sensitivity presented at the Neutrino2014 conference.

The current SK CP sensitivity is limited by the systematic uncertainties on the atmospheric neutrino flux and cross section. Figure 34 shows the expected CP sensitivity to exclude  $\delta_{CP} = 0$  for given  $\delta_{CP} = 0$  when the systematic uncertainty is not considered. The black curve is with 50 bins in energy and zenith angle. The  $\Delta\chi^2$  is more than 16 ( $4\sigma$ ) at the best fit point and 13 ( $3.6\sigma$ ) at  $\delta_{CP} = -\pi/2$ , which is the current best fit point. If we consider integrated date till 2020, the expected CP sensitivity exceeds  $5\sigma$  at the best fit point and exceeds  $4\sigma$  at  $\delta_{CP} = -\pi/2$  for the statistical sensitivity. The red curve is zenith angle binning only and blue curve is energy binning only. Both energy and zenith angle contribute to the CP sensitivity. The likelihood to reject  $\delta_{CP} = \pi$ , which is also CP conserving, can be obtained by shifting the horizontal axis by  $\pi$ . There is little sensitivity for the current best fit point ( $\delta_{CP} = -\pi/2$ ), which corresponds to  $\delta_{CP} = \pi/2$  point in the figure.

Atmospheric neutrinos provide wide range of baseline length, energy, and neutrino species. As seen above, sub-GeV atmospheric neutrinos have good statistical sensitivity even with the data already taken by SK. However, the atmospheric neutrino results are often limited by systematic uncertainties which are difficult to quantify.

The main systematic uncertainties in the atmospheric neutrino oscillation come from the atmospheric neutrino flux and neutrino cross sections. One effective way to reduce the systematic uncertainties is taking the ratio between  $\nu_e$  and  $\nu_\mu$  candidates. The  $\nu_e$  and  $\nu_\mu$  flux ratio prediction below a few GeV is almost independent of the flux models as they are originating from the same parent pions produced in the atmosphere. The main uncertainty comes from the charge asymmetry in pion production in the atmosphere which creates the  $\nu_e$  and  $\bar{\nu}_e$  asymmetry. The systematic uncertainty is estimated to be about 5%

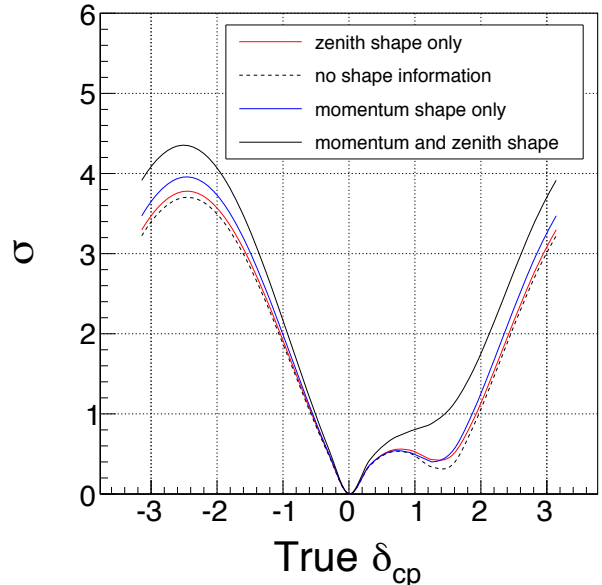


FIG. 34. CP sensitivity ( $\sigma$ ) when only the statistical uncertainty is considered for the existing 5000-days of SK data set. The black curve is with 50 bins in energy and 50 bins in zenith angle and the black dashed line is normalization only (no binning). The red curve and blue curves are for only zenith angle or energy binning, respectively.

in an earlier study [25]. The cross section systematics come from the difference between the  $\nu_e$  and  $\nu_\mu$  interaction cross sections, which are in the first order the same at a few % level. The difference comes from the phase space difference due to electron and muon mass difference and the radiative corrections and possible other unknown effects. This can be addressed by nuPRISM as discussed below. To match the statistical uncertainty of 1% ( $\sim 10,000$  events) to perform the precision CP measurement, further reduction in systematic uncertainties is essential.

The neutrino flux uncertainty comes from the primary cosmic ray flux and the hadron production in the atmosphere. Recently, there has been a big progress towards understanding the atmospheric neutrino flux. The new AMS result [26] announced in April 2015 provides a very precise measurement of the primary cosmic ray flux at a wide range of energies with a systematic uncertainty of 1-2% making this component to the systematic uncertainty to  $\nu_e$  and  $\nu_\mu$  flux ratio negligible. The CERN NA61 experiment developed a very precise measurement of hadron production at the 5% level which greatly improved the systematic uncertainty of the neutrino flux for the T2K long baseline neutrino experiment [27]. However, the current CERN SPS beamline used by NA61 is capable of delivering the beam above 15 GeV/c, and there remains large systematic uncertainty (tens of %) in hadron production cross section below 15 GeV/c which is the main source of atmospheric neutrino flux uncer-

tainty. A discussion is taking place with NA61 group to modify the SPS beamline to study hadron production in the primary proton energy of 1-15 GeV/c in NA61 for the atmospheric neutrino studies as well as T2K and other long baseline experiments.

For the neutrino cross section, the critical measurement is the cross section difference between  $\nu_e$  and  $\nu_\mu$ . nuPRISM will improve this as discussed in a previous section. It is also important to study the differential cross section in lepton direction and energy, as the dependence of these variables improves the sensitivity significantly as shown in Figure 34.

With a new hadron production measurements considered by NA61 and the sub-GeV neutrino cross section measurement by nuPRISM, along with the recent very precise AMS primary cosmic ray measurement, precise atmospheric neutrino oscillation study including CP violation would be possible using the existing SK data set.

### J. $\bar{\nu}_\mu$ Measurements

In principle, the NuPRISM technique of using multiple off axis angles to measure the oscillated  $p_\mu$  and  $\theta_\mu$  for each oscillated flux will work for anti-neutrinos as well. However, when running the T2K beam in anti-neutrino mode, there is a significant wrong-sign background from neutrino interactions. To disentangle these neutrino and anti-neutrino interactions, linear combinations of the neutrino-mode data can be used to construct the wrong-sign flux in anti-neutrino mode, analogous to the procedure used in Section II F to construct the Super-K oscillated spectra and in Section II G 1 to construct the electron neutrino spectrum. Hence, the neutrino flux in the anti-neutrino mode is described with the linear combination of neutrino mode fluxes:

$$\Phi_{\nu_\mu}^{\bar{\nu}\text{mode}}(E_\nu, \theta_{oa}) = \sum c_i(\theta_{oa}) \Phi_{\nu_\mu}^{i,\nu\text{mode}}(E_\nu). \quad (9)$$

$\Phi_{\nu_\mu}^{\bar{\nu}\text{mode}}(E_\nu, \theta_{oa})$  is the anti-neutrino mode  $\nu_\mu$  (wrong-sign) flux for a given off-axis angle  $\theta_{oa}$ .  $\Phi_{\nu_\mu}^{i,\nu\text{mode}}(E_\nu)$  is the neutrino mode  $\nu_\mu$  (right-sign) flux for the  $i^{\text{th}}$  off-axis bin and  $c_i$  is the weight for the  $i^{\text{th}}$  off-axis bin that depends on the off-axis angle for which the anti-neutrino mode wrong sign flux is being modeled.

Linear combinations to reproduce the wrong-sign  $1.0 - 2.0^\circ$ ,  $2.0 - 3.0^\circ$  and  $3.0 - 4.0^\circ$  anti-neutrino mode fluxes are shown in Figure 35. As with the combinations to produce the  $\nu_e$  flux, the agreement is good up to about 1.5 GeV in neutrino energy. As discussed in Section II G 1, it is less important to reproduce the high energy part of the flux since high energy interactions are suppressed by the event topology selected and the muon acceptance of NuPRISM.

As shown Figure 36, there is significant correlation between the wrong-sign neutrino flux in anti-neutrino mode and the neutrino-mode flux, so the flux uncertainties will

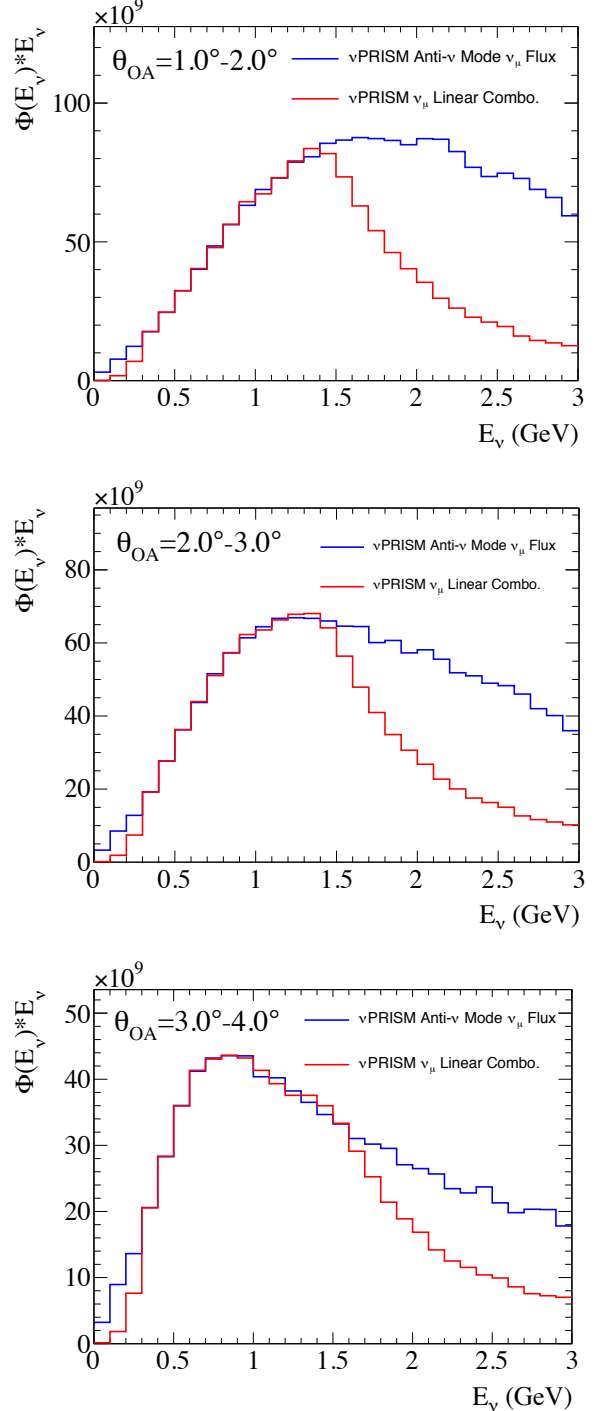


FIG. 35. The NuPRISM anti-neutrino mode wrong-sign  $\nu_\mu$  fluxes for  $1.0 - 2.0^\circ$  (top),  $2.0 - 3.0^\circ$  (middle) and  $3.0 - 4.0^\circ$  (bottom), and the NuPRISM linear combinations of neutrino mode  $\nu_\mu$  fluxes.

give some cancelation using this method. After subtracting the neutrino background, the remaining  $\bar{\nu}_\mu$  events can then be combined as in the neutrino case to produce oscillated spectra at Super-K.

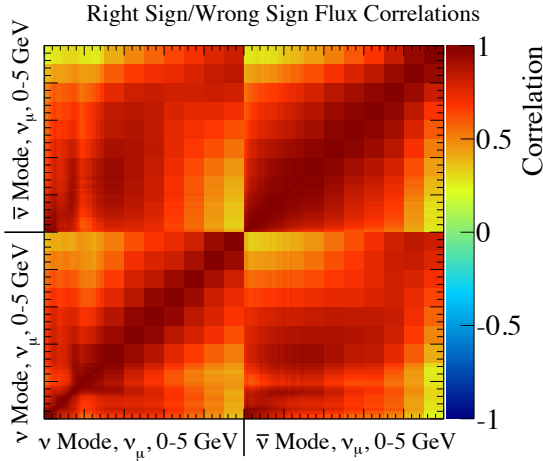


FIG. 36. The correlations between the flux normalization parameters for energy bins from 0 to 5 GeV for the neutrino mode and anti-neutrino mode  $\nu_\mu$  fluxes.

### K. Cross Section Measurements

A unique feature of NuPRISM is the ability to measure the true neutrino energy dependence of both CC and NC interactions using nearly monoenergetic beams. These measurements are expected to significantly enhance the reach of oscillation experiments, since the energy dependence of signal and background processes must be understood in order to place strong constraints on oscillation parameters. As explained in Section II F, additional multinucleon processes, with a different energy dependence than the currently modeled CCQE and CC1 $\pi$  cross sections can affect the T2K oscillation analysis. In the current disappearance analysis, there are also substantial uncertainties on NC1 $\pi^+$  and NC1 $\pi^0$  processes (for disappearance and appearance respectively). As a result, future proposed experiments which use water as a target (e.g. Hyper-Kamiokande and CHIPS) will directly benefit from the NuPRISM cross section program; other programs benefit less directly through a critical validation of our assumptions of the energy dependence of the cross section on oxygen. It is also not just long baseline oscillation programs which benefit, as cross section processes at T2K's flux peak are also relevant for proton decay searches and atmospheric neutrino oscillation analyses. Finally, should T2K run an antineutrino beam during NuPRISM operation, all arguments made above equally apply for antineutrino cross section measurements at NuPRISM.

One should also consider the study of neutrino interactions interesting in its own right as a particle/nuclear theory problem. As an example, MiniBooNE's cross section measurements have received much attention from the nuclear theory community who predominantly study electron scattering data.

Some of the difficulties in improving our understanding of neutrino cross sections stems from the fact that we do not know, for a given interaction, the incident neutrino energy. Any given measurement is always averaged over the entire flux. The observed rate  $N$  in a given observable bin  $k$  depends on the convolution of the cross section,  $\sigma$ , and the flux,  $\Phi$ :

$$N^k = \epsilon_k \int \sigma(E_\nu) \Phi(E_\nu) dE_\nu \quad (10)$$

where  $\epsilon$  is the efficiency. Therefore, our understanding of the energy dependence of neutrino interaction for a particular experiment is limited by the flux width and shape. One then attempts to use different neutrino fluxes (with different peak energies) to try to understand the cross section energy dependence. As discussed later in this section, for CC interactions we have many examples of disagreements between experiments, and for NC, we have a limited number of measurements made, and the lack of information and conflicting information leaves unresolved questions about the true energy dependence of the cross section.

In addition to providing new measurements on oxygen, there are two main advantages of NuPRISM over the current paradigm. First, we can directly infer the energy dependence of the cross section by combining measurements at different off-axis angles into a single measurement, as if we would have had a Gaussian neutrino flux source. Second, and equally important, we can fully understand the correlations between energy bins, in a way not possible previously when comparing across experiments with entirely different flux setups.

In CC interactions, previous experiments use the muon and hadronic system to try to infer the neutrino energy dependence. NuPRISM has the capability to directly test if the neutrino energy dependence inferred from the lepton information is consistent with the energy information determined from the off-axis angle. NuPRISM will also for the first time probe the energy dependence of NC cross sections within a single experiment.

Furthermore, there is no data for the kinematic information of pions out of NC $\pi^+$  interactions. However, NC $\pi^+$  is one of the backgrounds in the current T2K 1 $R_\mu$ -like selection used for the disappearance analysis. A direct measurement of NC $\pi^+$ , and a measurement of the pion momentum and angular distributions would reduce the substantial uncertainties on this process (in both cross section and detector efficiency) in the analysis.

Oxygen is an interesting target material for studying cross sections because few measurements exist and it is a medium sized nucleus where the cross section is calcu-

TABLE VI. Expected number of events in the fiducial volume of NuPRISM for  $4.5 \times 10^{20}$  POT, separated by true interaction mode in NEUT.

Int. mode	1-2°	2-3°	3-4°
CC inclusive	1105454	490035	210408
CCQE	505275	271299	128198
CC1 $\pi^+$	312997	111410	39942
CC1 $\pi^0$	66344	23399	8495
CC Coh	29258	12027	4857
NC 1 $\pi^0$	86741	32958	12304
NC 1 $\pi^+$	31796	11938	4588
NC Coh	18500	8353	3523

lable. NuPRISM will provide differential measurements in muon and final state pion kinematic bins. While these kinds of measurements will be done with the ND280 P0D and FGD2 detectors in the near term, NuPRISM will have more angular acceptance than those measurements and so enhances the T2K physics program.

Possible cross section measurements, based on observable final state topologies, at NuPRISM include:

- CC inclusive
- CC0 $\pi$
- CC1 $\pi^+, \pi^0$  (resonant and coherent)
- NC1 $\pi^+, \pi^0$  (resonant and coherent)
- NC1 $\gamma$

The above list is based on expected water Cherenkov detector capabilities from experience with MiniBooNE, K2K 1 kton and Super-Kamiokande (SK) analyses. All CC measurements can be done for  $\nu_\mu$  and  $\nu_e$  flavors due to the excellent e- $\mu$  separation at NuPRISM. Antineutrino cross section measurements are also possible with similar selections. A brief summary of each measurement follows. Table VI shows the number of events in the FV of NuPRISM, broken down by interaction mode.

### 1. CC Inclusive

Inclusive measurements are valuable because they are the most readily comparable to electron scattering measurements and theory, as there is minimal dependance on the hadronic final state. Also, external CC inclusive neutrino data was used in the estimation of the T2K neutrino oscillation analyses to help determine the CCDIS and CC multi- $\pi$  uncertainties.

The CC  $\nu_\mu$  cross section has been measured on carbon by the T2K [28] and SciBooNE [29] experiments. MINERvA has produced ratios of the CC inclusive cross section on different targets (C,Fe,Pb) to scintillator [30]. In addition, the SciBooNE results include the energy dependence of the CC inclusive cross section from the muon

kinematic information. The CC  $\nu_e$  cross section on carbon is in preparation by T2K.

NuPRISM should be able to select CC  $\nu_\mu$  and  $\nu_e$  events with high efficiency and produce a CC inclusive measurement vs. true neutrino energy on water. Using the latest T2K simulation tools, we estimate a CC inclusive  $\nu_\mu$  ( $\nu_e$ ) selection to be 93.7% (50.4%) efficient relative to FCfv and 95.9% (39.5%) pure based on observable final state. The low purity of the  $\nu_e$  selection is predominantly due to the small  $\nu_e$  flux relative to  $\nu_\mu$ .

### 2. CC0 $\pi$

The CCQE  $\nu_\mu$  cross section has been measured on carbon by MiniBooNE [31] and is consistent with a larger cross section than expected which could correspond to an increased value of an effective axial mass ( $M_A$ ) over expectation; SciBooNE's analysis was presented at NuInt2011 [32] but not published and is consistent with MiniBooNE. In addition, a measurement by NOMAD [33] was done at higher neutrino energies which is not in agreement with MiniBooNE and SciBooNE. This is shown in Figure 37, along with the recent T2K ND280 Tracker analysis results. An indirect measurement of the cross section was done with the K2K near detectors, where a higher than expected value of the QE axial mass,  $M_A$ , was also reported [35]. There are also recent results from MINERvA [34].

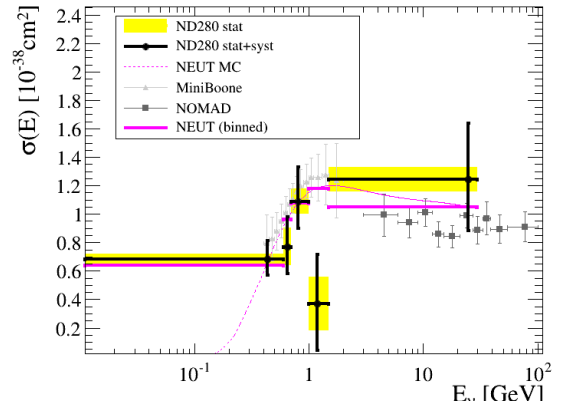


FIG. 37. The CCQE cross section as predicted by NEUT (pink dashed) vs. true neutrino energy. Also overlaid are results from MiniBooNE, NOMAD and T2K.

MiniBooNE's selection was CC0 $\pi$ , that is 1 muon and no pions in the final state, and was 77.0% pure and 26.6% efficient; the  $1R_\mu$ -like selection at SK is 91.7% pure and 93.2% efficient, based on observable final state. It is postulated that the MiniBooNE selection, but not the NOMAD one, is sensitive to multinucleon processes, where a neutrino interacts on a correlated pair of nucleons and that this resulted in the higher cross section reported

by MiniBooNE. However, the two experiments have very different flux, selection and background predictions and systematics.

By measuring the CC0 $\pi$  cross section at different vertex points in NuPRISM, we should be able to infer the different energy dependence and constrain multinucleon and CC1 $\pi^+$  pionless  $\Delta$  decay (PDD) processes. This can be seen in Figure 6, which shows the momentum of CCQE and MEC (Nieves' npnh) events for a particular angular range ( $0.85 < \cos(\theta) < 0.90$ ) generated according to the T2K flux, and for a 1 GeV NuPRISM flux. MiniBooNE and T2K have difficulty separating the MEC component of the CCQE cross section due to the shape of their neutrino energy spectra, but the NuPRISM detector would give us additional information to separate out that component and characterize it, as demonstrated in Figure 6. Even though NuPRISM is not a measurement on carbon, oxygen is of a similar density to carbon and so will be helpful in understanding the difference between the MiniBooNE and NOMAD results if it is indeed due to MEC.

### 3. CC1 $\pi^+$ and CC1 $\pi^0$

The CC1 $\pi^+$  and CC1 $\pi^0$  cross sections have been measured on carbon by MiniBooNE [36],[37]; K2K also produced measurements CC1 $\pi^+$  [38] and CC1 $\pi^0$  [39] with the SciBar detector. One may infer the coherent contribution to the CC1 $\pi$  cross section from the angular distribution of the pion; this was done by K2K [40] and SciBooNE. Improvements to the SK reconstruction could yield a similar efficiency and purity to the the MiniBooNE selections for CC1 $\pi^+$  (12.7%, 90.0%) and CC1 $\pi^0$  (6.4%, 57.0%) based on observable final state.

The CC1 $\pi$  resonant cross section for the T2K flux is dominated by contributions from the  $\Delta$  resonance [41], so NuPRISM would provide clear information about the N $\Delta$  coupling and form factors. We can also compare the pion momentum produced out of CC1 $\pi^+$  interactions for different neutrino energies in order to better understand how final state interactions affect pion kinematics.

### 4. NC1 $\pi^+$ and NC1 $\pi^0$

The NC1 $\pi^0$  cross section has been measured on carbon by MiniBooNE [42] (36% efficient, 73% pure) and SciBooNE. A measurement of the ratio of NC1 $\pi^0$  to the CCQE cross section has been done water by the K2K 1kton near detector [43]. The efficiency and purity of the K2K selection is 47% and 71% respectively. A measurement of NC $\pi^+$  exists [45] on a complicated target material ( $C_3H_8CF_3Br$ ) but has no differential kinematic information. Figure 38 shows this measurement with a prediction from the NUANCE neutrino event generator.

A measurement of NC $\pi^+$  will be challenging but possible at NuPRISM. T2K already has developed an “NC”

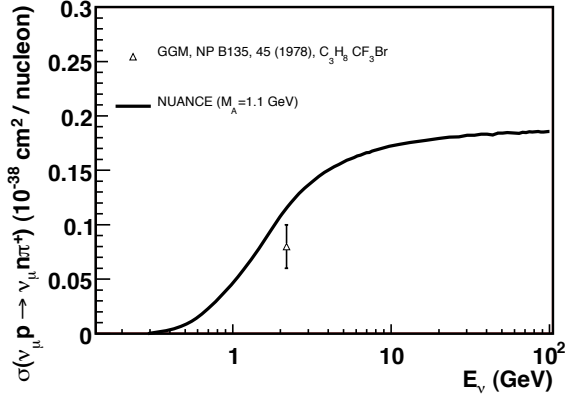


FIG. 38. The NC $\pi^+$  cross section as predicted by NUANCE vs. true neutrino energy overlaid with the only measurement (on  $C_3H_8CF_3Br$ ). Figure from Ref. [44]

enhanced selection for Super-K that is 24% NC $\pi^+$ , 14% NC1proton, and 55% CC $\nu_\mu$ , by interaction mode. Recent developments in event reconstruction at Super-K include a dedicated pion ring finder, which should make possible a more pure selection of NC $\pi^+$  from which the pion momentum and angular distribution can also be measured. Since NuPRISM will allow for a first measurement of the energy dependence of the NC channels and like the CC channels, it will be particularly interesting to measure the outgoing pion spectra of these events in order to probe nuclear final state interactions.

To summarize, NuPRISM’s measurement of true neutrino energy dependence of the cross section is a unique and potentially critical input to our overall understanding of cross section processes around 1 GeV neutrino energy. In particular, NuPRISM will help us understand for CC0 $\pi$  events, if the shape and size of the PDD and multinucleon components are modeled correctly. Furthermore, NuPRISM can provide new information on the pion kinematics out of NC interactions relevant to the oscillation analysis and the energy dependence of those cross sections.

### III. DETECTOR DESIGN AND HARDWARE

The NuPRISM detector uses the same water Cherenkov detection technology as Super-K with a cylindrical water volume that is taller than Super-K (50-100m vs 41m) but with a much smaller diameter (6-10m vs 39m). The key requirements are that the detector span the necessary off-axis range ( $1^\circ$ - $4^\circ$ ) and that the diameter is large enough to contain the maximum required muon momentum. The baseline design considers a detector location that is 1 km downstream of the neutrino interaction target with a maximum contained muon momentum of 1 GeV/c. This corresponds to a 50 m tall tank with a 6 m diameter inner detector (ID) and a 10 m diameter outer detector (OD), as shown in Figure 39. A larger, 8 m ID is also being considered at the expense of some OD volume in the downstream portion of the tank. As the NuPRISM analysis studies mature, the exact detector dimensions will be refined to ensure sufficient muon momentum,  $\nu_e$  statistics and purity, etc.



FIG. 39. The planned configuration of the nuPRISM detector within the water tank is shown. The instrumented portion of the tank moves vertically to sample different off-axis angle regions.

The instrumented portion of the tank is a subset of the full height of the water volume, currently assumed to be 10 m for the ID and 14 m for the OD. The novel feature of this detector is the ability to raise and lower the instrumented section of the tank in order to span the full off-axis range in 6 steps. The inner detector will be

instrumented with either 5-inch or 8-inch PMTs to ensure sufficient measurement granularity for the shorter light propagation distances relative to Super-K. Also under consideration is to replace the OD reflectors with large SMRD-style scintillator panels, as discussed in Section III E.

The remainder of this section describes the elements needed for NuPRISM and corresponding cost estimates, where available. The cost drivers for the experiment are the civil construction and the cost of the PMTs, and, correspondingly, more detailed cost information is presented in those sections.

#### A. Site Selection

The NuPRISM detector location is determined by several factors, such as signal statistics, accidental pile-up rates, cost of digging the pit, and potential sites available. At  $2.5^\circ$  off-axis position at 1 km with a fiducial volume size of 4 m diameter and 8 m high cylinder, the neutrino event rate at NuPRISM is more than 300 times that of SK. At 2km, the number of events drops by a factor of 4, which yields 75 times more events than SK, for the same size of the detector. The impact of the number of events collected on the physics sensitivities is described in Section II. The event pile-up is dominated by sand muons, but at 1 km, the pile-up rate appears to be acceptable, which is explained in more detail in Section II. The detector size and the depth scales with the distance to the NuPRISM detector. In order to cover from  $1$ - $4^\circ$  off-axis angles, the depth of the detector is 50m at 1km and 100m at 2km. There are standard Caisson approach available the pit depth of up to 65m and diameter of up to 12m. For deeper depth or larger diameter, more specialized construction may be required, and could increase the cost per cubic meter of excavation dramatically.

The two far detector sites that must be considered are the Mozumi mine, where Super-K is located, and Tochibora, which is a candidate site for Hyper-K. There are four potential unused sites in the Tochibora and Mozumi directions, not including rice fields, as shown in Figure 40:

- 750m site near the Muramatsu community meeting centre: This location is right next to R245 and owned by the local government. The space is limited but covers the Mozumi direction and the central line between Mozumi and Tochibora. This site would have the highest event pile-up rate.
- 1km site: a large un-cultivated private land covering both Tochibora and Mozumi directions
- 1.2km site: a large patch of private land at the foot of a forest covering both Tochibora and Mozumi directions
- 1.8km site: the originally considered 2km detector site owned by the local government covering Tochi-



FIG. 40. Potential sites are shown for NuPRISM if all rice field locations are excluded.

bora direction. This site would have the deepest detector, 90m deep.

If the rice field can be available, there are a lot more choices. At the time of the 2km detector site study, rice fields were also considered, although not selected in the end. Changing the land use for the rice field would require additional approval process, if it were possible. The process of land use require consensus from the local community and the strong involvement of the host institution. There are facilities that are operated just outside J-PARC, the KEK-Tokai dormitory, KEK Tokai #1 building at IQBRC, and the dormitory of the Material Science Institute of Tokyo university about hundred meter north of IQBRC.

### B. Civil Construction

Based on the current baseline design of the NuPRISM detector described previous sections, we have communicated with companies for the preliminary cost estimation of NuPRISM civil construction; the water tank construction and detector construction. The NuPRISM detector is also considered as a prototype detector of Hyper-Kamiokande (Hyper-K) for testing new photo-sensors, readout electronics, and the water containment system design.

Two groups have been contacted to provide preliminary cost estimates for the civil construction associated with fabricating a 50 m deep cylindrical volume with a 10 m diameter. The first group consists of a general construction company and a heavy industrial company currently providing cost estimates for Hyper-K. The second group is a single general construction company that was associated with the cost estimates from the original T2K 2 km detector proposal [47].

There are several techniques to construct the  $10 \text{ m} \phi$  and 50 m long vertical “tunnel”; Pneumatic Caisson (PC) method, Soil Mixing Wall (SMW) method, New Austrian Tunneling (NAT) method, Urban Ring (UR) method.

Each of the construction methods have pros and cons, and some of the methods are not applicable depending on the actual geological condition. Cost estimates from both construction groups are given in the appendix.

### C. Liner and Tank

The NuPRISM detector can be used for proof-testing various designs and components which will be adopted in the Hyper-K detector. The NuPRISM water tank will have the same liner structure as that designed for Hyper-K.

The structure of the NuPRISM tank liner is shown in Figure 41. The innermost layer contacting with the tank water must be a water-proofing component to seal the water within the tank. We use High-Density Polyethylene (HDPE) sheets, which are commonly used as a water-proofing tank liner material. The sheets have extremely low water permeability and also are resistant to long-term damages from the ultra pure water. The adjoining sheets are heat-welded, and the welded part also keeps the water-proof functionality.

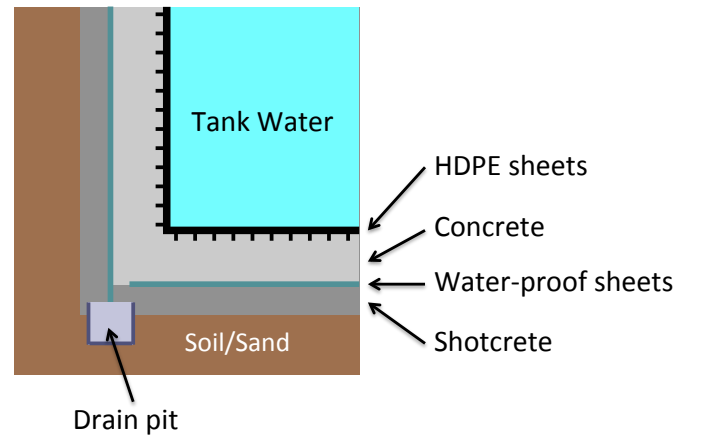


FIG. 41. A schematic view of the NuPRISM tank liner.

We select the HDPE sheet with a number of studs protruding from one side. These studs work for anchoring the sheet firmly on the backside concrete layer. To build this "HDPE on concrete" liner, a HDPE sheet is fastened to the inside of a concrete form beforehand, then the concrete is poured into the form for making the backfill concrete layer. While the thickness of the HDPE liner is 5-10mm, the thickness of the backfill concrete layer is yet to be determined.

Though we aim to construct the HDPE sheet liner such that the tank water can not leak, an additional waterproof layer is made between the backfill concrete layer and the shotcrete. This layer works as a catcher and a guide for the water by the unexpected leakage through the HDPE liner (and also the sump water through the shotcrete). This leaked water is drained via pits placed under the water tank.

#### D. Detector Frame and Lifting Mechanism

This section describes a proposed design for the frame that supports the NuPRISM PMTs and defines both the inner and outer detector. We will also describe the system by which this frame can be moved up and down in order to be able to make the NuPRISM measurements. Attention will be paid to the question of providing adequate water flow through the NuPRISM frame while maintaining optical separation.

##### 1. Detector Shape, Support and Positioning

Figure 42 shows a simple cylindrical design, the walls of the Inner Detector (ID) being 0.5 meters thick. The half circles represent the 20" PMTs (0.5m) facing outward for the veto region (OD). The smaller half circles represent 8" PMTs (0.2m) facing inwards to the ID region. The 0.5m thickness of the detector wall is to contain the bodies of the PMTs (and PMT electronics) and, with internal stiffening braces, be stiff enough to accurately position the PMTs and not deform significantly under the weights and buoyancies.

Figure 42 also shows a conceptual support and positioning system. The detector is positioned on four vertical rails fixed to the shaft walls, and supported on top and bottom rings. Struts connect the detector to these two rings. The struts are positioned at the corners of the detector where the structure is strongest, and angled so that the distance from the detector to the start of the reflector is 1.7m top and bottom, and 1.5m on the sides. The reflector encloses the OD region and is required to be optically isolated from the ID volume, and from the shaft water volumes above and below. We discuss the reflector in more detail below.

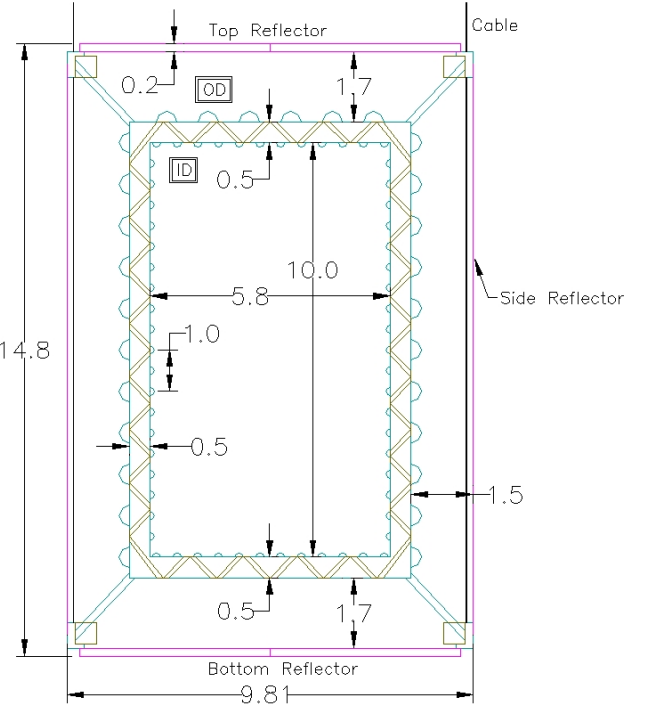


FIG. 42. The Detector is positioned on four rails inside shaft, and supported on top and bottom rings. Struts connect the detector to its rings. Four vertical cables support the assembly. Ballast can be added to the rings, if required. Distances are in meters.

##### 2. Water Flow and Optical Isolations

Figure 43 shows views of the top-left corner of the detector and reflector. Two section views indicate the conceptual features and functions involved. The volume of the ID and OD are  $\approx 264\text{m}^3$  and  $\approx 790\text{m}^3$ , respectively, with a combined volume of  $\approx 1,190\text{m}^3$  (including all wall volumes). If the apparatus is to traverse the shaft limits in  $\approx 24$  hours, the speed would be  $\approx 1.5$  meters/hour. Since the reflector side walls are close to the shaft, the displaced water needs to flow through the reflectors. This speed corresponds to a water flow of  $\approx 118 \text{ m}^3/\text{hour} = 2.0 \text{ m}^3/\text{min}$ . Even if the water could flow past the sides of the reflector enclosure, 1,190 tons of water would also be in motion, which would be difficult to accommodate. With no water flowing through the sides of the reflector enclosure, the sides can be simple metal panels with a white inner surface to enhance the OD light collection. As indicated in Figure 43, these vertical reflector walls need to notch around the four rails and the associated couplings on the rings, and would be screwed to the top/bottom rings. With a height of 13.8m and circumference of 33.5m, it will need to be segmented with overlapping joints (or added joint strips). When the detector is out of the water, it would be useful to be able to easily remove the side reflector segments. Minimal segmentation would be four, with joints at the center of the

'notches'. This would allow the segments to slide out past the rails and the support towers. The top and bottom reflectors are also bolted to the top/bottom rings, but they have to be thicker to allow them to be strong and stiff due to the quantity of water flowing through them. The stiffness is achieved by making the top/bottom reflectors 0.2m thick and them having an internal bracing structure. The top/bottom reflectors need an optical seal to the rest of the shaft, yet allow  $\approx 2.0$  tons/min of water to flow through. Figure 43, shows two possible solutions:

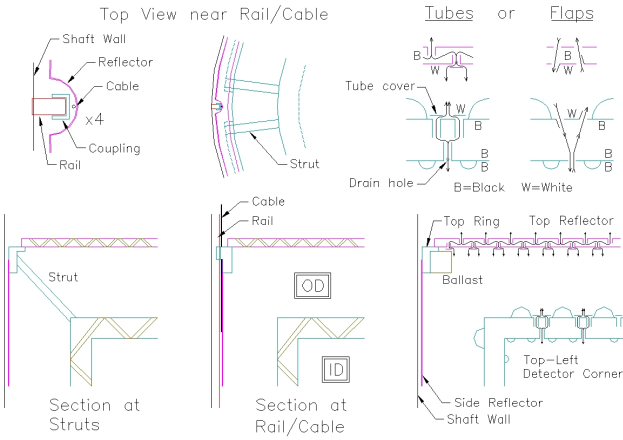


FIG. 43. This shows views of the top-left corner of the detector and reflector. Two sections views indicate the conceptual features and functions involved. A system of offset black pipes (or flaps) would allow water to flow through.

1. The first is a system of offset black pipes, so that water can flow through, but any light would need at least two reflections off black surfaces. The inner surface of the top/bottom reflectors would be white to enhance light collection. The tubes at the inner surface would have white 'tube covers'. This is easily done by having the tube extend, with the tube cover fixed to it, but the tube having four side large slots, leaving webs of material to hold the cover. The cover and outer surface of tube extension would be white. To prevent water being trapped in the reflector wall when the detector is lifted out of the water, there would be 'Drain holes' in the tubes, just inside the inner wall. Alternately, there could be some small drain tubes+covers extending slightly into OD volume. This scheme is a little complicated, but has the advantage of no moving parts. If the flow is fully distributed over the  $55.0 \text{ m}^2$  area, the movement water flow would then be  $\approx 36$  liters/minute/ $\text{m}^2$ .
2. Another way solve this problem would to have a system of flaps that open only when the detector is moved, and close automatically when it stops. Half the flaps open when the detector moves down

(water moves up), these flaps close under their own weight when movement stops. The other flaps open when the detector moves up (water down), these 'down' flaps would need to be spring loaded or counterweighted to close when movement stops. In Figure 43, we show both these flaps in the open position. The inner surfaces of the flaps would be white. In this scheme most of the water would drain through the spring loaded 'down flaps', but would also require a system to small holes or pipes to drain out the last of the water. This system has many moving parts that cannot be lubricated, so binding and galling would be concerns, but it can probably be made to work. It would need to be made very reliable, a few flaps stuck closed wouldn't be a concern, but some stuck open could be a problem. This system has the disadvantage that it prevents lower levels of circulating water during data taking. This recirculating loop will probably be required for; the purification and temperature control of the water, cooling of electronics etc. For these reasons, we prefer the offset tubes option.

When the detector is out of the water, the bottom reflector would need to be segmented to be removed between the support towers. With four towers (see Figure 44), the four bottom cover segments would be  $4.6 \times 4.6$  meters. Higher segmentation (multiples of 4) would also be possible. We imagine a scissor cart rolled under the detector, lifted to contact a segment. It could then be unbolted, lowered and rolled away. The segments would need to overlap on the inner surface for light seal, and on the outer surface for joining (or have extra joint strips). The top reflector would be craned out, in one piece or in segments.

### 3. Walls of Inner Detector (ID)

The top/bottom walls of the ID would also need to allow water flow, otherwise one would have to allow for the inertia of 400 tons of trapped water. The movement flows would be 42 tons/hour = 0.7 tons/minute. Distributed, this is 27 liters/minute/ $\text{m}^2$ . This is somewhat less than the 36 liters/minute/ $\text{m}^2$  of the reflector, but this wall has all the PMTs as well. In Figure 43, I show the tubes and flaps options for this wall, similar to that for the top and bottom reflectors.

### 4. Detector in the shaft

The detector is guided within the shaft by a set of rails. The current proposal has four rails and support cables but it could be three, five, etc. if dictated by other design considerations. It is important to understand that the ring connections to the rails do not need to be high precision rail bearings. Because the positioning accuracy

required is only  $\approx 1\text{cm}$ , they could be simple guides (see Figure 44). Similarly, the rails do not need to be complex. The loose tolerance makes it far less likely that the detector will jam on the rails. When the detector has been moved, there may be a system to lock two of the four guide locations to eliminate small position changes during data taking. Another reason for a looser coupling (before locking), is that then the rails do not need to be so precisely positioned on the shaft walls, i.e. several millimeters versus  $0.1\text{mm}$ .

Figure 44 shows the detector in the shaft, the shaft covers and the external towers. Four vertical cables support the assembly. Ballast can be added to the rings, if required. Above ground, there would be four towers extending upwards 17.6 meters. Four motors, acting together, lift or lower the detector in the shaft, or even lift it completely out of the water. The load will increase as it leaves the water (loss of buoyancy), if the load is too much, the top ballast can be removed by crane as it clears the water. Or, a lifting frame could be attached when the top ring clears the water, allowing the crane to raise it further, then it can be locked in the out position, freeing the crane.

In this concept, the signal and power cables for the detector would travel up out of the water beside the four support cables. They would nominally go up and over the towers, then down to the ground racks. With this scheme there would be no extra length in the water, wherever the detector was positioned in the shaft. When the detector is slowly lowered further down the shaft, the cables etc. should be cleaned before entering the water.

Once the detector is entirely out of the water, the shaft covers can be craned back into position (see Figure 45). Adding counterweights will make sure the Center-of-Gravity (COG) of the covers are beyond the detector shadow when the covers are pushed in. The covers would be bolted to the ground. Lightweight seals cover the joints, the central region, and the four small areas where the support cables, signal and power cables exit the water.

Figure 46 shows the detector out of the water and covers reinstalled. It is important that the covers and seals are safe for people and light equipment, so that the bottom of the detector can be worked on. Scaffolding can be erected to work on all parts of the detector. The figure also shows the detector moved to a stand. To move the detector, the lifting frame would be installed, the detector supported, then the eight ring guides removed and two of the towers removed (or laid down), opening a path for the detector move.

Whether above the shaft or on a separate stand, it would probably be useful to be able to remove the reflector sections and get access to parts of the ID. If the ID were bolted together sections, it might be possible to partially disassemble to make repairs and/or replacements.

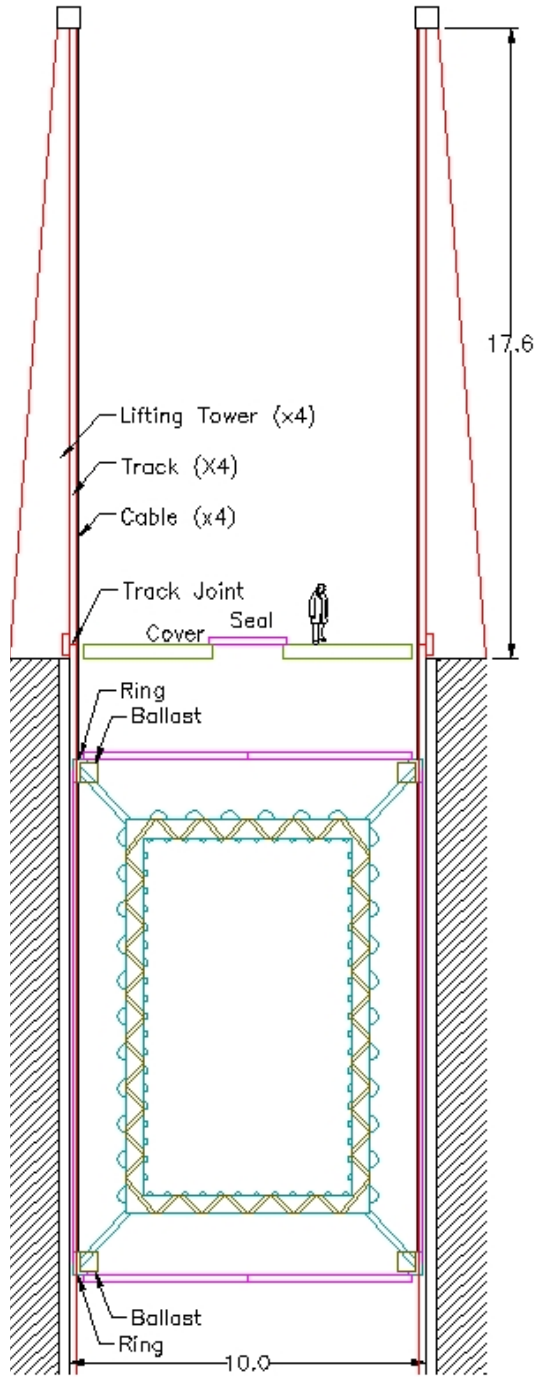


FIG. 44. This shows the detector in the shaft, the shaft covers and the external towers. Four vertical cables support the assembly. Above ground, there would be four towers upwards extending 17.6 meters. Four motors, acting together, lift or lower the detector in the shaft, or even lift it completely out of the water.

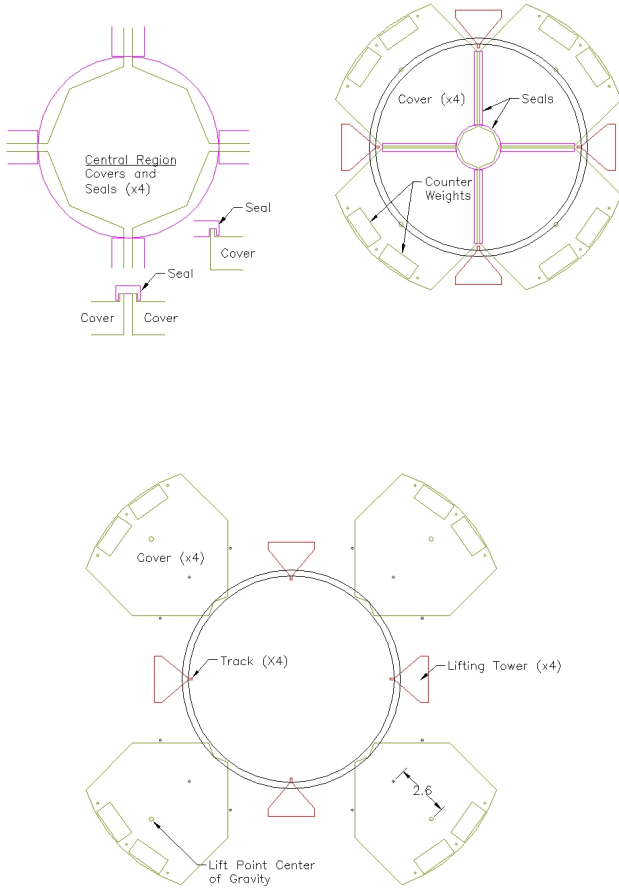


FIG. 45. The four covers can be craned in and out. Added counterweights make sure the center of gravity is beyond the detector shadow when in. The covers are bolted to the ground. Light weight seals cover the joints and the central region.

### 5. Detector Surveying

As mentioned earlier, after the detector has been moved, there may be a system to lock two of the four guide locations to eliminate small position changes during data taking. A laser surveying system could be in place to look down through the water to periodically check the detector position at the four rail locations. The PMTs may have to be turned off during these times. The positioning of PMTs within the detector would be surveyed during its assembly (out of water) and then should only be subject to thermal expansion/contraction shifts in the water, plus deflections due to loads (primarily the top/bottom PMTs).

The thermal expansion/contractions of the detector will depend on its material. For a 10 meter Aluminum

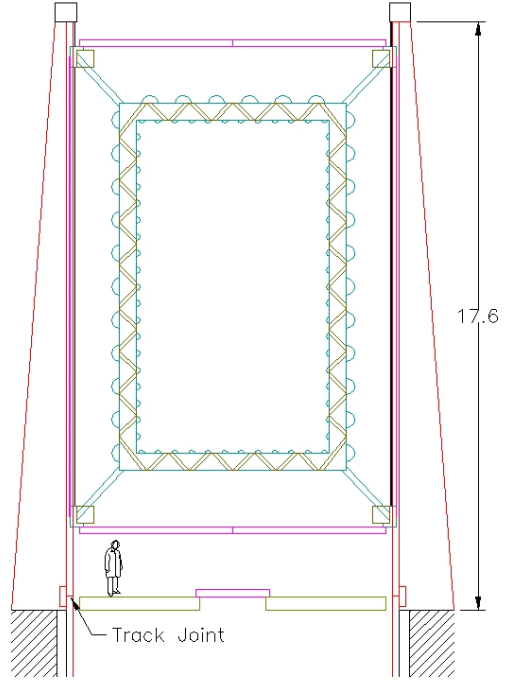


FIG. 46. The four towers allow the detector to be raised out of the water (units in meters). The covers can be reinstalled under the detector, allowing people to work underneath it. A lifting frame can be craned over the detector, attached, and the towers removed. The detector can then be craned to a stand.

piece, the expansion would be 2.2mm for a 10 OC change. 306 stainless steel would be 1.6mm. The shaft, being reinforced concrete, should expand 1.3mm for 10 degrees. Stainless steel is a better thermal match, the differential expansion being 0.3mm for 10 degrees, compared to 0.9mm for an Aluminum detector frame, but the difference is not likely to be significant.

### E. Scintillator panels

The veto system of the NuPRISM detector can be composed of plastic scintillator detectors which completely surround the the water Cherenkov detector. The main purpose of the veto system is to identify backgrounds from beam neutrino interactions in the surrounding pit walls and to provide a cosmic trigger signal for calibration purposes. The technology developed for the ND280 SMRD detector can be applied for this veto system.

### 1. Scintillator counters with WLS/avalanche photodiode readout

Scintillator counters with wavelength-shifting (WLS) fibers and opto-electronic readout are an established technology for neutrino detectors in long-baseline neutrino oscillation experiments. ND280 consists of several subdetectors which use extruded plastic scintillators of various shape and dimensions [11]. Each of these subdetectors is comprised of plastic slabs and bars, wavelength shifting fibers and compact photosensors - multi-pixel avalanche photodiodes. The Kuraray double-clad Y11 WLS fibers are used in all ND280 scintillator detectors for transportation of the reemitted light to photosensors.

*SMRD counter.* The SMRD detector was made of the polystyrene-based scintillator slabs, each with an embedded wave-length shifting fiber. The slabs were produced at the Uniplast Factory (Vladimir, Russia). The scintillator composition is a polystyrene doped with 1.5% of paraterphenyl (PTP) and 0.01% of POPOP. The slabs were covered by a chemical reflector by etching the scintillator surface in a chemical agent that results in the formation of a white micropore deposit over a polystyrene[19]. The chemical coating is an excellent reflector, besides it dissolves rough surface acquired during the cutting process. The WLS fiber was read out on both ends to increase light yield, improve uniformity and position accuracy, and provide redundancy.

A key feature of these counters is the usage of the one serpentine-shaped WLS fiber for readout of scintillating signal. The serpentine geometry of a groove consists of 15 half-circles, each with a diameter of 58 mm and straight sections connecting the semi-circles. A 1 mm diameter Y11 (150) Kuraray WLS fibers of flexible S-type and with double-cladding was used for the SMRD counters. Fibers are bent into a serpentine-shape and glued into grooves with BC600 Bicron glue. The mean light yield for sum of both ends was about 40 p.e./MIP after subtraction of the MPPC cross-talk and after pulses. The high light yield allowed us to obtain the efficiency of more than 99.9% for detection of minimum ionizing particles.

The light yield of about 14 p.e. per a minimum ionizing particle ( $\sim 7$  p.e./MeV for 1 cm thick bar) provides the efficiency for detection of minimum ionizing particles of more than 99% in an individual scintillator bar for a detection threshold of 1.5 p.e. Time resolution depends on the light yield as  $\sim 1/\sqrt{N_{p.e.}}$  where  $N_{p.e.}$  – is the number of photoelectrons. For the l.y. of 20 p.e. the typical resolution is obtained to be  $\sigma$  1 ns. Detectors with shorter WLS fibers were also tested. Light yield of the detector with a 5 m long WLS Y11 fiber is shown in Fig. 47

In this case, the minimum light yield of more than 40 p.e./MIP (sum of both ends) is obtained.

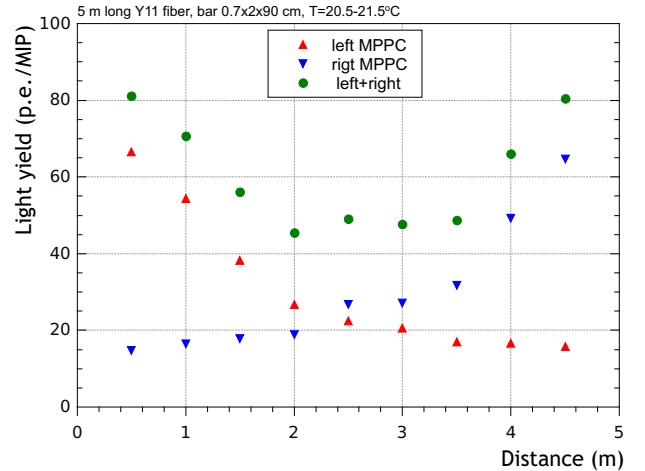


FIG. 47. Light yield of a scintillator counter with 5 m long WLS fiber vs position along the fiber. The T2K 667 pixel MPPC's were used in this measurement.

### 2. Veto counters for NuPRISM

i

The excellent performance of the SMRD counters with one serpentine WLS fiber per counter gives a possibility to make a veto system using similar approach. One option is to construct the NuPRISM veto system from scintillator counters, each of  $0.2 \text{ m}^2$ . One WLS Y11 S-type fiber is embedded in the extruded plastic slab of  $2000 \times 200 \times 7\text{mm}^3$ . Half-circles have the radius of 3 cm that allows to keep the performance of the fiber without loosing the transmission of the reemitted light along the fiber. A 6 m long Y11 fiber is readout on both ends by MPPC's. Taking into account the improved parameters of new MPPC's, for example, higher PDE, we can expect to obtain minimum light yield of 20-30 p.e./MIP and time resolution of about 1 ns for these detectors. More accurate information can be obtained after tests of the counter prototypes.

### 3. Integrated Design

Initial conceptual drawings of the fully integrated detector are shown in Figure 48. The structure is composed of stainless steel-coated I-beams that define both the inner and outer detector. The scintillator panels are shown covering a portion of the outer detector. The inner detector PMTs have been attached to the frame using stainless steel rods, and the optical separation between the inner and outer detectors is achieved using anodized aluminum plates. Once the experiment is approved, these drawings are intended to help guide the development of a complete set of engineering drawings for the detector.

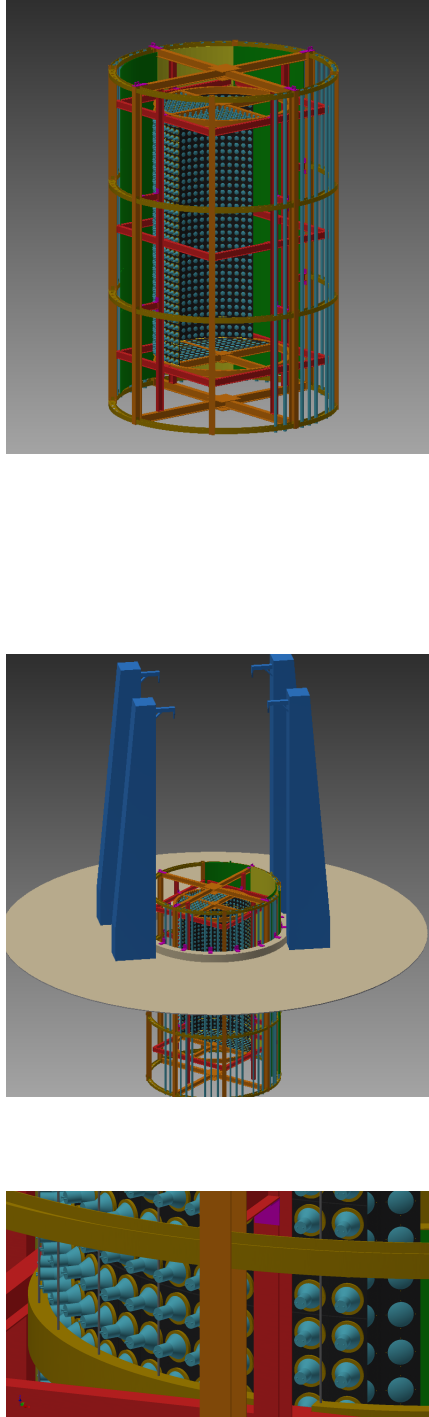


FIG. 48. A conceptual drawing of the fully integrated NuPRISM detector is shown (top), as well as the lifting towers (middle) and a detailed view of the beams supporting the inner detector PMTs (bottom).

## F. Photomultiplier Tubes

The original T2K 2 km detector proposal used 8" PMTs to better match the granularity of the 20" PMTs used in the much-larger Super-K detector. The baseline design for the NuPRISM detector is only 6 m in diameter and 10 m tall, which corresponds to 3,120 PMTs for 40% photocathode coverage. This is significantly smaller than the 11,129 PMTs used at Super-K, so to improve the granularity of the detector, 5" PMTs are also being investigated, of which 7,385 PMTs would be required for 40% coverage. Additional options such as avalanche photodiodes and high quantum efficiency coating are also being explored. Initial cost estimates from Hamamatsu for a wide variety of PMT configurations are given in the appendix.

## G. Electronics

Part of the goal of the NuPRISM is to serve as a prototype for the Hyper-K. We therefore want NuPRISM to use a set of electronics that is as close as possible to the electronics being proposed for Hyper-K. Some of the key features of the Hyper-K electronics are the following:

- Front-end electronics will be placed in the water, as close as possible to the PMTs.
- Front-end electronics are expected to find all hits above 0.25 PE and send all information about hits up to back-end electronics. In back-end computers trigger decisions will be made using software. No global triggers will be propagated to the front-end electronics.
- PMT digitization should provide 0.05 PE charge resolution, 0.5 ns timing resolution for 1 PE hits and 1250 PE dynamic range.

We shall note various aspects of the NuPRISM electronics where we may differ from the default HK electronics plan. In particular, one clearly different aspect of NuPRISM will be the much higher rate of ‘pile-up’ events during beam spills. The rate of sand muon events entering the ID may be as high as 0.19 per bunch. At minimum we therefore need electronics that can cleanly distinguish between PMT hits in different bunches; ie, hits with separation of order  $\approx 600\text{ns}$ . We may also want to have some capacity to distinguish between hits within a single bunch; ie hits that differ by 10s of ns. This is a more challenging requirement.

### 1. FADC Digitization

Given this requirement for inter-bunch and intra-bunch hit resolution we propose using FADC (Flash Analog to Digital Converter) digitization with basic digital

signal processing in the front-end electronics. The basic scheme is as follows:

1. The stretched/shaped PMT signal is fed into the FADC. Use of a standard commercial FADC is foreseen, with sampling frequency between 80-250 MHz and 12-14 bit resolution.
2. The digital output of the FADC is fed into an FPGA (on the front-end electronics card), where we do basic digital pulse processing (on the fly, at same rate as original digitization). Digital pulse processing would involve the following:
  - (a) Digital filtering to improve signal-to-noise ratio and to remove unwanted signal component (for instance from pickup of electromagnetic interference).
  - (b) Finding PMT hits.
  - (c) Calculating the pulse time and charge.
3. The digital pulse information is then transferred to the back-end electronics. We send different types of data depending on the pulse charge.

It is worth emphasizing that the expected timing resolution using FADCs is not intrinsically limited by the sampling rate. For instance, if you appropriately shape a PMT pulse, you can easily achieve better than 0.5 ns timing resolution using a 100 MHz digitizer (i.e. a sample each 10 ns), as long as you have decent signal to noise ratio, reasonable ADC accuracy (i.e. number of bits) and if you apply correct signal processing algorithms. Therefore, several studies were made in order to estimate impact of noise introduced by electronics and various signal processing algorithms on the overall system performance, so that one can configure the system in an optimum way. In our case an ‘optimum system’ means that error contributions from the acquisition chain would be small compared to errors due to statistics of the observed processes and those introduced by photomultipliers. We present a description of these studies in Sections III G 3, III G 4 and III G 5.

## *2. Signal Conditioning And PMT HV Supply*

We propose to use differential transmission in order to deliver signals from the PMT bases to the digitization board. An advantage of such a solution is that, in principle, it would allow us to use a standard unshielded twisted pair cable, while still maintaining fairly good immunity to pickup of electromagnetic interference. The base of the PMT would contain shaping circuitry, which would stretch PMT signals, limiting their bandwidth to match FADC requirements and converting them into a symmetric form, suitable for transmission via a twisted pair cable. Preliminary studies show that signal shaping using a 4-th or 5-th order Bessel-type low pass filter should provide satisfactory results.

One of the design goals for the NuPRISM is minimization of the amount of necessary cables. As such, it would be advisable to use a single cable to provide both high voltage to the PMT and to transmit the signal from the PMT base to the digitization board. Therefore, the preferable solution would be to synthesize the high voltage directly on the PMT base, from a 48-200 V DC supply, using either a commercial high voltage module or a custom designed voltage multiplier structure. This way, power to the PMT base could be delivered via an additional twisted pair of the same cable that would be used to transmit the shaped PMT signal. The slow control link necessary to tune the high voltage for specific PMT could be realized via a DC power line, thus avoiding the need to use additional cables. In any case, it should be emphasized that the details of the PMT HV implementation will depend strongly on the exact PMTs that are chosen.

## *3. Study of a Digital Constant Fraction Algorithm*

One of the frequently used algorithms for timing arrival of digitized pulses is the digital constant fraction algorithm. It works in a similar way to its analog counterpart (see Fig. 49), i.e.:

1. The pedestal is estimated using samples preceding the pulse and then it is subtracted from the original signal, thus removing the DC component.
2. An additional signal is created by delaying, inverting and optionally amplifying the original signal. If sub-sample delays are desired, then some form of interpolation is necessary.
3. A composite signal is created by summing the original and the delayed signals.
4. The sample number corresponding to the intersection point of the composite signal and the zero-level is calculated. Linear interpolation is used in order to get a sub-sample position.

An advantage of this algorithm is that, first of all, it is simple. Second, if one is able to avoid sub-sample delays and use gain factor that is a power of two, then the time of pulse arrival can be obtained using little memory and few simple operations – sign inversion, bit-shifting (multiplication by a power of 2), one addition per sample and one sub-sample interpolation, all of which are relatively little demanding on FPGA resources. Even if one uses FFT interpolation to increase sample density in order to reduce errors due to random time offset between the leading edge of the pulse and the phase of the sampling clock, the algorithm is still an attractive option in terms of overall resource usage. On the disadvantage side one should mention the algorithm is potentially unsuitable in case of noisy environments and weak signals, due to following factors:

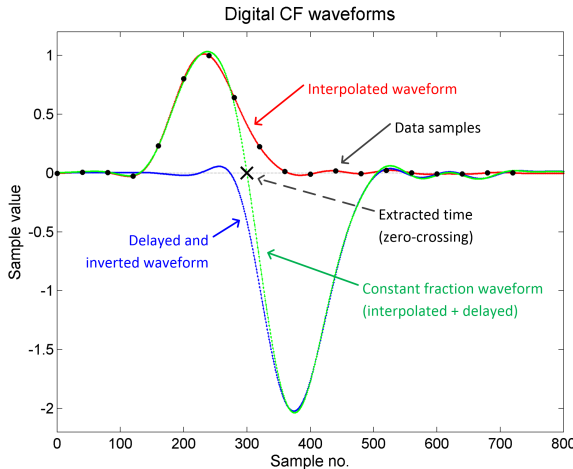


FIG. 49. Algorithm of a digital constant fraction discriminator. Sample indexes are for interpolated waveform (red curve has sample density increased by 40 times).

- the ‘zero’ level is obtained by subtracting the pedestal estimate from the signal, and this estimate may significantly differ from the real value if noise level is high;
- if the signal to noise ratio is poor, the signal samples will be significantly distorted.

Since only two samples are used to calculate the time of the ‘zero-crossing’ point, the method is prone to potentially significant errors.

Therefore, a Monte-Carlo study has been performed in order to test the limits of applicability of the digital constant fraction algorithm to signal to noise ratio and the shape of the signal. Since at present stage the major concern is defining performance requirements for the electronics, it was decided to take a general approach and make simulation at a signal layer only, disregarding detailed models of electronic circuits. The main idea was to test various combinations of sampling rate, signal to noise ratio and order of the shaping filter. Also, we wanted the results to be applicable to any system, independently of the particular ADC type (i.e. its sampling frequency and the number of bits). For this reason, the following choices were made:

- All the resulting time resolutions were normalized to the pulse rise time.
- The rise time is expressed as the number of samples at the rising edge, defined as a transition from 10% to 90% of the amplitude.
- The shaper circuit has been model using a normalized, ideal Bessel-type low-pass filter.

The simulations were performed in the MATLAB environment. The algorithm of the simulations was as follows (see Fig. 50):

1. An impulse response of an ideal, normalized Bessel-type low pass filter of a given order was calculated.
2. The calculated response was sampled at a frequency giving desired number of samples at the rising edge of the pulse. No quantization was made (i.e. ADC with infinite number of bits was assumed). The sampling process started at a random sub-sample offset  $t_{offset}$ , where  $t_{offset} \in [0, t_{sample})$  and had a uniform distribution;  $t_{sample}$  was the sampling period. This operation accounted for the fact that the phase of the sampling clock was not correlated with the time of pulse arrival.
3. White noise was added to the sampled signal. This step accounted for the electronics noise as well as errors introduced by the quantization process (ADC SNR =  $6.02N + 1.76\text{dB}$ , N being the number of bits). Therefore, the finite number of the ADC bits was ‘hidden’ in the amount of noise added to the signal.
4. The time of pulse arrival was calculated using the digital constant fraction algorithm described above. In order to make the results comparable, FFT interpolation was used so that the constant-fraction algorithm operated on a waveform with 64 samples at the leading edge of the shaper pulse, irrespective of the actual sampling frequency used.
5. The resulting sample number is increased by the initial sub-sample offset  $t_{offset}$  and then recorded. Afterwards, the procedure is reiterated starting from point 2, up until reaching required number of iterations.
6. The standard deviation of the achieved distribution of sample indexes is calculated and then normalized by the number of samples at the rising edge.

For every combination of filter order, signal to noise ratio and pulse rise time, the algorithm tested several constant fraction delays and chose the one corresponding to the best timing resolution.

Example results are shown in Fig 51. As expected, the most important factor affecting the timing performance was the signal to noise ratio. What did come out little surprising was a relatively low impact of the sampling rate with respect to the rise time of the shaper pulse. For higher signal to noise ratios (SNR) it seems that 1.4 to 1.6 samples at the rising edge is enough to get time resolutions of better than 1% of the rise time. For poor SNR increasing sampling density has little effect on timing performance of the algorithm. The above is a significant hint as to which way to go further – while a faster system means shorter rise times, it also means wider bandwidth and hence worse signal to noise ratios. As such, it may be worth to analyze the interrelationship between the sampling rate and signal to noise ratio to see whether an optimum can be reached at some point.

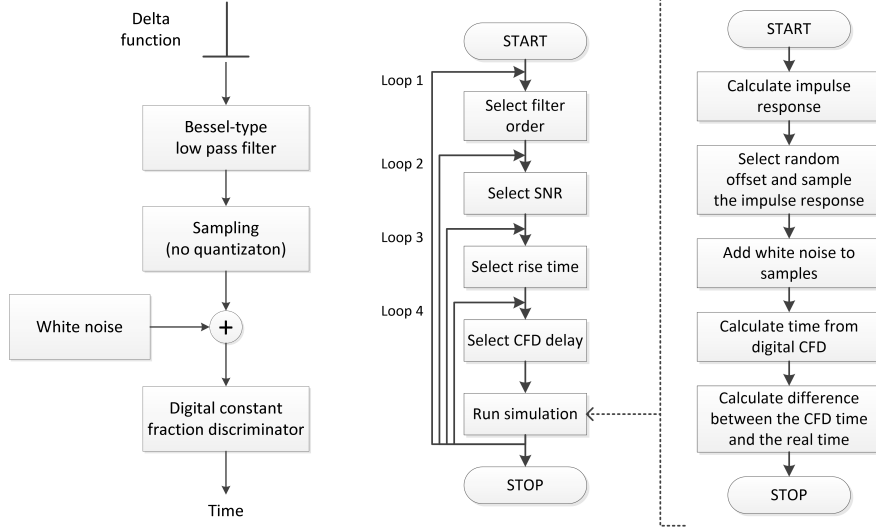


FIG. 50. Simulation setup (left) and algorithm (right) for studying the timing accuracy achievable when using the digital constant fraction algorithm, under various combinations of the order of the shaper (Bessel-type low-pass filter), sampling rate of the ADC and signal-to-noise ratio.

It may well be that the desired timing resolution can be achieved using a slower system just because the SNR will be improved. Nevertheless, the most important conclusion is that with a digital constant fraction approach it may be rather difficult to achieve desired timing resolution, given the dynamic range requirement. One needs to find signal processing methods which are better suited for low SNR scenarios.

When it comes to the order of the Bessel-type shaping filter, there was little improvement when using filters of orders above four. The major advantage of a higher order filter is a more symmetric and thus shorter pulse, which may aid if pile-up is expected. However, a filter of order four or five already outputs a pulse with nearly equal rise and fall times.

#### 4. Tests Using an Arbitrary Waveform Generator

A test setup has been built in order to determine, primarily, the timing resolution of various FADC setups (Fig. 52) and, additionally, to provide validation for the simulations. The setup consisted of an arbitrary waveform generator (AWG) Agilent 33600A with 80 MHz analog bandwidth, and sampling rate of 1 GSPS, which created signals resembling what is expected to be seen from a photomultiplier (PMT). We have chosen to use an AWG instead of a PMT because the purpose of the tests was to assess the performance of the electronics only, and the PMT would introduce additional, possibly dominant errors to the time measurements. One channel of the AWG was connected directly to the ADC, while the other was connected to the shaper, which in turn was connected to the second channel of the ADC. The shaping amplifiers were designed based on the results of the study of

the timing performance of the digital constant fraction algorithm. One nominally has an impulse response with a 15 ns rise-time while another has a response with a 30 ns rise-time. Lastly, three different commercial ADCs or ‘digitizers’ have been investigated:

- The CAEN DT5724; 100 MSPS, 14-bit, 4 channels
- The CAEN V1720; 250 MSPS, 12-bit, 8 channels
- The CAEN V1730; 500 MSPS, 14-bit, 16 channels

To obtain our timing resolution measurements two pulses are simultaneously generated by the AWG, one large ‘reference’ pulse with a high SNR, and a smaller ‘signal’ of the same form that gets manipulated for testing. The reference pulse heads straight to the ADC but the signal pulse passes through one of the shapers first. The arrival time of each pulse is deduced in ROOT by fitting a skewed Gaussian to the data. The skewed Gaussian was chosen because the waveform seemed to rise slightly quicker than it dropped. This function has a number of parts but is of the form

$$f(x) = \frac{\phi(y)}{\alpha - \kappa(x - \xi)}$$

where  $\phi(y)$  is a standard Gaussian,  $\xi$  is the mean,  $\alpha$  is a scaling factor,  $\kappa$  is a skewing factor, and

$$y = -\frac{1}{\kappa} \log[1 - \kappa(x - \xi)/\alpha].$$

After fitting, the peak time of the fit is chosen as the pulse arrival time to be used. The difference in the pulse times between the reference and shaper signals was calculated for several thousand events, and the timing resolution is

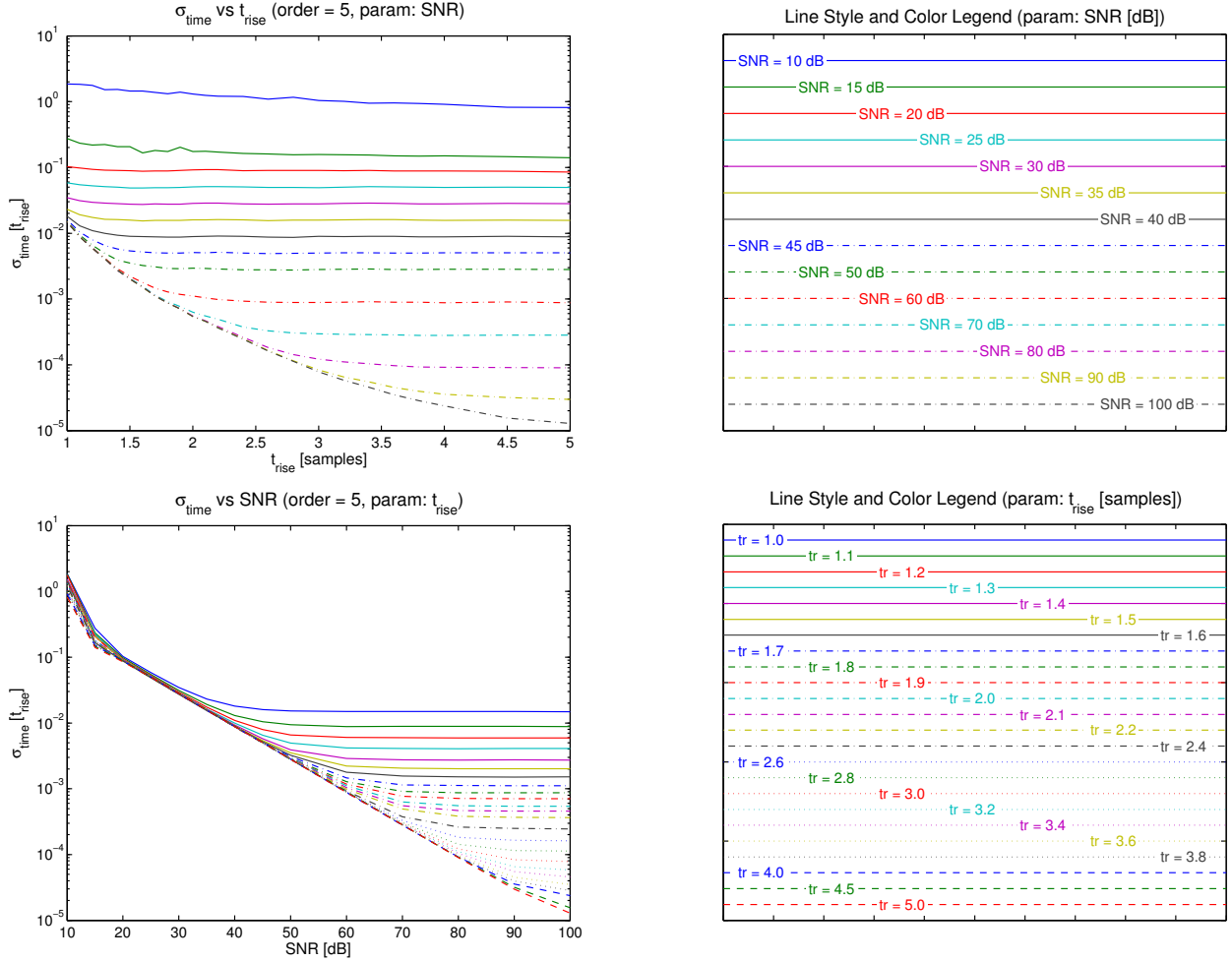


FIG. 51. Results of the study of the timing resolution of the digital constant fraction algorithm. The top row shows results parameterized by the signal-to-noise ratio (SNR), whereas the bottom row show the same data but parameterized by the amount of samples at the rising edge of the pulse (10% to 90% of the amplitude).

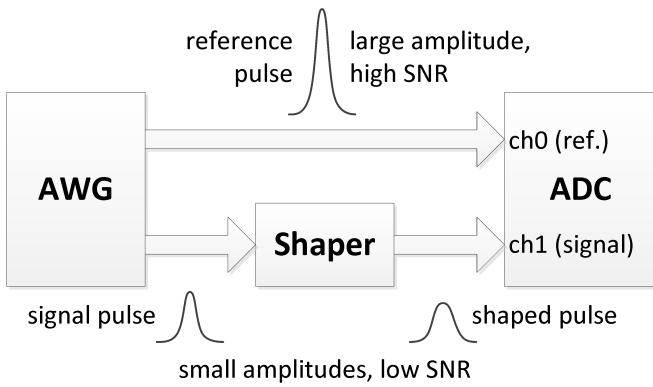


FIG. 52. Measurement setup for studying time resolution of various configurations of ADCs and shapers.

taken from the RMS of the distribution of timing differences. The signal pulse has been manipulated in various ways to see how timing resolution is affected. The mod-

ifications included varying the pulse height, passing it through long cables, and using a double or twin pulse waveform.

Fig. 53 shows timing resolution vs. signal pulse height for the three different digitizers and each shaper. Not surprisingly the 500 MSPS digitizer, offering many samples along the pulse, performed the best. Nevertheless, the 100 MSPS digitizer seems to offer near the same resolution and appears to be a better choice, as it is less expensive. Trailing behind is the 250 MSPS, which has worse SNR due to lower accuracy (12-bit as opposed to 14-bit in the other two). This seems to confirm that it is the signal to noise ratio that is the key issue. However, it should be mentioned that the shapers were optimized for the 100 MSPS digitizer and in the 250 MSPS and 500 MSPS cases the pulse shape was suboptimal. Still another conclusion is that the 15 ns shaper gave better results than the 30 ns one – which again agrees with the simulation and suggest that an attention should be paid to choosing proper shaping times.

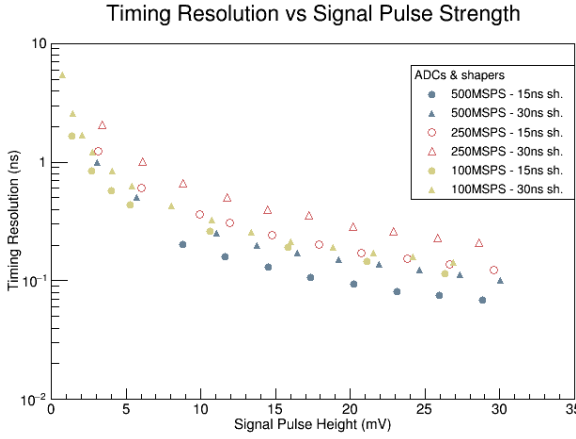


FIG. 53. Timing resolution vs. signal pulse height for both shapers and all three digitizers.

One of the tests performed was to see how sending the signal pulse through a long cable would affect characteristics such as its attenuation and the timing resolution. Fig. 54 results for the signal pulse that was sent through a 450ft cable under two different configurations – the shaper placed before the cable and the shaper placed afterwards. The 100 MSPS digitizer was used for this test. What was quite positive about these results was that, for the shaper-before configuration, the timing resolution was entirely unaffected, even after almost 50% attenuation. The shaper-after configuration however consistently worsened the resolution - which agrees with expectation, as in this configuration the SNR deteriorates with increasing the cable length. These results indicate that, with the proper signal amplification at each PMT, there is quite some freedom in the choosing PMT and electronics design, because such long cables can be used.

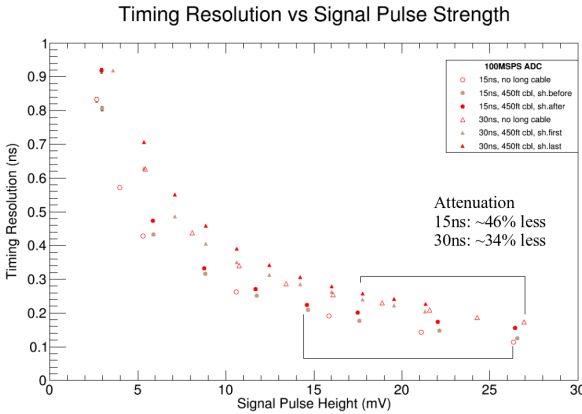


FIG. 54. Timing resolution vs. signal pulse height with and without the addition of a long 450ft cable. One configuration had the shaper placed before and another had the shaper placed after the long cable.

Finally, time resolution measurements have been done using a double pulse structure for the signal, with pulse separations ranging from 40 ns up to 120 ns. An example pulse is shown in Fig. 55. For the 15 ns shaper, the resolution was quite stable even after the pulses were significantly overlapping at around 40 ns, as shown in Fig. 56. These tests were done with the 100 MSPS digitizer, though it might be interesting to see how other digitizers perform considering that the 100 MSPS is limited in how close the pulses can be brought together. Even so, the resolution on the latter pulse compares extremely well under this configuration, deviating by only  $\approx 0.01$  ns.

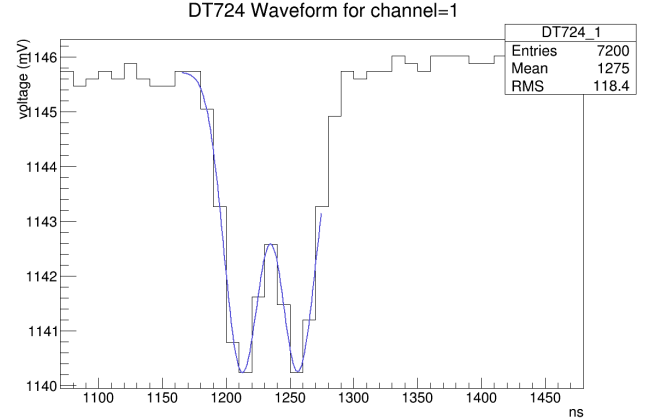


FIG. 55. Double pulse with the 15ns shaper and 100 MSPS digitizer, along with a fitted function to determine peak times.

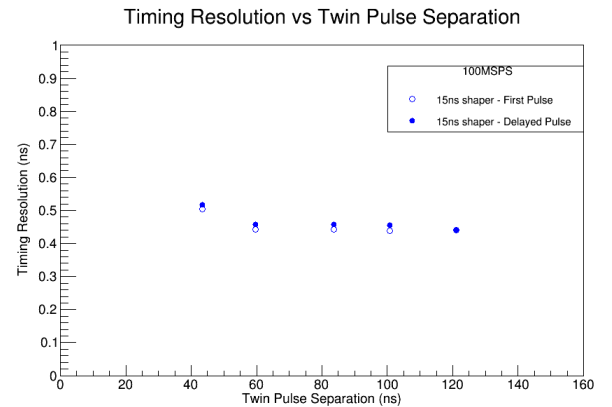


FIG. 56. Timing resolution vs. twin pulse peak separation.

##### 5. Noise Study and Optimum Filtering

Since the amount of noise is a key factor determining performance of the whole system, a detailed noise study has been performed using the equipment described in section III G 4. Noise data was acquired using several equipment configurations for the 100 MSPS and 250 MSPS digitizers, including:

1. ADC with both inputs unconnected
2. ADC with one input unconnected and the other input connected to the output of the shaper. The shaper's input was left floating.
3. Both inputs of the ADC connected to the AWG, with the AWG turned on but producing no signal.
4. One input of the ADC connected to the AWG and the other connected to the shaper. The shaper input is connected to the second channel of the ADC. The AWG was on, but again producing no signal. This was the configuration used for testing the time resolution in section III G 4.

Runs in each of the configuration consisted of several thousands of events and the acquisition time for a single event was 100  $\mu\text{s}$ . Afterwards, an estimate of noise spectrum was calculated using a smoothed, averaged periodogram, with a frequency resolution of 10 kHz. Prior to periodogram calculation, samples from each event were processed by the Hanning window. The window length was equal to the amount of samples in the event. Figs. 57 and 58 show an example noise spectrum for the configuration 'ADC+shaper' (III G 4), for both 100 MSPS and 250 MSPS digitizers, respectively. As expected, it can be clearly observed that the 12-bit ADC is noisier than the 14-bit one. Furthermore, the noise spectrum is not white, i.e. sample-to-sample correlations are present. The frequency peaks also indicate presence of deterministic components, probably due to electromagnetic interference pickup.

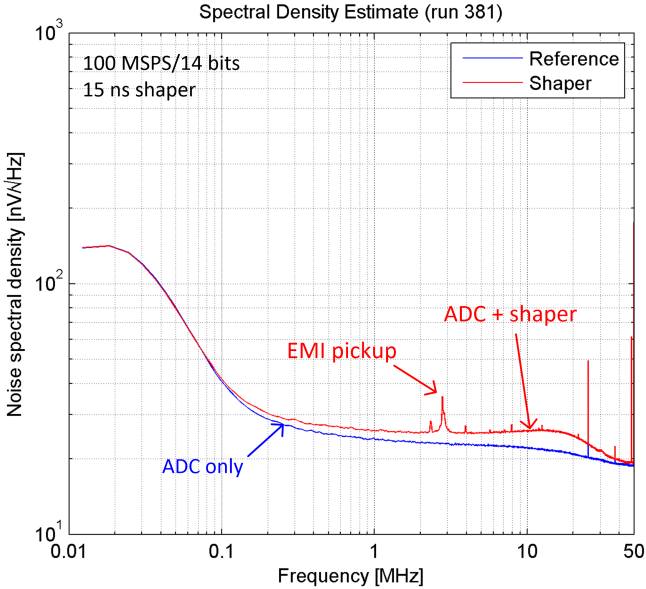


FIG. 57. Example estimates of noise spectrum of the 100 MSPS, 14-bit digitizer (CAEN DT5724). The 'reference' channel had unconnected input (blue curve), while the 'shaper' channel had its input connected to the 15 ns shaper (red curve). The input of the shaper was unconnected.

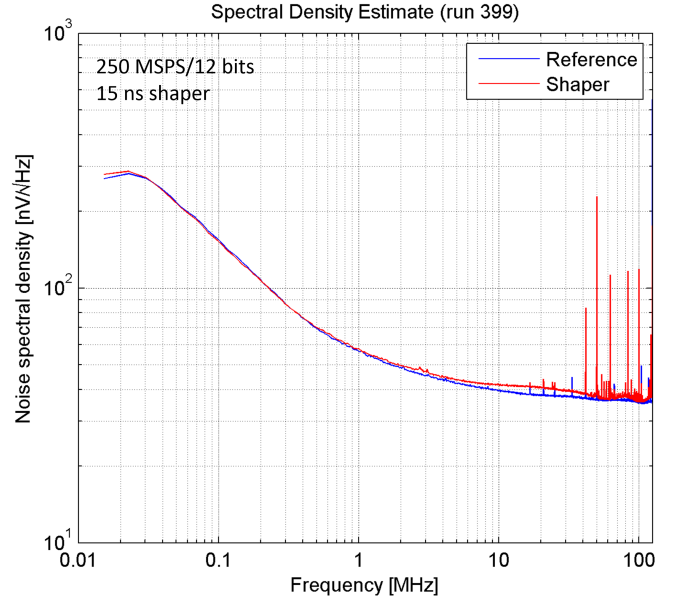


FIG. 58. Example estimates of noise spectrum of 250 MSPS, 12-bit digitizer (CAEN V1720). The 'reference' channel had unconnected input (blue curve), while the 'shaper' channel had its input connected to the 15 ns shaper (red curve). The input of the shaper was unconnected.

Based on the results of the above measurements and information available in published articles, the following requirements for the signal processing methods were formed:

- Account for arbitrary noise spectrum present in real experimental conditions, in particular ability to work in presence of correlated noise.
- Ability to filter out individual frequency components originating from a pickup of electromagnetic interference.
- Ability to remove the DC component of the signal, thus removing the need for pedestal estimation.
- Shorten the pulses by performing some form of deconvolution, thus improving the ability to properly detect events that are closely spaced in time.
- Minimize effects of quantization noise resulting from limited number of ADC bits, therefore allowing for use of less precise digitizers.

Given the above requirements, the finite impulse response (FIR) filters were chosen.

From our perspective, the FIR filter can be treated as a 'black box' that changes one signal into another, which is more appropriate for further processing, be it estimation of time of arrival or estimation of charge. Each sample of the output signal is a convolution of the filter's impulse response and the input signal or, in other words, each

output sample is a weighted sum of samples of the input signal:

$$y[n] = \sum_{l=0}^{N-1} h[l] \cdot x[n-l] \quad (11)$$

where  $y$  is the output signal,  $x$  is the input signal,  $h$  is the filter's impulse response and  $N$  is the number of filter taps (i.e. number of input samples used in calculation of the output sample). Two big advantages of this approach are:

- An arbitrary filter impulse response is possible.
- By definition, the algorithm is stable.

The key issue is the choice of optimal shape of the output pulse and of the filter's impulse response.

Based on the published literature (for example [48]), we propose to use the 'Digital Penalized Least Mean Squares' (DPLMS) method [49–52] for the synthesis of the filter response. We intend to use two filters, one optimized for pulse timing [53] and the other one optimized for charge estimation (Fig. 59). The studies of the method are on-going.

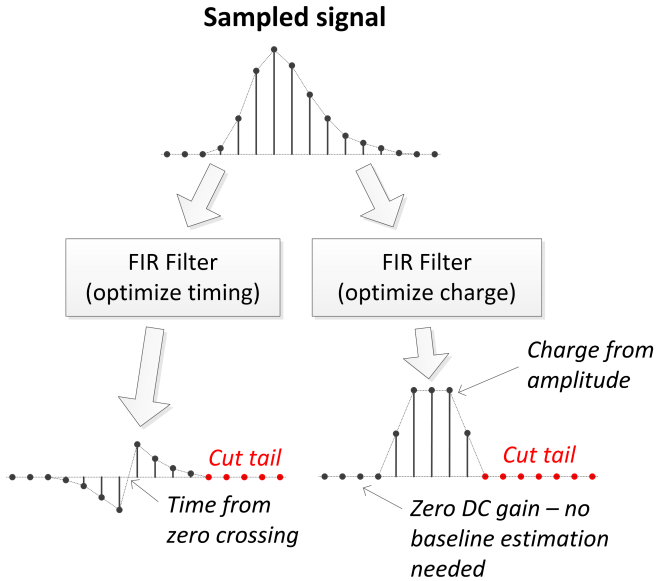


FIG. 59. Overview of the proposed signal processing using finite impulse response filters.

## H. Water System

Starting with the very first large-scale Water Cherenkov detector – the Irvine Michigan Brookhaven [IMB] proton decay experiment, which began taking data in the early 1980's – exceptional water clarity has been of key importance for massive devices of this kind. There is little benefit in making a very large detector unless

the target mass contained within the detector can be efficiently observed. Good water quality has two main advantages: the light generated by physics interactions in the water can propagate long distances with minimal attenuation until it is collected by photomultiplier tubes or other technologies, aiding accurate energy reconstruction, and the light can traverse these distances (10's of meters) with minimal scattering, which aids in the precise reconstruction of event vertices.

The strategy employed to create kilotons of extremely clear water has been to remove all suspended solids, dissolved gases, ions, and biologics from solution via a series of filtration elements. These include microfiltration filters, degasifiers (vacuum and/or membrane type), reverse osmosis membranes [RO], de-ionization resins [DI], and exposure to intense ultraviolet light [UV].

These water systems typically run in one of two modes: fill or recirculation. During the fill mode, water supplied by the local municipality or ground water in the vicinity of the experiment is first brought up to ultrapure levels and then injected into the detector. The capacity of the water system, along with availability of water, defines how long it will take to fill the detector. During recirculation mode, already high-quality water from the detector is continuously passed through the filtration system and returned to the detector after being cleaned even further. This is necessary as transparency-impairing materials are steadily leaching into the chemically active ultrapure water. In addition, during the process of filtration the water is typically chilled to further impede biological growth, with the added benefit of simultaneously reducing PMT dark noise which is typically strongly temperature dependent.

In the current baseline design, NuPRISM will have interior dimensions ten times smaller than Super-K. It is therefore possible that a commensurately less powerful water filtration system would be able to provide sufficient water transparency. Nevertheless, for now we will base our initial system design and flow rates on water systems known to have worked and produced useful physics in the past.

Following this approach, a baseline design and cost estimate for the NuPRISM water system has been prepared. The primary components described above are represented graphically in Figure 60. This system will be capable of filling the detector at a rate of 6.3 tons/hour, such that a complete fill can be completed in one month of operations. It will be capable of recirculating the water at a rate of 6.3 tons/hour through the entire system plus an additional 22.8 tons/hour through what is known as a secondary "fast recirculation" path which trades some filtration components for faster overall flow. The combination of complete cleaning and fast recirculation has been shown at previous experiments (including the K2K one kiloton near detector) to be the most cost-effective way of achieving the desired water transparencies. A preliminary cost estimate for this baseline water system from South Coast Water in the is \$350,000, including shipping,

duties, and installation at the detector site.

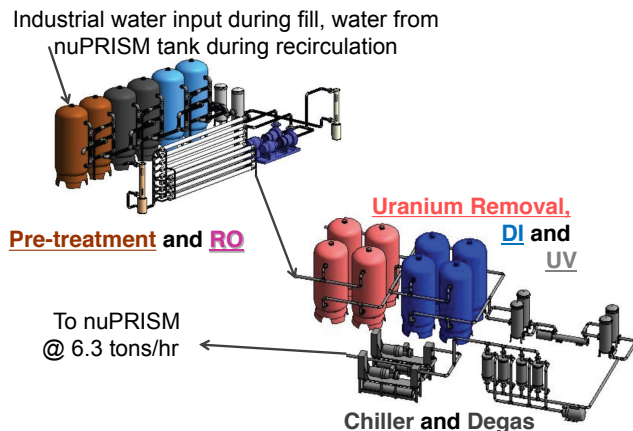


FIG. 60. A preliminary baseline design of the NuPRISM water system.

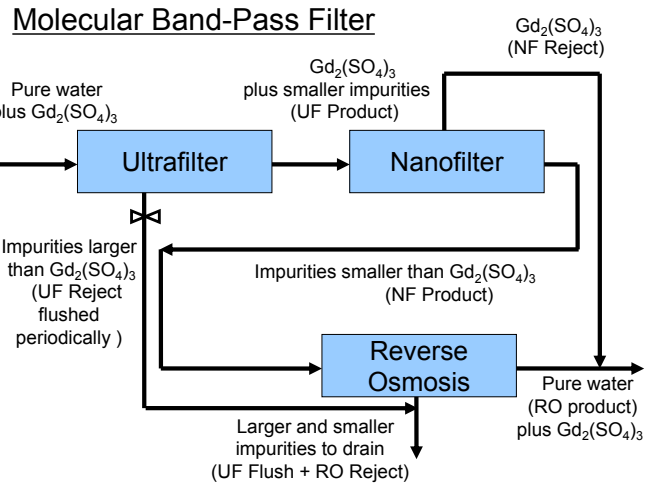


FIG. 61. A schematic illustration of the principle of the "molecular band-pass filter". Successively fine filter elements isolate the dissolved gadolinium sulfate ions and return them to the main tank, bypassing water system elements which would be fouled if they were to trap gadolinium.

### 1. *Gd option*

If it is decided to add 0.2% gadolinium sulfate by mass to Super-Kamiokande in order to provide efficient tagging of neutrons in water, it will likely be useful for a near detector at Tokai to also be Gd-loaded such that the responses of both detectors are as similar as possible. As a large water Cherenkov detector, NuPRISM is a natural candidate for eventual Gd-loading. Therefore, the implications this has on the water system design must be taken into account.

Over the past decade there have been focused R&D programs both in the US and Japan aimed at devising a method capable of maintaining the exceptional water transparency discussed above, while at the same time maintaining the desired level of dissolved gadolinium in solution. In other words, somehow the water must be continuously recirculated and cleaned of everything *except* gadolinium sulfate.

Starting in 2007 with a 0.2 ton/hour prototype at the University of California, Irvine, since 2009 the Kamioka-based EGADS (Evaluating Gadolinium's Action on Detector Systems) project has shown that such a selective water filtration technology – known as a "molecular band-pass filter" and schematically shown in Figure 61 – is feasible at 3 tons/hour. As the EGADS design is modular and uses off-the-shelf and readily available equipment, albeit in novel ways, scaling it up from the current 3 tons/hour to 60 tons/hour for Super-Kamiokande, is straightforward, while scaling to NuPRISM's 6.3 tons/hours would be trivial.

## IV. DETECTOR CALIBRATION

The calibration systems for NuPRISM will largely borrow from the existing Super-K calibration systems. However, NuPRISM will also face some unique challenges:

- The PMT frame will move within the water volume.
- Accessing the inner detector is more difficult when the position of the top of the detector is not fixed.

To address these issues, NuPRISM will consist of calibration sources that are fixed within the ID (e.g. laser balls, LEDs, and scintillation cubes), as well as sources that can be lowered through remote-controlled access portals (e.g. radioactive sources). It is expected that each time the detector is moved, all of the PMTs will need to be recalibrated. This can be accomplished using the fixed light sources within the ID, and additional calibration runs with radioactive sources will be taken for each new detector position.

In addition to the detector response, it will also be necessary to precisely determine both the relative position of the PMTs within the ID, as well as the absolute position of the PMT frame within the water volume. This will be accomplished with a laser calibration system. An R&D program is planned to demonstrate the effectiveness of such a system when operated in water.

As NuPRISM will essentially reuse many of the established Super-K calibration techniques, the remainder of this section will provide a brief description of Super-K calibration systems. Further details can be found elsewhere [16, 17].

### A. Overview of Super-K Calibration Systems

This section overviews Super-K detector calibrations. For further details, reader can also refer to [16, 17].

The Super-K detector calibration can be divided into two steps; the detector hardware calibrations and the calibrations for physics analyses. The first step is common over all physics analyses, but the second step is designed for each physics analysis goal.

#### 1. Detector hardware calibrations

The detector hardware calibrations (measurements) consist of several parts:

- Geometrical surveys: tank geometry, PMT positions
- Geomagnetic field
- PMT calibration: gain, photo-detection efficiency
- Readout channel (PMT and electronics) calibrations: linearity, timing, timing resolution

- Optical properties: water, PMT glass, black sheet, etc (for detector MC tuning)
- Water temperature

All of these calibrations and measurements are indispensable to understand the detector and to model the detector in the simulation. This section focuses on the PMT calibrations and readout channel calibrations, which will be most relevant to NuPRISM.

The PMT calibration procedure can be divided into three large steps; 1) pre-calibration, 2) post-installation calibration, 3) detector monitoring. At the stage of ‘pre-calibration’, a fraction of all Super-K PMTs have been calibrated prior to the installation, e.g. a tuning of PMT gain. The pre-calibrated PMT, called *standard PMTs*, were used to calibrate all other PMTs *in-situ* after installed, at the stage of post-installation calibration. Once all PMT are calibrated, the stability of the PMTs is monitored continuously for the lifetime of the experiment. The following sections discuss our ideas for each of the PMT calibration steps.

*a. Pre-calibration* SK has 420 standard PMTs, which corresponds to about 4% of all SK PMTs. The SK standard PMTs were calibrated prior to the installation by adjusting HV values to have identical charge ( $\sim 30$  p.e.) over the standard PMTs. For the pre-calibration, SK employed a xenon lamp and scintillator ball. Figure 62 shows a schematic diagram of the pre-calibration set-up.

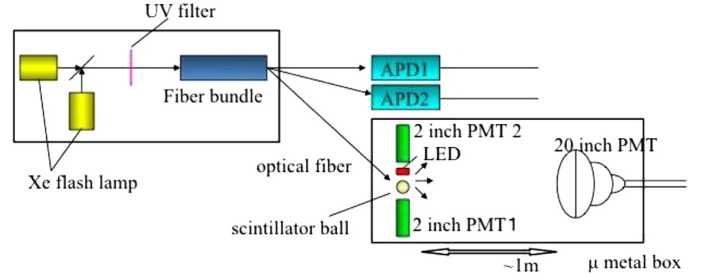


FIG. 62. SK pre-calibration set-up. (Figure quoted from [17])

The SK standard PMTs were installed in the tank in a geometrically symmetric configuration. Figure 63 shows the location of the standard PMTs in SK inner detector.

*b. Post-installation calibrations* In the post-installation calibration, all PMTs other than the standard PMTs were calibrated *in-situ* after installed. At this stage, all PMT parameters were determined and measured. We will discuss the following items in this section,

#### • HV (gain) tuning

Tune HV for all PMTs, referencing to the standard PMTs by using the Xe lamp and deploying a scintillator ball in the tank (the same light source used in the pre-calibration). Move the scintillator ball along Z-axis (height direction), and tune

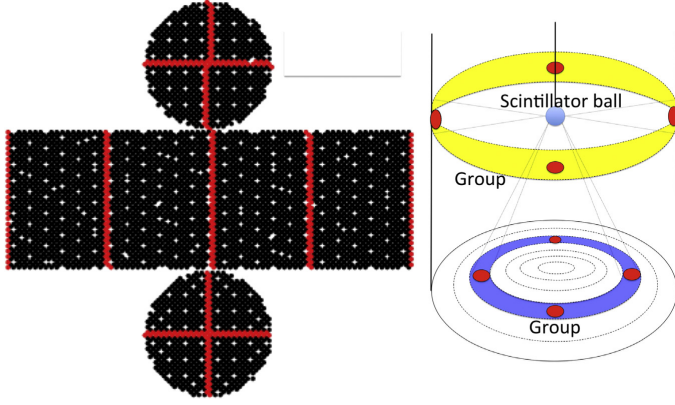


FIG. 63. Layout of SK standard PMTs. (Figure quoted from [17])

HV group-by-group, where the group is defined by Fig. 63.

- Charge to photo-electron conversion

Conversion factor of charge (pC) to photo-electron (p.e.) were obtained by measuring 1 p.e. distribution. SK deployed “nickel source” in the tank, that generate 1 p.e. level of light, where the nickel source is nickel-californium source;  $\text{Ni}(n,\gamma)\text{Ni}$ ,  $E_\gamma \sim 9 \text{ MeV}$ . Figure 64 shows the SK nickel source.

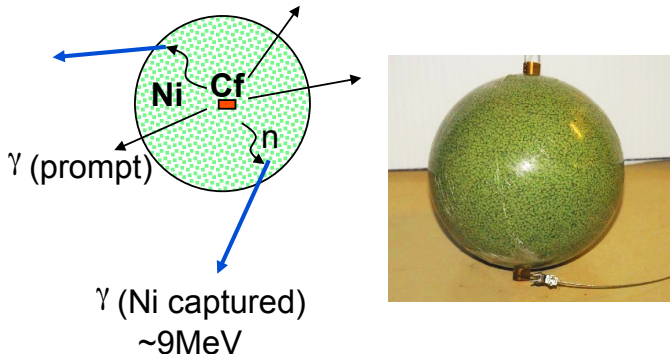


FIG. 64. SK ‘Nickel source’ (Figure quoted from [17])

- Photo-detection efficiency

The photo-detection efficiency,  $\epsilon$ , is defined by Quantum Efficiency times Collection Efficiency (CE). Hit rate ( $N_{\text{hit}}$ ) for 1 p.e. level of light is proportional to the photo-detection efficiency;  $N_{\text{hit}} \propto N_{\text{photon}} \cdot \epsilon$ . For this measurement, SK used the Nickel source to evaluate the hit rate, and compare with MC to evaluate *relative* efficiency over all PMTs.

- Timing calibration

Calibration for time response of readout channel (PMT and electronics), e.g. *time-walk* effect. SK

employed  $\text{N}_2$ -dye laser and deployed diffuser-ball in tank, that light source can generate 0.1~1000 p.e. level light and covers the entire dynamic range of electronics. Evaluate TQ-maps for every single PMTs, and evaluate detector timing resolution (for MC input).

## 2. Calibrations for physics analyses

The calibrations for physics analyses need to be designed for physics goal basis. This section describes the calibrations used for SK atmospheric neutrino and T2K analyses, that relevant to NuPRISM physics goals.

*a. Photon yield and charge scale* Although several detailed detector calibrations have been carried out, there are uncertainties on the photon propagation and photon detection of the detector, that need to be tuned in the detector simulation using a well known control samples. For that, SK uses cosmic-ray muons, called “vertical through-going muons”. Figure 65 shows a schematic of vertical through-going muon event of SK. The absolute

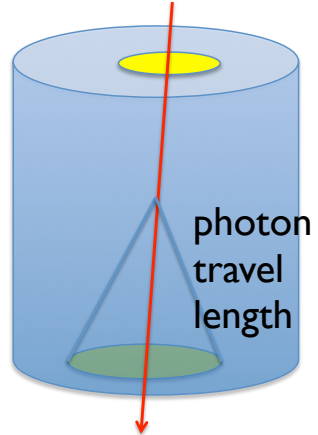


FIG. 65. Schematic of SK vertical through-going muon events.

photon yield and charge scale in the detector simulation have been tuned to data using the vertical through-going muon events that provide known muon track length and Cherenkov photon travel distance.

*b. Momentum and energy scale* SK event reconstruction algorithm uses a conversion table that translate the observed total charge in the Cherenkov ring to the particle (muons and electrons) momentum. The conversion table is called “momentum table” have been evaluated using the detector simulation by generating particles in momentum range of 10’s MeV/c to GeV/c. Based on all detector calibrations and the simulation tuning, the detector and simulation are ready to use for physics analyses. Absolute energy scale is checked using natural sources; decay electron,  $\pi^0$  mass, sub-GeV stopping muons, and multi-GeV stopping muons, these sources

cover the energy range of 10's MeV to 10 GeV. SK detector simulation reproduces data within  $\sim 2\%$  and that have been continuously monitored. SK defines the energy scale uncertainty as the data-MC difference. If the simulation does not reproduce the data reasonably well, the detector calibrations and simulation tuning need to be revised.

## V. CONCLUSION

The proposed NuPRISM detector has the potential to address the remaining systematic uncertainties that are not well constrained by ND280. In particular, this detector can constrain the relationship between measured lepton kinematics and incident neutrino energy without relying solely on rapidly-evolving neutrino interaction models. Since NuPRISM is a water Cherenkov detector, the neutral current backgrounds with large systematic uncertainties at Super-K, particularly  $NC\pi^+$  and  $NC\pi^0$ , can be measured directly with a nearly identical neutrino energy spectrum. The ability to produce nearly monoenergetic neutrino beams also provides the first ever ability to measure neutral current cross sections as a function of neutrino energy. Finally, NuPRISM provides a mechanism to separate the many single-ring e-like event types to simultaneously constrain  $\nu_e$  cross sections, neutral current background, and sterile neutrino oscillations.

The main long-baseline oscillation analysis presented

in this note was a  $\nu_\mu$  disappearance measurement, since the effects of various cross section models on this measurement had already been well studied, which provided a useful basis for comparison. However, it is also expected that NuPRISM will provide a significant improvement to the ultimate T2K constraint on  $\delta_{CP}$  by constraining neutral current backgrounds and electron-neutrino cross sections. Initial studies have also been presented that demonstrate the impact NuPRISM can have on both  $\nu_e$  appearance measurements and anti-neutrino oscillation measurements. Other planned improvements to the analysis include a realistic detector simulation and event reconstruction. Thanks to the work done on event simulation and reconstruction in Hyper-K, these tools already exist and can be quickly incorporated into the current analysis to perform more detailed studies of event pileup and detector performance for various detector configurations and PMT sizes and coverage.

Cost estimates for NuPRISM are still preliminary, but initial quotes have been obtained for the most expensive components of the project: the civil construction and PMTs. Initial quotes have been received for these two items, which provides an initial cost estimate for the total project of US\$16.3 million. There are still uncertainties associated with this cost estimate that will be reduced before the experiment proposal is submitted. More details regarding the project cost can be found in the appendix. Once funded, NuPRISM is expected to take less than 3 years to construct, based on the experience from the T2K 2 km detector.

- 
- [1] T. Dealtry *et al.* T2K-TN-172 (2014)
  - [2] C. H. Llewellyn Smith, Phys. Rept. **3**, 261 (1972).
  - [3] R. A. Smith and E. J. Moniz, Nucl. Phys. B **43**, 605 (1972) [Erratum-*ibid.* B **101**, 547 (1975)].
  - [4] O. Benhar, A. Fabrocini and S. Fantoni, Nucl. Phys. A **505**, 267 (1989).
  - [5] J. Marteau, Eur. Phys. J. A **5**, 183 (1999) [hep-ph/9902210].
  - [6] M. Martini, M. Ericson, G. Chanfray and J. Marteau, Phys. Rev. C **80**, 065501 (2009) [arXiv:0910.2622 [nucl-th]].
  - [7] M. Martini, M. Ericson, G. Chanfray and J. Marteau, Phys. Rev. C **81**, 045502 (2010) [arXiv:1002.4538 [hep-ph]].
  - [8] M. Martini, M. Ericson and G. Chanfray, Phys. Rev. C **84**, 055502 (2011) [arXiv:1110.0221 [nucl-th]].
  - [9] J. Nieves, I. Ruiz Simo and M. J. Vicente Vacas, Phys. Rev. C **83**, 045501 (2011) [arXiv:1102.2777 [hep-ph]].
  - [10] Melanie Day, Kevin S. McFarland, Differences in Quasi-Elastic Cross-Sections of Muon and Electron Neutrinos Phys.Rev. D86 (2012) 053003
  - [11] Yu. Kudenko (for the T2K Collaboration), Nucl. Instr. and Meth. A598 (2009) 289-295; K. Abe *et al.*, (The T2K Collaboration) Nucl. Instr. and Meth. A **659** (2011) 106.
  - [12] D. Renker, and E. Lorenz, JINST 4 (2009) P04004.
  - [13] M. Yokoyama *et al.*, Nucl. Instr. and Meth. A **610** (2009) 128; M. Yokoyama *et al.*, Nucl. Instr. and Meth. A **622** (2010) 567; A. Vacheret *et al.*, Nucl. Instr. and Meth. A **656** (2011) 69.
  - [14] Yu.Musienko, New developments in solid state photomultiplier, talk at the International Conference "Instrumentation for Colliding Beam Physics" (INSTR14), 24 February - 1 March 2014, Novosibirsk, Russia.
  - [15] K. Abe, T. Abe, H. Aihara, Y. Fukuda, Y. Hayato, K. Huang, A. K. Ichikawa and M. Ikeda *et al.*, arXiv:1109.3262 [hep-ex].
  - [16] Y. Fukuda *et al.* [Super-Kamiokande Collaboration], Nucl. Instrum. Meth. A **501**, 418 (2003).
  - [17] K. Abe, Y. Hayato, T. Iida, K. Iyogi, J. Kameda, Y. Kishimoto, Y. Kosho and L. Marti *et al.*, Nucl. Instrum. Meth. A **737**, 253 (2014) [arXiv:1307.0162 [physics.ins-det]].
  - [18] O.Mineev *et al.*, JINST **6** (2011) P12004; arXiv:1110.2651 [physics.ins-det].
  - [19] Y. Kudenko *et al.*, Nucl. Instr. Meth. A469 (2001) 340.
  - [20] S. Nakayama *et al.* [Hyper-Kamiokande Working Group], "Hyper-K Tank", Talk at the 4th Open Meeting for the Hyper-Kamiokande Project, <http://indico.ipmu.jp/indico/getFile.py/access?contribId=29&sessionId=4&resId=0&materialId=slides&confId=29>
  - [21] MiniBooNE collaboration, Phys.Rev.Lett.102(2009)101802

- [22] nuSTORM - Neutrinos from STORed Muons: Proposal to the Fermilab PAC, arXiv:1308.6822
- [23] E. Akhmedov, Nucl. Phys. Proc. Suppl. **188**, 204 (2009) [arXiv:0901.3450 [hep-ph]].
- [24] S. Razzaque and A. Y. Smirnov, JHEP **1505**, 139 (2015) [arXiv:1406.1407 [hep-ph]].
- [25] G. D. Barr, T. K. Gaisser, S. Robbins and T. Stanev, Phys. Rev. D **74**, 094009 (2006) [astro-ph/0611266].
- [26] C. Consolandi [AMS 02 Collaboration], arXiv:1402.0467 [astro-ph.HE].
- [27] N. Abgrall *et al.* [NA61/SHINE Collaboration], Phys. Rev. C **84**, 034604 (2011) [arXiv:1102.0983 [hep-ex]].
- [28] K. Abe *et al.* [T2K Collaboration], Phys. Rev. D **87**, 092003 (2013) [arXiv:1302.4908 [hep-ex]].
- [29] Y. Nakajima *et al.* [SciBooNE Collaboration], Phys. Rev. D **83**, 012005 (2011) [arXiv:1011.2131 [hep-ex]].
- [30] B. G. Tice *et al.* [MINERvA Collaboration], [arXiv:1403.2103 [hep-ex]].
- [31] A. A. Aguilar-Arevalo *et al.* [MiniBooNE Collaboration], Phys. Rev. D **81**, 092005 (2010) [arXiv:1002.2680 [hep-ex]].
- [32] Y. Nakajima, [http://nuint11.in/final\\_nuint/cc%20quasi%20and%20nc%20elastic%20scattering/nakajima\\_nuint11.pdf](http://nuint11.in/final_nuint/cc%20quasi%20and%20nc%20elastic%20scattering/nakajima_nuint11.pdf)
- [33] VLyubushkin *et al.* [NOMAD Collaboration], Eur. Phys. J. C **63**, 355 (2009) [arXiv:0812.4543 [hep-ex]].
- [34] G. A. Fiorentini *et al.* [MINERvA Collaboration], Phys. Rev. Lett. **111**, no. 2, 022502 (2013) [arXiv:1305.2243 [hep-ex]].
- [35] R. Gran *et al.* [K2K Collaboration], Phys. Rev. D **74**, 052002 (2006) [hep-ex/0603034].
- [36] A. A. Aguilar-Arevalo *et al.* [MiniBooNE Collaboration], Phys. Rev. D **83**, 052007 (2011) [arXiv:1011.3572 [hep-ex]].
- [37] A. A. Aguilar-Arevalo *et al.* [MiniBooNE Collaboration], Phys. Rev. D **83**, 052009 (2011) [arXiv:1010.3264 [hep-ex]].
- [38] A. Rodriguez *et al.* [K2K Collaboration], Phys. Rev. D **78**, 032003 (2008) [arXiv:0805.0186 [hep-ex]].
- [39] C. Mariani *et al.* [K2K Collaboration], Phys. Rev. D **83**, 054023 (2011) [arXiv:1012.1794 [hep-ex]].
- [40] M. Hasegawa *et al.* [K2K Collaboration], Phys. Rev. Lett. **95**, 252301 (2005) [hep-ex/0506008].
- [41] O. Lalakulich and U. Mosel, Phys. Rev. C **88**, no. 1, 017601 (2013) [arXiv:1305.3861 [nucl-th]].
- [42] A. A. Aguilar-Arevalo *et al.* [MiniBooNE Collaboration], Phys. Rev. D **81**, 013005 (2010) [arXiv:0911.2063 [hep-ex]].
- [43] S. Nakayama *et al.* [K2K Collaboration], Phys. Lett. B **619**, 255 (2005) [hep-ex/0408134].
- [44] J. A. Formaggio and G. P. Zeller, Rev. Mod. Phys. **84**, 1307 (2012) [arXiv:1305.7513 [hep-ex]].
- [45] E. Hawker, Proceedings of the Second International Workshop on Neutrino-Nucleus Interactions in the Few-GeV Region, Irvine, CA, unpublished
- [46] T. Kikawa *et al.* T2K-TN-132 (2013)
- [47] E. Kearns *et al.* <http://www.phy.duke.edu/~walter/nusag-members/2km-proposal-05-05-30.pdf> (2005)
- [48] S. Riboldi, R. Abbiati, A. Geraci, and Emilio Gatti. Experimental Comparison of State-of-the-Art Methods for Digital Optimum Filter Synthesis With Arbitrary Constraints and Noise. *IEEE Transactions on Nuclear Science*, 52(4):954–958, August 2005.
- [49] S. Riboldi, A. Geraci, R. Abbiati, Emilio Gatti, and Gi-ancarlo Ripamonti. A new method for LMS synthesis of optimum finite impulse response (FIR) filters with arbitrary time and frequency constraints and noises. In *2002 IEEE Nuclear Science Symposium Conference Record*, volume 1, pages 198–202 vol.1, November 2002.
- [50] E. Gatti, A. Geraci, S. Riboldi, and G. Ripamonti. Digital Penalized LMS method for filter synthesis with arbitrary constraints and noise. *Nuclear Instruments and Methods in Physics Research Section A: Accelerators, Spectrometers, Detectors and Associated Equipment*, 523(12):167–185, May 2004.
- [51] A. Abba, F. Caponio, A. Geraci, and G. Ripamonti. Experimental implementation of LMS synthesis of optimum FIR filters with arbitrary time and frequency constraints and noises. In *2011 IEEE Nuclear Science Symposium and Medical Imaging Conference (NSS/MIC)*, pages 862–865, October 2011.
- [52] S. Riboldi, A. Pullia, F. Camera, S. Brambilla, and A. Geraci. Optimum synthesis of FIR filters with arbitrary time and frequency constraints for energy and time estimations in case of pulse-correlated noise. In *IEEE Nuclear Science Symposium Conference Record, 2007. NSS '07*, volume 1, pages 486–489, October 2007.
- [53] R. Abbiati, A. Geraci, Emilio Gatti, and Giancarlo Ripamonti. Application of a Digital Technique for Timing of Events From Scintillation Detectors. *IEEE Transactions on Nuclear Science*, 53(6):3850–3854, December 2006.

TABLE VII. Summary of nuPRISM project costs, excluding any contingency. Costs taken directly from the T2K 2 km proposal are labeled with \*

Item	Cost (US M\$)
Cavity Construction, Including HDPE Liner	6.00
*Surface Buildings	0.77
*Air-Conditioning, Water, and Services	0.50
*Power Facilities	0.68
*Cranes and Elevator	0.31
*PMT Support Structure	1.27
3,215 8-inch PMTs	4.30
PMT Electronics	1.45
*PMT Cables and Connectors	0.13
Scintillator Panels	0.36
Water System	0.35
Gd Water Option	0.15
*GPS System	0.04
Total	16.31

### Appendix A: Detector Costs

This appendix is intended to characterize the costs associated with building NuPRISM. Several companies have provided preliminary cost estimates for the cost drivers of the experiment, which allows for a preliminary estimate of the total project cost.

For many of the less expensive items, the costs presented here rely heavily on the experience from the T2K 2 km detector proposal, which was written in 2005 [47]. For now, we have assumed that the prices are the same as those listed in the 2 km detector, since inflation rates in Japan have stayed near zero during the 9 years since that proposal was written. The assumed exchange rate is 107 Japanese yen to the US\$.

A summary of the total project cost is given in Table VII, and each component is described in the following subsections. Note that these numbers do not contain any contingency, as was the case in the 2 km proposal.

The remaining item for which no price estimate is given is cost of acquiring or renting the experimental site. For the 2 km detector, the chosen site was initially owned by a private company before being acquired by Tokai village and offered to J-PARC to use at no cost. Other experiments in Japan, such as AGASA, instead rent the land from the owner. Since any solution for land acquisition will require input from J-PARC, and since the original 2 km site was acquired without any cost to the laboratory, no cost estimate for land acquisition is included in the total project cost at this time.

### 1. Civil Construction

As mentioned in Section III B, two construction groups have been consulted for preliminary cost estimates for constructing the shaft. The first group evaluated the ini-

tial cost of the civil construction by scaling with the excavation volume based on prior vertical tunnel constructions. Table VIII summarizes the initial cost estimation for each construction method.

TABLE VIII. Summary of initial cost estimation for civil construction. Five methods are considered: Pneumatic Caisson (PC), Soil Mixing Wall (SMW), New Austrian Tunneling (NAT), Urban Ring (UR), and Cast in-situ diaphragm wall (RC). A 70 m deep boring survey is assumed.

(Unit: Oku JPY, roughly corresponds to Million USD)

Method	PC	SMW	NAT	UR	RC
Survey			0.1		
Designing			0.15		
Land preparation			0.15		
Construction	7.7	5.9	5.3~6.1	7.5	7.5

The second company prefers the NAT method for constructing the shaft, and they estimate a total cost of US\$6M, including the HPDE liner, although this number is contingent on a geological survey to confirm the rigidity of the earth in that region. This estimate is more consistent with the cost listed in the 2 km detector proposal, which was listed at US\$9.3M, despite a much larger excavated volume that included the construction of an underground cavern.

### 2. Photomultiplier Tubes

Table IX shows a cost comparison of the various PMT options from Hamamatsu. The default design assumes 3,215 standard 8" PMTs, although several other options are being explored, as shown in the table. The cost of the newer Hybrid Photodetector (HPD) technology being considered for Hyper-K depends on the year in which the PMTs are requested, since further R&D is expected to bring the production costs down for these devices.

The ETEL/ADIT company based in the UK and Texas has also been consulted for supplying PMTs to NuPRISM. They can provide 8" or 5" PMTs, but they do not have the APD or high-QE options available from Hamamatsu. The provided quote for 3,000 8" PMTs is \$1,775 per tube, which is significantly higher than the Hamamatsu quote. However, further consultation is planned to determine the cost of the 5" PMT option.

### 3. PMT Electronics

Initial cost estimates for NuPRISM electronics were based on early HK presentations, where the cost per channel for the electronics was \$450 per channel. This included the estimate for the digitization, HV power supply, network and case components. Separate estimates for the cost per channel for an FADC option came to a

TABLE IX. The pricing scenarios from Hamamatsu for various PMT configurations are shown. All prices are given in Japanese Yen.

Name	QE%	Quantity	Price/PMT	Cost	Delivery
5" PMT	25	8,000	103,500	828M	any
5" PMT HQE	35	5,714	123,700	707M	any
8" PMT	25	3,215	143,000	460M	any
8" PMT HQE	35	2,296	170,500	391M	any
8" HPD HQE	35	2,296	264,000	606M	2014
	35	2,296	236,500	543M	2015
	35	2,296	209,000	480M	2016
20" PMT HQE	30	508	604,500	307M	2014
	30	508	572,000	291M	2015
	30	508	539,500	274M	2016
20" HPD HQE	30	508	715,000	363M	2014
	30	508	617,500	314M	2015
	30	508	520,000	264M	2016

lower value for the digitization part; so we might conservatively use HK's estimate for the cost per channel. Assuming that we are equipping 3,215 channels this results in \$1.45 million for NuPRISM electronics.

#### 4. OD Scintillator Panels

TABLE X. Rough cost of one extruded scintillator counter of  $2000 \times 200 \times 7$  mm<sup>3</sup> with WLS fiber readout.

Material/labor	cost in US\$
One extruded slab covered by a reflector	70
WLS fiber Y11, 6 m long, 2\$/m	12
Optical glue, 2 g/m, 0.3\$/g	3.6
Optical connectors 2 × 0.25	0.5
MPPC 2 × 10\$	20
Labor	13.9
Total	120

The rough cost estimation of one counter ( $2000 \times 200 \times 7$  mm<sup>3</sup>) is given in Table X. The total surface of the NuPRISM detector (10 m in diameter, 14 m in height) is about 600 m<sup>2</sup>. About 3000 counters will be needed to cover the detector surface completely. The rough total cost of this veto detector (without mechanics and electronics) is estimated to be about 360 k\$US. Assuming similar production speed as obtained in the SMRD case it will take 12-14 months to extrude 3000 scintillator slabs of suitable dimensions and finally make all veto counters at the INR workshop.

#### 5. Water System

The water system is modeled after the Super-K water system, just as was done for the 2 km detector. We have consulted South Coast Water for an estimate of the cost of each of the system components, which resulted in a cost of US\$0.35M. This is only slightly higher than the US\$0.32M cost assumed in the 2 km proposal.

By scaling from the running EGADS system, it is possible to estimate for adding the additional components needed to handle gadolinium to the baseline system described above. Including the extra equipment required to make the baseline water system Gd-capable primarily means adding filtration elements called nanofiltration. Beyond that, there would have to be a small standalone system for dissolving, pre-purifying, and then injecting the gadolinium sulfate, as well as a standalone system to capture the gadolinium whenever the NuPRISM tank needed to be drained for servicing. All of this would increase the total cost of the complete NuPRISM water system from US\$0.35 to US\$0.50.



*Nuclear and Particle Physics, Astrophysics, and Cosmology*

T-2

PO Box 1663, MS B283  
Los Alamos, New Mexico 87545  
Phone 505-667-6245/Fax 505-667-1931

*Date:* June 12, 2015

To whom it may concern:

With this letter we express our strongest support for the construction of the nuPRISM detector in the J-PARC neutrino beam-line.

One of the goals of the international high-energy physics community is to measure the properties of neutrinos---their oscillation parameters and mass hierarchy-- and to determine the charge-conjugation parity (CP) violating phase differentiating the oscillation probabilities of neutrinos versus anti-neutrinos. The success of this experimental program hinges crucially on our ability to model accurately and precisely neutrino-nucleus interactions in order to unravel the response of neutrino detectors to be used in experiments, particularly since the latter aim at percent-level measurements of neutrino event rates and precise measurements of their energy distribution.

The nuPRISM detector with its capability of providing "pseudo-monochromatic" neutrino beams offers unique opportunities to test our understanding of weak interaction dynamics in nuclei at intermediate values of lepton energy and momentum transfers. For example, first-principles quantum Monte Carlo (QMC) calculations of weak response functions in this regime (momentum transfers less than 1 GeV/c and energy transfers in the threshold and quasi-elastic regions), based on realistic nuclear interactions and electro-weak currents, predict that these response functions are significantly increased by two-body contributions not only in the vector component of the weak current but also in its axial component. While the enhancement of the vector response, specifically the transverse one, has been confirmed by  $(e,e')$  inclusive data, no direct experimental corroboration exists for this prediction in the case of the axial and vector-axial interference responses, the latter, in particular, differentiates between neutrino and anti-neutrino cross sections and is therefore crucial for studies of mass hierarchy and CP violation. The unique ability of the nuPRISM detector to obtain quasi monochromatic beams will enable a much more direct comparison with monochromatic electron scattering, and hence put much more severe constraints on the axial and vector-axial interference terms in the response. The combination of theory and experiments such as nuPRISM is critical in obtaining the precision needed in our understanding of neutrino-nucleus interactions.

Clearly a detector such as nuPRISM would represent a dramatic step forward in our ability to test in detail our understanding electroweak structure and dynamics of nuclei. This increased understanding is certain to have impacts in a variety of weak interaction experiments with nuclei, particularly the short- and long-baseline accelerator neutrino experiments. We support it wholeheartedly.

Sincerely,

J. Carlson (LANL)  
S. Gandolfi (LANL)  
A. Lovato (ANL)  
S.C. Pieper (ANL)  
R. Schiavilla (JLAB/ODU)  
R.B. Wiringa (ANL)

Prof. Magda Ericson, Emeritus Professor  
IPN Lyon (France) and CERN (Switzerland)  
e-mail: [mericson@cern.ch](mailto:mericson@cern.ch)

Dr. Marco Martini, Senior Post-Doc  
Ghent University (Belgium)  
e-mail: [martini.marco@gmail.com](mailto:martini.marco@gmail.com)

June 13<sup>th</sup> 2015

**Letter of support for nuPRISM full proposal submission to J-PARC PAC.**

We write this letter in support of the project of the nuPRISM water Cherenkov detector.

The possibility to observe charged current neutrino interactions over a continuous range of off-axis angle, providing a direct constraint between lepton kinematics and neutrino energy would have important consequences for several aspects of neutrino physics.

First, in connection with the neutrino oscillation program with water Cherenkov detectors like Super-Kamiokande and Hyper-Kamiokande, the results obtained with nuPRISM would solve the well known neutrino-energy reconstruction problem. Indeed in the Cherenkov detectors the multinucleon component cannot be distinguished from the genuine quasielastic one and affects the determination of the neutrino energy by the usual reconstruction method. In these last years, theoretical studies, performed in particular by ourselves, have shown how much a misidentification of the multinucleon emission component affects the determination of the neutrino energy distribution, hence, as a consequence, the determination of the neutrino oscillation parameters. With respect to the situation of the very recent years, when the multinucleon emission channel was not taken at all into account in the Monte Carlo of the neutrino oscillations and cross sections experiments, the situation now is improved since this channel is included in the generators but the theoretical uncertainties related to the treatment of this complex process remain important. The results obtained with the nuPRISM detector would offer the unique opportunity to obtain the determination of the neutrino energy without any model dependence of the results.

The possibility to produce nearly monoenergetic neutrino measurements is also very important for the neutrino-nucleus interaction physics. In the charged current processes, the simultaneous access to neutrino energy and charged lepton energy and momentum allows the full determination of the energy and momentum transfer to the nucleus, opening the way to detailed studies of nuclear dynamics. In this way, even without the measurement of the final states nucleons, genuine quasielastic events can be more easily disentangled from MEC and Delta resonance ones. nuPRISM would allow to shed light non only on the very debated multinucleon emission channel but also on other nuclear effects, such as long-sought-after RPA influence, including the Ericson-Ericson-Lorentz-Lorentz quenching.

Combining monoenergetic neutrino and antineutrino results as well as muon-neutrino and electron-neutrino measurements will be crucial both for the neutrino oscillation problem and for the understanding of the neutrino-nucleus interaction physics.

In our opinion nuPRISM could represent one of the first major steps of the long-baseline neutrino precision era and can contribute to fill the gap between the accurate knowledge of the electron scattering physics and the neutrino scattering one. Therefore we fully support this project.

Sincerely,

Magda Ericson

Marco Martini

Massachusetts Institute of Technology  
Center for Theoretical Physics  
Cambridge, MA 02139-4307

June 12, 2015

To whom it may concern:

It is a pleasure to write a letter in support of the nuPRISM initiative. By using off-axis, small-angle detection of charged leptons in neutrino-induced reactions on a water target, through the angular distributions involved, this facility would greatly improve the capabilities of neutrino-nucleus reaction studies and therefore of determinations of neutrino oscillations. Presently a major issue with existing facilities is the poorly determined energy of the neutrino beams, and one has been forced to rely on modeling and simulations of the neutrino-nucleus cross sections to extract useful information. While initially there was optimism that the models being used were adequate for this task, in fact, what has emerged is significant doubt that one can do better than perhaps 20-30% using currently available approaches (see below). What nuPRISM would provide is a capability that is more akin to studies of electron scattering at similar kinematics, namely, good determination of the incident neutrino energy (and, of course, direction) and hence of the leptonic part of the reaction including the energy and momentum transferred to the nucleus. Such would be a major advance in the field.

Our international group of collaborators, involving members at M.I.T., in Italy and in Spain, have been involved in theoretical studies of electroweak interactions with nuclei for some time now. We typically either use relativistic modeling of nucleon knockout via one-body currents (the so-called quasielastic contribution), of two-nucleon knockout via two-body meson-exchange currents and of pion production, especially in the region of the Delta resonance, or we use scaling ideas, the so-called SuperScaling Approach (SuSA). In doing so we have attempted to quantify the levels of uncertainty both in our modeling and in the modeling done by other groups, finding that the 20-30% level stated above is typical, and not really satisfactory for the goals of the neutrino program

worldwide (both for oscillations and for reaction studies). Since we have considerable experience with electron scattering, as well as neutrino reactions, we obviously appreciate the great advantages of having a well-defined incident beam.

Accordingly, we are all very supportive of this initiative. Personally, in conversations with Kendall Mahn, I have offered to participate by bringing our approaches to bear on helping to disentangle the various reaction mechanisms at play. I am also part of a collaboration involving members at Los Alamos, JLab, ANL, FNAL and several universities who hope to inter-connect their theoretical undertakings with the nuPRISM program (see other letters of support). We all believe that this initiative would be a big step forward and strongly hope that it can be implemented.

Sincerely,

A handwritten signature in black ink, appearing to read "T.W. Donnelly". The signature is written in a cursive style with a horizontal line through it.

T. W. Donnelly  
MIT 26-403  
1-617-253-4847  
[donnelly@mit.edu](mailto:donnelly@mit.edu)